Nonadiabatic Electron Transfer in the Condensed Phase, via Semiclassical and Langevin Equation Approach

by

XiaoGeng Song

B.S., Univ. of Alberta (2003)

Submitted to the Department of Chemistry
in partial fulfillment of the requirements for the degree of

Doctor of Philosophy

at the

MASSACHUSETTS INSTITUTE OF TECHNOLOGY

Febuary 2009

Author.....
Department of Chemistry
March 14, 2008

Certified by .....
Troy Van Voorhis
Associate Professor of Chemistry
Thesis Supervisor

Accepted by.....
Jianshu Cao
Chairman, Associate Professor of Chemistry

This doctoral thesis has been examined by a Committee of the Department of Chemistry as follows:

Professor Jianshu Cao.....
Chairman, Thesis Committee
Associate Professor of Chemistry

Professor Troy Van Voorhis.....
Thesis Supervisor
Associate Professor of Chemistry

Professor Moungi Bawendi .....
Lester Wolfe Professor in Chemistry

Professor Robert W. Field.....
Chairman, Department Committee on Graduate Study

Nonadiabatic Electron Transfer in the Condensed phase, via Semiclassical and Langevin Equation Approach

by
XiaoGeng Song

Submitted to the Department of Chemistry
on March 31, 2009, in partial fulfillment of the
requirements for the degree of
Doctor of Philosophy

Abstract

In this dissertation, we discuss two methods developed during my PhD study to simulate electron transfer systems. The first method, the semi-classical approximation, is derived from the stationary phase approximation to the path integral in the spin-coherent representation. The resulting equation of motion is a classical-like ordinary differential equation subject to a two-ended boundary condition. The boundary value problem is solved using the "near real trajectory" algorithm. This method is applied to three scattering problems to compute the transmission and reflection probabilities. The strength and weakness of this approach is investigated in details. The second approach is based on the generalized Langevin equation, in which the quantum transitions of electronic states are condensed into a linear regression equation. The memory kernel in the regression equation is computed using a second perturbation expansion. The perturbation is optimized to achieve the best convergence of the second order expansion. This procedure results in a tow-hop Langevin equation, the THLE. Results from a spin-boson system validate the THLE in a wide range of parameter regimes. Lastly, we tested the feasibility of using Monte Carlo sampling to compute the memory kernel from the spin-boson system and proposed a smoothing technique to reduce the number of sampling points.

Thesis Supervisor: Troy Van Voorhis

Title: Associate Professor

Acknowledgments

I would like to than my advisor, Troy Van Voorhis, for his support and guidance during my stay at M.I.T. Troy's endless effort and patience on revising my draft papers are not to be expected from anyone else. I will always fondly and painfully recall his comments on my first draft paper, in which his comments are longer than the paper. His extensive knowledge on areas I have worked on has also been very helpful and beneficial to me.

I would like to thanks members in my group as well. I. Rudra, Q. Wu, O. Vydrov, C. L. Cheng, J. Evans, A. Y. Lu, L. P. Wang, B. Kaduk and S. Yost have been great friends and colleagues. I am grateful to many members of the greater theoretical group, the zoo: X. Xiang, S. L. Yang, J. L. Wu, , J. Witkoskie, V. Lubechenco, E. Zimanyi, X. Chen and M. Kryvohuz. I want to thank S. Presse for helpful discussions on various interesting research topics as well as his sense of humor during boring periods.

I would like to thank members of my thesis committee Prof. Bawendi and Prof. Cao. Prof. Cao has provided many helpful suggestions and references and contributed to the success of my projects.

I also benefitted greatly from taking high caliber classes at M. I. T. Prof. Negele's knowledge, rigor and mathematical elegance will be always be an inspiration.

Prof. Wang and Prof. Thoss have also been of great help at providing auxiliary data and inputs for my research and their efforts are much appreciated.

The National Sciences and Engineering Coucil of Canada has provided continued funding through my PhD program. I am grateful to all Canadian tax payers for their support.

I could not have completed my PhD study without friends around the Boston area. XiaoGeng Song would like to thank Xuemin Chi in particular for her friendship and support during the most depressing, ridiculous, dreadful and desperate times as well as many happy moments.

Finally and most importantly, my mom, Cindy Hao has been the most important person through out my life. This dissertation is dedicated to her and my family.

Contents

List of Figures

Chapter 1

Introduction

To start the discussion of my PhD research, we look at the basic equations and the difficulties dealing with them directly. Then we will briefly discuss the established approximations. Finally, methods developed during my PhD research will be introduced.

1.1 The Born-Oppenheimer approximation and beyond

A molecular system consists of both nuclei and electrons. In principle, both types of degrees of freedom are treated at an equal footing in the time-independent Shrödinger equation:

$$H(R,r)\Psi(R,r) = E\Psi(R,r) \tag{1.1}$$

where $\Psi(R,r)$ is the wavefunction of both the nuclear degrees of freedom R and the electronic degrees of freedom r. The Hamiltonian operator is defined as:

$$H(R,r) = T_e + T_N + U(R,r) \tag{1.2}$$

where T_e and T_N are the kinetic energy operators of the electron and nuclei and $U(R,r)$ is the potential energy of both the nuclei and electron[1, 2]. Since the mass of the lightest

nucleus, proton, is over 1000 times then the mass of an electron, there is a natural separation of time scales in the motions of nuclei and electrons. Therefore it makes sense to write and total wavefunction as a sum of product wavefunctions:

$$\Psi(R,r) = \sum_n \chi_n(R)\psi_n(R,r) \tag{1.3}$$

where $\chi_n(R)$ are a set of nuclear wavefunctions and $\psi_n(R,r)$ are the electronic wavefunctions that have parametric dependence on the nuclear coordinates R. Often $\psi_n(R,r)'s$ are required to be the eigenstates of the electronic Hamiltonian:

$$H_e(R,r)\psi_n(R,r) = V_n(R)\psi_n(R,r), \tag{1.4}$$

where $H_e = T_e + U(R,r)$ is the electronic Hamiltonian and $V_n(R)$ is the eigenvalue of the nth electronic state, as a function of the nuclear coordinates. Such $\psi_n(R,r)$ are often named adiabatic representations, since the total Hamiltonian can be represented as matrix element between the adiabatic states:

$$H_{m,n}(R) \;=\; \langle\psi_m(R,r)|H(R,r)|\psi_n(R,r)\rangle. \tag{1.5}$$

Assuming the nuclear kinetic energy operator takes the usual form:

$$T_N = -\sum_i \frac{1}{2m_i}\frac{\partial^2}{\partial R_i} \tag{1.6}$$

where the index i runs over the nuclear coordinates, the matrix element $H_{m,n}(R)$ can be written explicitly[3]:

$$H_{m,n}(R) = T_N + \sum_j C^{(i)}_{m,n}(R)\frac{\partial}{\partial R_i} + D_{m,n}(R) + V_n(R)\delta_{m,n} \tag{1.7}$$

where $C^{(i)}_{nm}(R)$ is the nonadiabatic coupling vector given as:

$$C^{(i)}_{m,n}(R) = -\sum \langle \psi_m(R,r)| \frac{1}{2m_i} \frac{\partial}{\partial R_i} |\psi_n(R,r)\rangle \tag{1.8}$$

and the matrix D_{mn} is known as the Born-Oppenheimer correction and serves as an additional potential energy term:

$$D_{m,n} = \sum \langle \psi_m(R,r)| \frac{1}{2m_i} \frac{\partial^2}{\partial^2 R_i} |\psi_n(R,r)\rangle. \tag{1.9}$$

An important use of equation 1.7 is to assume that only the ground state of electrons are involved. Since the diagonal element of the non-adiabatic coupling vector can be shown to be zero[3], we are left with the familiar nuclear Hamiltonian:

$$H_0(R) = T_N + V_0(R), \tag{1.10}$$

where we also assumed the Born-Oppenheimer correction is negligible. Equation 1.10 is the Born-Oppenheimer approximation, where nuclei are assumed to move on the ground state potential energy surface. Further more, the nuclear motion are often assumed to be classical and numerous applications have been done under such approximation.

However, as the title of this thesis indicates, we are mainly interested in studying electron transfer reactions, where a donor electronic state will eventually evolves to the acceptor state. Such problem involves multiple electronic states by nature and we must go beyond the Born-Oppenheimer approximation. The inclusion seems easy at first: one only needs to calculate more electronic states and deal with a 2 by 2 Hamiltonian instead of a 1 by 1 Hamiltonian. In reality, however, the difficulties associated with going from a single-state system to a multiple-states system increase dramatically.

The main problem is that the nuclear dynamics are often assumed to be classical while the dynamics among discrete electronic states are inherently quantum. The combination

of two types of dynamics is at least ambiguous and non-unique and many version of mixed quantum-classical methods exist[4, 3, 5, 6, 7, 8]. In the next section we will briefly discuss a few widely used methods.

In addition, the nonadiabatic coupling vector is difficult to calculate since it involves taking derivatives of the electronic wavefunction. Adiabatic representation also leads to conical intersections, where the dipole operator is undefined, thus making it poorly suited to study electron transfer reactions[9].

An alternative choice to the adiabatic representation. The diabatic representation, uses electronic wavefunctions that are independent of the nuclear coordinates. In this representation, both the nonadiabatic coupling vector and the Born-Oppenheimer correction disappears and the diabatic Hamiltonian is:

$$H_{m,n}(R) = T_N + V_{m,n}(R) \tag{1.11}$$

where $V_{m,n}(R)$ is the matrix element of the electronic Hamiltonian:

$$V_{m,n}(R) = \sum \langle \psi_m(r) | H_e(R,r) | \psi_n(r) \rangle. \tag{1.12}$$

This is especially relevant since an efficient and accurate method has been developed to compute the matrix elements of the diabatic states[10, 11, 12, 13].

1.2 Quasi-classical methods

Classical mechanics provides a useful description for complex molecular systems. Not only is classical mechanics more intuitive, the computational cost of a classical system is also much more affordable than a quantum system. For a system with N degrees of freedom, the computational cost of solving classical equations of motion scales as N^2, where most of the cost is involved in computing the forces at each time step. On the contrary, the cost of solving

the Shrödinger equation scales as m^N, where m is the number of basis functions in each degrees of freedom. Even if we assume that $m = 10$ will suffice, the most advanced computers today can only deal with matrices as large as one million by one million, corresponding to $N = 6$. A typical chemical system in condensed phase consists of a few hundred degrees of freedom. Clearly, a straightforward quantum mechanical expansion will fail while the classical approximation is still computationally feasible.

However, when the classical assumption breaks down, such as in an electron transfer reaction discussed above, innovations must be made. But it is not necessary to abandon classical mechanics altogether. Hence the inclusion of nonadiabatic effects into classical-like descriptions has been a topic of much interest in chemical physics. Some successful methods include the surface hopping method[3], the Ehrenfest method[14] and the semi-classical method in the initial value representation(SCIVR)[6, 7].

1.2.1 The Ehrenfest method

The Ehrenfest method is derived using the mean field approximation, in which the total wavefunction is approximated as a single product between the nuclear wavefunction and the electronic wavefunction. The nuclear wavefunction is often replaced by the classical trajectory of the nuclei.

The diabatic representation of an N-state electron transfer system is:

$$H = \frac{p^2}{2m} + V_{i,j}(q).$$

Then the state of the system at time t, by the Ehrenfest method, is $\{p(t), q(t), c_i(t)\}$, where $p(t)$ and $q(t)$ are the momentum and position of the nuclei and $c_i(t)$'s are the coefficient of

the electronic state. The equation of motion for these variables are:

$$\begin{aligned} \dot{q} &= p/m \\ \dot{p} &= -\sum c_i^*(t)\frac{\partial}{\partial q}V_{i,j}(q(t))c_j(t) \\ \dot{c}_i(t) &= -i\sum_j V_{i,j}(q(t))c_j(t). \end{aligned} \tag{1.13}$$

As equation 1.13 indicates, the coefficients of the electronic states follow the usual time-dependent Shrödinger equation and the momenta and positions of the nuclei feel average force from all electronic states, weighted by the coefficients of the electronic states. Equation 1.13 is written in the diabatic representation but it can be modified to employ the adiabatic representation as well.

Equation 1.13 provides a self-consistent way of propagating both the nuclear and electronic degrees of freedom together. The evolution of the electronic states provides a quantum back reaction to the nuclear dynamics through the mean force[8] and the positions of the nuclei give the instantaneous transition elements to the electronic evolutions. The self-consistence and the easy of implementation has made the Ehrenfest method a popular choice in the field of electron transfer[15, 16].

However, limitations of the Ehrenfest method are also well known. One major flaw of the Ehrenfest method is its poor description of the branching of the trajectories to different electronic surfaces. For example, suppose two electronic surfaces predict dynamics in the opposite directions, the Ehrenfest method will predict the average of the two, which is physically incorrect. A more recent discovery is that in condensed phase, the Ehrenfest method predicts a final equilibrium sate that is substantially different from the correct Boltzmann distribution[8], therefore putting the use of the Ehrenfest dynamics in doubts.

1.2.2 The surface hopping(SP) method

The surface hopping method is designed to treat the branching problem that is present in the Ehrenfest method. From the branching point of view, it is more desirable to make the nuclei move on a single surface at one time and use the electronic populations as a criteria for hopping onto another surface[3]. The hopping mechanism can be designed such that the final distribution of electronic states agree with thermal dynamical result[8].

The SP method always uses the adiabatic representation:

$$H = \frac{p^2}{2m} + V_{\delta ij}(q) + mC_{i,j}(q) \cdot p.$$

The equation of motion for the electronic variables is the time-dependent Shrödinger equation:

$$\dot{c}_i(t) = \sum_j c_j(t)[V_{\delta ij}(q) - iC_{ij}(q) \cdot p/m].$$

The difference is that the electronic evolution does not provide a feed back reaction through the mean force. At any time, the nuclei move on a single surface:

$$\dot{p}(t) = \frac{\partial}{\partial q} V_{ii}(q).$$

However, at the each time step, the time derivative of the current electronic population $\frac{d}{dt}|c_i(t)|^2$ provides a transition probability to other states. A random number is selected and compared to the transition probabilities to decide whether a hop should take place. Finally, Monte Carlo sampling is used to converge the probabilistic hops. There are many variations in the exact hopping schemes and some specific examples can be found here[3, 1, 17].

The movement on a single surface is the distinct feature of the SP method. Under the same hypothetical situation where two surfaces make the nuclei move on the opposite directions, the SP result will have two distinct samples corresponds to the different surfaces. The statistical weight of the these two sample give the final electronic populations. This

advantage has made the SP method a popular method and a large number of applications have been seen in the literature[1, 9, 18, 19, 20, 21, 22, 23, 24]. The SP method has another important advantage over the Ehrenfest method. It has been shown that the SP method predicts the correct thermal dynamical distribution while the Ehrenfest often results in large deviations from the correct distribution[8]. In a real simulation, a wrong final distribution corresponds to a different temperature than what is used in the simulation and can leads qualitatively incorrect interpretation of the simulation results.

Despite the success of the SP method, shortcomings exist. It has been observed that in condensed phase, as the number of hops increases, the quality of SP result tends to decrease. The choice of using the adiabatic representation to reduce the number of hops also presnet a difficulty in interprating spectroscopic results from electron transfer reaction, since adiabatic representation leads to conical intersections, where the dipole operator is undefined[9], thus making it poorly suited to study electron transfer reactions.

1.2.3 The semi-classical initial value representation(SCIVR)

Both the Ehrenfest and the SP assume the nulcear dynamics is purely classical. The difference between them can be viewed as how to incorporate the quantum feed back information into the classical dynamics. The semi-classical method, in general, treat both degrees of freedom in the same footing.

The usual semi-classical propagator on a single surface is simply the stationary phase approximation to the path integral representation of the quantum propagator $u(q_i, q_f; T) = \langle q_f | e^{-iHT} | q_i \rangle$. The path integral of this propagator is the functional integral over all paths that connect the intial point q_i at $t = 0$ and the final point q_f at $t = T$:

$$u(q_i, q_f; t) = \int e^{iS[q]} Dq$$

where $S[q]$ is the action:

$$S[q] = \int_0^T dt L(q(t), p(t))$$

and L is the classical Lagrangian given by:

$$L(q(t), p(t)) = \frac{p(t)^2}{2m} - V(q(t)).$$

The functional integral over all paths, except for simple cases such as a quadratic potential, can not be evaluated analytically. The exponential of the action integral, however, is highly oscillatory. Therefore only the stationary paths and variations among are likely to contribution to the functional integral. It is well known that the stationary paths are the classical paths that satisfy the classical equation of motion and the proper boundary conditions:

$$\begin{aligned} \dot{q}(t) &= p(t) \\ \dot{p}(t) &= q(t) \\ q(0) &= q_i \\ q(T) &= q_f. \end{aligned} \tag{1.14}$$

Furthermore, one can expand the exponent around the stationary paths. Due to stationarity, the first order of variations are zero and the second order variations form an multidimensional Gaussian integral, which can be integrated to yield the semi-classical propagator:

$$u_{sc}(q_i, q_f; T) = \frac{1}{\sqrt{\frac{\partial q(T)}{\partial p(0)}}} e^{iS_{sc}}. \tag{1.15}$$

The classical action S_{sc} becomes a phase factor in the semi-classical propagator. The prefactor comes from the Gaussian integral of the second order variations. and contains important information such as the zero point energy. To obtain the classical trajectories, one must solve the "root search" problem, which means one needs to find the correct initial momentum that

leads to the final boundary condition $q(T) = q_f$. In general, the root search problem in a multi-dimensional system does not have a well known solution and present itself as the major challenge to the implementation of the semi-classical approximation.

One way around this is to use the initial value representation(IVR). For example, if one wants to compute the autocorrelation function of the propagator:

$$\langle\psi|e^{-iHt}|\psi\rangle = \int dq_f \int dq_i \langle\psi|q_f\rangle\langle q_f|e^{-iHt}|q_i\rangle\langle q_i|\psi\rangle \tag{1.16}$$

the semi-classicl approximation is then:

$$\langle\psi|e^{-iHt}|\psi\rangle_{sc} = \int dq_f \int dq_i \langle\psi|q_f\rangle \frac{1}{\sqrt{\frac{\partial q(T)}{\partial p(0)}}} e^{iS_{sc}}\langle q_i|\psi\rangle. \tag{1.17}$$

Since the final position $q(T)$ is a function of the initial conditions $q(0)$ and $p(0)$, the integral over the final condition $q(T)$ can be converted into an integral over the initial condition $p(0)$ and the Jacobian of this transformation is $|\frac{\partial q(T)}{\partial p(0)}|$. The result is the SCIVR approximation:

$$\langle\psi|e^{-iHt}|\psi\rangle_{sc} = \int dp_i \int dq_i \langle\psi|q_i(T)\rangle \sqrt{\frac{\partial q(T)}{\partial p(0)}} e^{iS_{sc}}\langle q_i|\psi\rangle. \tag{1.18}$$

The above integral can be compute by Monte Carlo sampling of the initial values of q_i's and p_i's.

To apply the SC method to the electron transfer problem, an additional innovation needs to be made. The path integral for the electronic states is a sum over discrete variables. One needs to find a way to map the discrete variables to their continuous counter part[25]. Then a classical-like Langrangian can be obtained and the SPA used in deriving the SC approximation can be employed. Additionally, the IVR trick can also be used to convert the root search problem into a Monte Carlo evaluation of all initial values[7, 6]. Alternatively, one can design efficient search algorithms to accomplish the root search problem and use likes of equation 1.15 directly[4], which will be discussed in details in the following chapter.

1.3 reduced equations of motion

Although many chemists normally think of electron transfer reactions as electrons hopping among different electronic states, physicist have considered them in the context of quantum dissipations[26, 27]. Some of the well known approximations in quantum dissipations are the Bloch-Redfield equation(BRE)[28] and the non-interacting blip approximation(NIBA)[29, 30, 31, 32]. Both of them can now be derived in the frame of the generalized Langevin equation formulation[33, 28, 34].

1.3.1 The generalized Langevin equation(GLE)

First we introduce the Liouville operator L such that

$$LA = -i[H, A]$$

where A is any quantum operator and H is the Hamiltonian operator. The Liouville operator is often called "super operator" since it operates on quantum operators. The Heisenberg equation of motion of any operator can be written as:

$$\begin{aligned} \dot{A}(t) &= i[H, A(t)] \\ &= LA(t) \end{aligned}$$

or, in the integrated form:

$$\begin{aligned} A(t) &= e^{iHt} A e^{-iHt} \\ &= e^{Lt} A. \end{aligned}$$

The key step in deriving the generalized Langevin equation is to introduce the projection

operator P such that:

$$PB = \frac{(B, A)}{(A^2)} A$$

where B is any operator. The action of P on the operator B is to project it onto the subspace in the operator A. The inner product (A, B) has not been specified at this point. Later it will be shown special choices of the inner product can lead to desired results under different circumstances. It can be easily verified that:

$$PPB = PB$$

so that P is indeed an projection operator. Similarly, the complementary operator $Q = 1 - P$ is also a projection operator and it projects any operator to the subspace outside A. The sum of P and Q is the identity operator: $P + Q = I$.

The use of the projection operator is to partition the equation of motion of A into the dynamics inside the subspace spanned by A and the space outside A. The equation of motion of A is:

$$\begin{aligned} \dot{A}(t) &= LA(t) \\ &= Le^{Lt}A \\ &= e^{Lt}LA \\ &= e^{Lt}(P + Q)LA \\ &= e^{Lt}PLA + e^{Lt}QLA. \end{aligned} \tag{1.19}$$

Using the definition of the projection operator P, the first term in equation 1.19 can be

written as:

$$\begin{aligned} e^{Lt}PLA &= e^{Lt}\frac{(A,LA)}{(A^2)}A \\ &= \frac{(A,LA)}{(A^2)}A(t) \\ &= i\Omega A(t) \end{aligned} \tag{1.20}$$

where the frequency $\Omega = -i\frac{(A,LA)}{(A^2)}$. To partition the second term in equation 1.19, we first partition the propagator e^{Lt} as:

$$\begin{aligned} e^{Lt} &= e^{(Q+P)Lt} \\ &= e^{QLt} - \int_0^t e^{L(t-s)}PLe^{QLs}ds \end{aligned} \tag{1.21}$$

where we have used well known identity:

$$e^{(a+b)t} = e^{at} - \int_0^t e^{(a+b)(t-s)}be^{as}ds. \tag{1.22}$$

Equation 1.22 can be proven by taking the Laplace transform:

$$\begin{aligned} \frac{1}{s+a+b} &= \frac{1}{s+a+b}(s+a)\frac{1}{s+a} \\ &= \frac{1}{s+a+b}(s+a+b-b)\frac{1}{s+a} \\ &= \frac{1}{s+a} - \frac{1}{s+a+b}b\frac{1}{s+a}. \end{aligned}$$

Using the partition of the propagator in equation 1.21, the last term in equation 1.19 becomes:

$$\begin{aligned} e^{Lt}QLA &= [e^{QLt} - \int_0^t e^{L(t-s)}PLe^{QLs}ds]QLA \\ &= e^{QLt}QLA - \int_0^t e^{L(t-s)}PLe^{QLs}QLAds \\ &= e^{QLt}QLA - \int_0^t e^{L(t-s)}\frac{(Le^{QLs}QLA, A)}{(A^2)}Ads \\ &= F(t) - \int_0^t e^{L(t-s)}A\frac{(LF(s), A)}{(A^2)}ds \\ &= F(t) - \int_0^t A(t-s)K(s)ds \end{aligned} \tag{1.23}$$

where the operator $F(t) = e^{QLt}QLA$ is recognized as the noise operator and the function $K(t) = \frac{(LF(s),A)}{(A^2)}$ is known as the memory kernel. Putting together equation 1.19 and equation 1.23, we arrive at the generalized Langevin equation:

$$\dot{A}(t) = i\Omega A(t) - \int_0^t A(t-s)K(s)ds + F(t). \tag{1.24}$$

The generalized Langevin has been well studied and more useful properties have been and are being discovered. Due to the lack of space, we will only discuss aspects relevant to electron transfer problems. Interested readers can find other details in reference[33, 34].

1.3.2 The non-interacting blip approximation(NIBA)

The original NIBA[26] is only applicable to a two state system linearly coupled to a bath. What we will discuss, however, is a more generalized version. The author has also found the derivation using the GLE frame more straightforward then the original derivation using the influence functional.

A two state dissipative system, or, a two state electron transfer system can be written

as:

$$H = \begin{pmatrix} h_1(p,q) & V(g) \\ V(g) & h_2(p,q) \end{pmatrix}$$

where h_1 and h_2 are the Hamiltonians operator on state $|1\rangle$ and state $|2\rangle$, respectively and $V(g)$ is the interstate coupling element. Note we have used the diabatic representation here for simplicity but the extension is straightforward.

To use the GLE, we first define the projection P such that

$$PB = \frac{(O_1, B)}{(O_1^2)} + \frac{(O_2, B)}{(O_2^2)}$$

where $O_1 = |1\rangle\langle 1|$ and $O_2 = |2\rangle\langle 2|$. We also make a special choice of the inner product:

$$(A, B) = \frac{1}{\mathrm{tr}\rho_{eq}} \mathrm{tr}\rho_{eq} AB$$

where the approximate equilibrium density matrix is

$$\rho_{eq} = e^{-\beta h_1} O_1 + e^{-\beta h_2} O_2.$$

This specific form of inner product allows a convenient property:

$$PL_0 = 0$$

where L_0 is the reference Liouville operator such $L_0 A = i[H_0, A]$. The perturbative Liouville operator L_v is defined similarly:

$$L_v A = i[L_v, A].$$

Other two properties are also useful:

$$\begin{aligned} L_0 O_{1/2} &= 0 \\ P L_v O_{1/2} &= 0. \end{aligned}$$

Both identities can be verified using definitions.

Now we shall determine each terms in the GLE. First the frequency term Ω is obviously zero and we are only left with the memory kernel and the noise term. The difficulty involved in computing the two quantities is the exponential of the operator QL. However, this can be done using perturbation expansions in powers of QL_v:

$$\begin{aligned} e^{QLt} &= e^{(L_0+QL_v)t} \\ &= e^{L_0 t} - \int_0^t e^{QL(t-s)} Q L_v e^{L_0 s} ds \\ &= e^{L_0 t} - \int_0^t e^{QL_0(t-s)} Q L_v e^{L_0 s} ds + \cdots \end{aligned} \tag{1.25}$$

To second order in QL_v, the noise term terms out to be:

$$\begin{aligned} F^{(2)}_{1/2}(t) &= e^{QLt} Q L O_{1/2} \\ &= e^{QLt}(1-P) L_v O_{1/2} \\ &= e^{QLt} L_v O_{1/2} \\ &= e^{L_0 t} L_v O_{1/2} - \int_0^t e^{QL_0(t-s)} Q L_v e^{L_0 s} L_v O_{1/2} \\ &= \int_0^t e^{QL_0(t-s)} Q L_v e^{L_0 s} L_v O_{1/2}. \end{aligned} \tag{1.26}$$

The second order kernel is computed similarly:

$$\begin{aligned} K^{(2)}(t) &= \frac{(L_V e^{L_0 s} L_V O, O)}{(O^2)} \\ &= \begin{pmatrix} (L_V e^{L_0 s} L_V O_1, O_1) & (L_V e^{L_0 s} L_V O_1, O_2) \\ (L_V e^{L_0 s} L_V O_2, O_1) & (L_V e^{L_0 s} L_V O_2, O_2) \end{pmatrix} \begin{pmatrix} \frac{1}{(O_1)} & 0 \\ 0 & \frac{1}{(O_2)} \end{pmatrix} \\ &= \begin{pmatrix} \frac{1}{(O_1)}(L_V e^{L_0 s} L_V O_1, O_1) & \frac{1}{(O_2)}(L_V e^{L_0 s} L_V O_1, O_2) \\ \frac{1}{(O_1)}(L_V e^{L_0 s} L_V O_2, O_1) & \frac{1}{(O_2)}(L_V e^{L_0 s} L_V O_2, O_2) \end{pmatrix} \end{aligned} \tag{1.27}$$

Since $O_1 + O_2 = I$, we have $K_{21}^{(2)}(t) = -K_{11}^{(2)}(t)$ and $K_{22}^{(2)}(t) = -K_{12}^{(2)}(t)$. In another world, the memory kernel satisfies the well known sum rule and the conservation of total probability is automatically satisfied: $O_1(t) + O_2(t) = 1$. Using the existing result, we can write the equation of motion for $O_1(t)$ as:

$$\begin{aligned} \dot{O}_1(t) &= -\int_0^t K_{11}^{(2)}(s) O_1(s) ds - \int_0^t K_{12}^{(2)}(s) O_2(s) ds + F_1(t) \\ &= -\int_0^t [K_{11}^{(2)}(s) - K_{12}^{(2)}(s)] O_1(s) ds - \int_0^t K_{12}^{(2)}(s) ds + F_1(t) \end{aligned} \tag{1.28}$$

The final step in deriving the generalized NIBA is to multiply equation 1.28 by the desired initial density matrix ρ_0 and take the average:

$$\langle O_1 \rangle = -\int_0^t [K_{11}^{(2)}(s) - K_{12}^{(2)}(s)] \langle O_1(s) \rangle ds - \int_0^t K_{12}^{(2)}(s) ds + \langle F_1(t) \rangle. \tag{1.29}$$

Similar reduced equations of motion for population dynamics to equation 1.29 have been derived using various approaches[29, 35, 36, 31, 30] but equation 1.29 contains the essential. All of these approaches involve writing reduced equations of motion for populations and using second order approximations for the memory kernel and noise. The advantage of using equation 1.29 is that one only deals with averages of quantum operators instead of these operators themselves. Although one still needs to compute averages containing the zero order

propagator $e^{L_0 t}$, the zero order operator only involves propagation on single electronic states and contains no discrete quantum transitions. Therefore one can use various established quasi-classical methods for computational purposes. Furthermore, for many model systems, the second order memory kernel and noise can be computed almost analytically. Thus asymptotic analysis of the memory kernel and noise can often lead to insightful conclusions of the electron transfer processes.

There are, however, problems with equation 1.29. In a phenomenologically Langevin equation the average of the noise is often zero identically, thus equation 1.29 would be closed in the averages of $O_1(t)$ and $O_2(t)$. Furthermore, one can show that the kernels $K_{11}(t)$ and $K_{12}(t)$ satisfy the correct detailed balance relation:

$$\frac{\bar{K}_{11}}{\bar{K}_{12}} = \frac{O_2^{eq}}{O_1^{eq}} \tag{1.30}$$

where the rates are the long time integral of the kernels:

$$\begin{aligned} \bar{K}_{11} &= \int_0^\infty K_{11}(t)dt \\ \bar{K}_{12} &= \int_0^\infty K_{12}(t)dt \end{aligned}$$

and the equilibrium averages of the population operators are:

$$\begin{aligned} O_1^{eq} &= \frac{\mathrm{tr}\rho_{eq}O_1}{\mathrm{tr}\rho_{eq}} \\ O_2^{eq} &= \frac{\mathrm{tr}\rho_{eq}O_2}{\mathrm{tr}\rho_{eq}}. \end{aligned}$$

Therefore, in the absence of the noise, the population will relax to the correct equilibrium values. The noise, however, only vanishes for initial densities that deviates linearly away from the equilibrium density matrix. This is puts a huge restriction on equation 1.29 and greatly limits its use[37].

Later we will present a different Langevin equation where we look at the correlation function of the population fluctuations instead of the populations themselves. Then we will show the noise term vanishes and we can freely choose from a large family of initial densities to resemble most electron transfer experiments.

Another closely related approximation is the Bloch-Redfield equation(BRE). If we instead choose the density matrix of the two state system as the observables and apply the GLE, the result is a generalized quantum master equation for the reduced density matrix of the two state system. Similarly, if we expand the memory kernel in the generalized quantum master in the difference of two single surface Hamiltonians, we arrive at the BRE[38]. Since the generalized NIBA is more closely related to our discussion, we shall not discuss the BRE in further details. Interested readers can find more discussions on this topic in reference[39, 40, 41, 42, 38].

Chapter 2

A coherent state approach to semi-classical nonadiabatic dynamics

2.1 introduction

Classical mechanics provides a useful description for complex molecular systems. However, the classical approach breaks down when quantum effects are non-negligible. One example is the breakdown of the Born-Oppenheimer approximation. Although the quantum mechanical generalization beyond the Born-Oppenheimer approximation is straight forward[43, 2], the exponential scaling with respect to the system dimensionality limits the applicability of quantum mechanical treatment to systems of only a few degrees of freedom. Hence the inclusion of nonadiabatic effects into classical-like descriptions has been a topic of much interest in chemical physics. The difficulty is that for nonadiabatic systems, classical mechanics is hard to define.

In order to tackle this problem, many mixed quantum-classical formulations[14, 44, 45, 46, 47, 48] as well as SC formulations[49, 6, 7, 50, 51, 52, 53, 54, 55] have been proposed. Among the mixed quantum-classical methods, two widely used methods are the Ehrenfest method[14] and the surface hopping (SH) method[46]. The former can be derived from taking the classical limit of the time-dependent Hartree approximation. The result is that

the nuclei move on a mean field potential generated by taking the expectation value of the electronic Hamiltonian. One major flaw of the Ehrenfest method is its poor description of the branching of the trajectories to different electronic surfaces. The SH method, on the other hand, is aimed at accurately describing the branching. In this method, the nuclei move on a single electronic potential surface and a stochastic switch is used to cause the nuclei to hop onto other surfaces according to the time dependent populations of the electronic surfaces. Both methods (and their variants) have been widely used in studying various problems in chemistry and physics[23, 24, 16, 56, 9, 57, 58, 21, 22]. However, like most quasi-classical formulations, some quantum mechanical effects are not accounted for. For example, trajectories in both methods evolve independently so the interference effects among them are ignored. Also, neither method is capable of providing the phase information of the system, which is required to understand the absorption spectrum and the Raman spectrum, which are often important experimental tools used in studies of nonadiabatic reactions.

The SC approximation is favored by many due to its potential ability to address the above problems as well as its more dynamically consistent treatment of the nuclear and the electronic degrees of freedom. The first "semi-classically exact" derivation is due to Pechukas[55], where the path integral over the electronic degrees of freedom is evaluated exactly, as a functional of the nuclear path. Then the resulting nuclear path integral is evaluated via the stationary phase approximation. The "Pechukas force" derived from the stationary phase approximation is non-local and in practice very difficult to calculate. Stock and Thoss[7, 50] as well as Sun and Miller[6] have independently developed a more practical SC approximation. In the work of Stock and Thoss, a mapping procedure is used to convert the discrete electronic degrees of freedom to continuous degrees of freedom that can be treated as classical variables. An Herman-Kluk type initial value representation (IVR)[59, 60] is used to evaluate the SC propagator. Sun and Miller arrived at the same SC propagator using the Meyer-Miller "classical electron analog"[44] to derive a classical-like Hamiltonian and quantize it using the SC-IVR. These IVR methods have shown to be promising and have

been extended and applied to various problems[54, 49, 57, 61]. However, the IVR-type SC propagator requires a multi-dimensional integral over phase space. Due to the chaotic behavior of the integrand, Monte Carlo evaluation of the phase space integral requires a huge number of trajectories to converge. For example, in the application to a 24-mode model Hamiltonian[61], the mapping SC-IVR accurately reproduced the experimental results but up to 10^7 trajectories were needed for convergence. Thus, the computational cost of the IVR phase space integral for this system is comparable to the cost of an essentially exact calculation, which can be performed employing 10^7 well-chosen basis functions[62]. Hence it would be desirable if one could avoid the phase space integral by using a non-IVR method.

In this chapter we present a nonadiabatic SC propagator derived from the SPA of an exact path integral, in which we use canonical coherent states for the nuclear degrees of freedom and spin coherent states for the electronic degrees of freedom. The use of spin coherent states can be viewed as an alternative mapping procedure to the Schwinger boson approach[7, 50, 1] and these states have a long history of applications in mixed quantum-classical systems: they facilitate a path-integral description of discrete transitions[63], they can be used to derive a trace formula in the extended phase space of quantum and classical degrees of freedom[64, 65] and the resulting expressions can be used to analyze the periodic orbit decomposition of spin-orbit interactions[66, 65]. Our present interest in spin coherent states for nonadiabatic SC dynamics stems from the fact that coherent states allow us to circumvent the phase space integral inherent in IVR approaches[67, 68]. In this article, we generalize the previously developed "real trajectory search algorithm"[67, 68] used for the single surface SC propagator to the nonadiabatic case. The derivation of the SC propagator is presented in Section II as well as descriptions of the root search algorithm. Section III shows the performance of the SC propagator in the three model systems suggested by Tully[46]. We observe some general trends of the performance of the SC propagator from these testing models. These trends are discussed in section IV and a simple system is used to show how the SC propagator can be improved. A summary of our work as well as future directions are

provided in section V.

2.2 the SC nonadiabatic propagator

The path Integral representation of the nonadiabatic propagator

For a nonadiabatic system with N nuclear degrees of freedom and 2 electronic states (the formulation can be generalized to more than 2 states but will involve more complicated algebra), the Hamiltonian in the diabatic representation is

$$\hat{H}(\hat{\mathbf{q}},\hat{\mathbf{p}}) = \sum_{i=0}^{N-1} \frac{\hat{p}_i^2}{2m_i}\hat{I}_e + \begin{pmatrix} h_{11}(\hat{q}) & h_{12}(\hat{q}) \\ h_{21}(\hat{q}) & h_{22}(\hat{q}) \end{pmatrix}. \tag{2.1}$$

A spin 1/2 coherent state[69] defined by

$$|\tilde{s}) = |0\rangle + \tilde{s}|1\rangle, \tag{2.2}$$

gives the identity operator in the electronic subspace a continuous form

$$\hat{I}_e = \int \frac{|\tilde{s})(\tilde{s}|}{(\tilde{s}|\tilde{s})}\mu(\tilde{s},\tilde{s}^*)d\tilde{s}\wedge d\tilde{s}^*, \tag{2.3}$$

where $\tilde{\mu}(\tilde{s},\tilde{s}^*)$ is the measure. A similarity transform can be then applied to $\hat{I}_e$:

$$\hat{I}_e = \int e^{u^*\hat{J}_+}|\tilde{s})(\tilde{s}|e^{-u^*\hat{J}_+}\frac{\mu(\tilde{s},\tilde{s}^*)}{(\tilde{s}|\tilde{s})}ds\wedge ds^*, \tag{2.4}$$

where u is an arbitrary complex number and $\hat{J}_+$ is the raising operator such that $\hat{J}_+|0\rangle = |1\rangle$. According to Solari[70], equation 2.4 can be put into the form:

$$\hat{I}_e = \int |s)(\bar{s}^*|\frac{\mu(s,\bar{s})}{(\bar{s}^*|s)}ds\wedge ds^*, \tag{2.5}$$

where $s = \tilde{s} + u$, $\bar{s} = \frac{\tilde{s}^*}{1-\tilde{s}^* u^*}$ and $\mu(s, \bar{s})$ is the appropriate new measure. The additional degree of freedom provided by u makes s and $\bar{s}$ independent variables.

The identity operator in the nuclear subspace can be written as a phase space integral using the canonical coherent states[69] defined by complex variables $\mathbf{z} = (\mathbf{q} + i\mathbf{p})/\sqrt{2}$

$$\hat{I}_n = \int \frac{|\mathbf{z})(\mathbf{z}|}{(\mathbf{z}|\mathbf{z})} d\mathbf{z} \wedge d\mathbf{z}^*, \tag{2.6}$$

where the canonical coherent state $|\mathbf{z})$ is the product of one dimensional canonical coherent states

$$|\mathbf{z}) = \prod_{i=0}^{M-1} |z_i). \tag{2.7}$$

In position representation, a canonical coherent state is a Gaussian wavepacket centered at q and p in phase space[71]:

$$\langle x|z) = e^{-\frac{1}{2}(x-q)^2 + ip(x-q/2)}, \tag{2.8}$$

and, though q and p are familiar in terms of classical mechanics, here we use z for more simplified algebra. A similarity transform can also be applied to the nuclear space identity operator[67] and equation 2.6 can be written as:

$$e^{\mathbf{v}^* \hat{\mathbf{a}}} \hat{I}_n e^{-\mathbf{v}^* \hat{\mathbf{a}}} = \int \frac{|\mathbf{z})(\bar{\mathbf{z}}^*|}{(\bar{\mathbf{z}}^*|\mathbf{z})} d\mathbf{z} \wedge d\mathbf{z}^*, \tag{2.9}$$

where $\bar{\mathbf{z}} = \mathbf{z}^* + \mathbf{v}^*$ and since $\mathbf{v}$ is arbitrary, $\mathbf{z}$ and $\bar{\mathbf{z}}$ are independent variables. The direct product of the two subspace identity operators gives the complete space identity operator

$$\hat{I} = \int \frac{|\mathbf{z}, s)(\bar{\mathbf{z}}^*, \bar{s}^*|}{(\bar{\mathbf{z}}^*, \bar{s}^*|\mathbf{z}, s)} \mu(s, \bar{s}) d\mathbf{z} \wedge d\mathbf{z}^* ds \wedge ds^*, \tag{2.10}$$

where $(\mathbf{z}, s)$ and $(\bar{\mathbf{z}}, \bar{s})$ are independent sets of variables. By inserting the similarity transformed identity operator (equation 2.10) into the matrix element of the propagator $U_{f,i}(t) = (\mathbf{z}_f, s_f|e^{-i\hat{H}t}|\mathbf{z}_i, s_i)$ $M+1$ times and taking the limit of large M, we have the path integral

representation of the propagator[69, 70, 72, 67, 73]:

$$(\mathbf{z}_f, s_f|e^{-i\hat{H}t}|\mathbf{z}_i, s_i) = \lim_{M\to\infty} \int \cdots \int \prod_{m=0}^{M} \mu(s_m, \bar{s}_m) d\mathbf{z}_m \wedge d\mathbf{z}_m^* ds_m \wedge ds_m^* e^F, \tag{2.11}$$

where F is the discrete action:

$$\begin{aligned} F = & \sum_{m=1}^{M} \ln\left[\frac{(\bar{\mathbf{z}}_m^*, \bar{s}_m^*|\mathbf{z}_{m-1}, s_{m-1})}{(\bar{\mathbf{z}}_m^*, \bar{s}_m^*|\mathbf{z}_m, s_m)}\right] \\ & -i\frac{t}{M}\frac{(\bar{\mathbf{z}}_m^*, \bar{s}_m^*|\hat{H}|\mathbf{z}_{m-1}, s_{m-1})}{(\bar{\mathbf{z}}_m^*, \bar{s}_m^*|\mathbf{z}_{m-1}, s_{m-1})} \\ & +\ln\left[\frac{(\mathbf{z}_f, s_f|\mathbf{z}_M, s_M)(\bar{\mathbf{z}}_0^*, \bar{s}_0^*|\mathbf{z}_i, s_i)}{(\bar{\mathbf{z}}_0^*, \bar{s}_0^*|\mathbf{z}_0, s_0)}\right]. \end{aligned} \tag{2.12}$$

Equation 2.11 is a formally exact path integral in the limit of large M. Here we note that the spin coherent state formulation has been used by

The stationary path approximation

If the functional integral of the discrete action is done according to the stationary path approximation, the result is the SC approximation to the propagator. The stationary conditions on F read:

$$\begin{aligned} \frac{\partial F}{\partial \mathbf{z}_m} = 0 \qquad \frac{\partial F}{\partial s_m} = 0 \\ \frac{\partial F}{\partial \bar{\mathbf{z}}_m} = 0 \qquad \frac{\partial F}{\partial \bar{s}_m} = 0. \end{aligned} \tag{2.13}$$

Evaluating the derivatives and taking the limit $M \to \infty$ gives equations of motion:

$$\begin{aligned}
\dot{\mathbf{z}} &= -i\frac{\partial H(\mathbf{z}, s, \bar{\mathbf{z}}, \bar{s})}{\partial \bar{\mathbf{z}}} \\
\dot{s} &= -i(1 + s\bar{s})^2\frac{\partial H(\mathbf{z}, s, \bar{\mathbf{z}}, \bar{s})}{\partial \bar{s}} \\
\dot{\bar{\mathbf{z}}} &= i\frac{\partial H(\mathbf{z}, s, \bar{\mathbf{z}}, \bar{s})}{\partial \mathbf{z}} \\
\dot{\bar{s}} &= i(1 + s\bar{s})^2\frac{\partial H(\mathbf{z}, s, \bar{\mathbf{z}}, \bar{s})}{\partial s},
\end{aligned} \tag{2.14}$$

where the classical Hamiltonian that governs the equations of motion is the matrix element of the quantum Hamiltonian :

$$H(\mathbf{z}, s, \bar{\mathbf{z}}, \bar{s}) = \frac{(\bar{\mathbf{z}}^*, \bar{s}^*|\hat{H}|\mathbf{z}, s)}{(\bar{\mathbf{z}}^*, \bar{s}^*|\mathbf{z}, s)}. \tag{2.15}$$

When equation 2.13 is applied to the end points ($m = 0, M$), boundary conditions are naturally selected:

$$\begin{aligned}
\mathbf{z}(0) &= \mathbf{z}_i \qquad s(0) = s_i \\
\bar{\mathbf{z}}(t) &= \mathbf{z}_f^* \qquad \bar{s}(t) = s_f^*.
\end{aligned} \tag{2.16}$$

Since the initial values of the barred variables are not specified but only their final values, $\bar{z}(0)$ and $\bar{s}(0)$ can always be adjusted such that the final boundary conditions will be met. This asymmetry of the barred and unbarred variables results from the similarity transform, which makes it clear that the two sets of variables are not necessarily complex conjugates of each other. As a result, the nuclear trajectory ($\mathbf{q} = \frac{\mathbf{z}+\bar{\mathbf{z}}}{\sqrt{2}}$, $\mathbf{p} = \frac{\mathbf{z}-\bar{\mathbf{z}}^*}{i\sqrt{2}}$) is complex valued in general.

The SC propagator is obtained by expanding the action in equation 2.12 to second order around the stationary path, performing the $M + 1$ resulting Gaussian integrals and taking the limit of $M \to \infty$. Here we merely present the results of these operations since the

corresponding details can be found elsewhere[70, 72, 25, 74, 73]. The SC propagator takes the usual form

$$(\mathbf{z}_f, s_f|e^{-i\hat{H}t}|\mathbf{z}_i, s_i) = Ke^{iS_{cl}}, \tag{2.17}$$

where the classical action S_{cl} is:

$$\begin{aligned} S_{cl} &= \int_0^t d\tau \left[i\frac{\bar{s}\dot{s}}{(\bar{s}^*|s)} + i\bar{\mathbf{z}}\dot{\mathbf{z}} - H(\mathbf{z}, s, \bar{\mathbf{z}}, \bar{s}) \right] \\ &\quad -i\ln(\mathbf{z}_f, s_f|\mathbf{z}(t), s(t)), \end{aligned} \tag{2.18}$$

and the reduced propagator K that takes quadratic fluctuations around the classical trajectory into account is

$$K = e^{\phi_e} \left(\begin{vmatrix} \frac{\partial \bar{\mathbf{z}}(t)}{\partial \bar{\mathbf{z}}(0)} & \frac{\partial \bar{s}(t)}{\partial \bar{\mathbf{z}}(0)} \\ \frac{\partial \bar{\mathbf{z}}(t)}{\partial \bar{s}(0)} & \frac{\partial \bar{s}(t)}{\partial \bar{s}(0)} \end{vmatrix} \frac{(\bar{s}^*(0)|s_i)}{(s_f|s(t))} \right)^{-1/2}. \tag{2.19}$$

The stability matrix is integrated along the classical path according to the matrix equation:

$$\frac{d}{dt} \begin{pmatrix} \frac{\partial \mathbf{z}(t)}{\partial \mathbf{z}(0)} & \frac{\partial s(t)}{\partial \mathbf{z}(0)} & \frac{\partial \bar{\mathbf{z}}(t)}{\partial \mathbf{z}(0)} & \frac{\partial \bar{s}(t)}{\partial \mathbf{z}(0)} \\ \frac{\partial \mathbf{z}(t)}{\partial s(0)} & \frac{\partial s(t)}{\partial s(0)} & \frac{\partial \bar{\mathbf{z}}(t)}{\partial s(0)} & \frac{\partial \bar{s}(t)}{\partial s(0)} \\ \frac{\partial \mathbf{z}(t)}{\partial \bar{\mathbf{z}}(0)} & \frac{\partial s(t)}{\partial \bar{\mathbf{z}}(0)} & \frac{\partial \bar{\mathbf{z}}(t)}{\partial \bar{\mathbf{z}}(0)} & \frac{\partial \bar{s}(t)}{\partial \bar{\mathbf{z}}(0)} \\ \frac{\partial \mathbf{z}(t)}{\partial \bar{s}(0)} & \frac{\partial s(t)}{\partial \bar{s}(0)} & \frac{\partial \bar{\mathbf{z}}(t)}{\partial \bar{s}(0)} & \frac{\partial \bar{s}(t)}{\partial \bar{s}(0)} \end{pmatrix} = \begin{pmatrix} \frac{\partial \dot{\mathbf{z}}(t)}{\partial \mathbf{z}(0)} & \frac{\partial \dot{s}(t)}{\partial \mathbf{z}(0)} & \frac{\partial \dot{\bar{\mathbf{z}}}(t)}{\partial \mathbf{z}(0)} & \frac{\partial \dot{\bar{s}}(t)}{\partial \mathbf{z}(0)} \\ \frac{\partial \dot{\mathbf{z}}(t)}{\partial s(0)} & \frac{\partial \dot{s}(t)}{\partial s(0)} & \frac{\partial \dot{\bar{\mathbf{z}}}(t)}{\partial s(0)} & \frac{\partial \dot{\bar{s}}(t)}{\partial s(0)} \\ \frac{\partial \dot{\mathbf{z}}(t)}{\partial \bar{\mathbf{z}}(0)} & \frac{\partial \dot{s}(t)}{\partial \bar{\mathbf{z}}(0)} & \frac{\partial \dot{\bar{\mathbf{z}}}(t)}{\partial \bar{\mathbf{z}}(0)} & \frac{\partial \dot{\bar{s}}(t)}{\partial \bar{\mathbf{z}}(0)} \\ \frac{\partial \dot{\mathbf{z}}(t)}{\partial \bar{s}(0)} & \frac{\partial \dot{s}(t)}{\partial \bar{s}(0)} & \frac{\partial \dot{\bar{\mathbf{z}}}(t)}{\partial \bar{s}(0)} & \frac{\partial \dot{\bar{s}}(t)}{\partial \bar{s}(0)} \end{pmatrix} \begin{pmatrix} \frac{\partial \mathbf{z}(t)}{\partial \mathbf{z}(0)} & \frac{\partial s(t)}{\partial \mathbf{z}(0)} & \frac{\partial \bar{\mathbf{z}}(t)}{\partial \mathbf{z}(0)} & \frac{\partial \bar{s}(t)}{\partial \mathbf{z}(0)} \\ \frac{\partial \mathbf{z}(t)}{\partial s(0)} & \frac{\partial s(t)}{\partial s(0)} & \frac{\partial \bar{\mathbf{z}}(t)}{\partial s(0)} & \frac{\partial \bar{s}(t)}{\partial s(0)} \\ \frac{\partial \mathbf{z}(t)}{\partial \bar{\mathbf{z}}(0)} & \frac{\partial s(t)}{\partial \bar{\mathbf{z}}(0)} & \frac{\partial \bar{\mathbf{z}}(t)}{\partial \bar{\mathbf{z}}(0)} & \frac{\partial \bar{s}(t)}{\partial \bar{\mathbf{z}}(0)} \\ \frac{\partial \mathbf{z}(t)}{\partial \bar{s}(0)} & \frac{\partial s(t)}{\partial \bar{s}(0)} & \frac{\partial \bar{\mathbf{z}}(t)}{\partial \bar{s}(0)} & \frac{\partial \bar{s}(t)}{\partial \bar{s}(0)} \end{pmatrix}. \tag{2.20}$$

The integration of the matrix equation, which scales as $(N+1)^3$, is the most expensive step in the SC calculation. The extra phase ϕ_e in equation 2.19 is

$$\phi_e = -\frac{1}{4}\mathrm{Tr}\int_0^t d\tau \left[\left(\frac{\partial \dot{\mathbf{z}}}{\partial \mathbf{z}} - \frac{\partial \dot{\bar{\mathbf{z}}}}{\partial \bar{\mathbf{z}}}\right) + \left(\frac{\partial \dot{s}}{\partial s} - \frac{\partial \dot{\bar{s}}}{\partial \bar{s}}\right) \right]. \tag{2.21}$$

It has been noticed before[75] that if one replaces the matrix element of the quantum Hamil-

tonian by the Weyl Hamiltonian:

$$\begin{aligned} H(\mathbf{z}, s, \bar{\mathbf{z}}, \bar{s}) &= \frac{(\bar{\mathbf{z}}^*, \bar{s}^* | \hat{H}(\hat{\mathbf{q}}, \hat{\mathbf{p}}) | \mathbf{z}, s)}{(\bar{\mathbf{z}}^*, \bar{s}^* | \mathbf{z}, s)} \\ &\downarrow \\ H_W(\mathbf{q}, \mathbf{p}, s, \bar{s}) &= \frac{(\bar{s}^* | \hat{H}_W(\mathbf{q}, \mathbf{p}) | s)}{(\bar{s}^* | s)}, \end{aligned} \tag{2.22}$$

where $\mathbf{q} = \frac{\mathbf{z}+\bar{\mathbf{z}}}{\sqrt{2}}$ and $\mathbf{p} = \frac{\mathbf{z}-\bar{\mathbf{z}}}{i\sqrt{2}}$, the error made during this process, to leading order in $\hbar$, cancels the first term in the extra phase. Hence one can avoid evaluating the matrix element of the Hamiltonian by using the Weyl Hamiltonian with a different extra phase $\tilde{\phi}_e$

$$\tilde{\phi}_e = -\frac{1}{4} \int_0^t d\tau \left(\frac{\partial \dot{s}}{\partial s} - \frac{\partial \dot{\bar{s}}}{\partial \bar{s}} \right). \tag{2.23}$$

This provides a huge advantage in practical calculations since the evaluation of the matrix element of the quantum Hamiltonian requires integration over the nuclear phase space and will be extremely difficult in multidimensional systems whereas the Weyl Hamiltonian only requires knowing the classical Hamiltonian at one point $(\mathbf{q}, \mathbf{p})$ in the phase space. The Weyl Hamiltonian with the extra phase $\tilde{\phi}_e$ is used through out our calculations.

The root search problem

The major problem that arises from the SC approximation is the root search problem, i.e., one needs to find the initial values of $\bar{\mathbf{z}}(0)$ and $\bar{s}(0)$ such that the final boundary condition is satisfied:

$$\begin{aligned} \bar{\mathbf{z}}(t; \mathbf{z}(0), s(0), \bar{\mathbf{z}}(0), \bar{s}(0)) &= \mathbf{z}_f^* \\ \bar{s}(t; \mathbf{z}(0), s(0), \bar{\mathbf{z}}(0), \bar{s}(0)) &= s_f^*. \end{aligned} \tag{2.24}$$

In general the above equations are nonlinear in $\bar{\mathbf{z}}(0)$ and $\bar{s}(0)$ and require some iterative method to solve. In most problems, the number of solutions is more than one and in prin-

ciple one needs to find all such solutions and sum up the amplitudes to obtain the full SC propagator. In general, finding all solutions would require a global search and clearly it is not feasible for multi-dimensional systems. Furthermore, the number of solutions to equation 2.24 can be in the order of thousands just after a few vibrational periods in multi-dimensional systems. Hence even if all solutions were known, adding up all amplitudes with possible smoothing would still be a formidable task. So in practice one would prefer some local search method that finds a few solutions that contribute significantly to the SC propagator.

As we pointed out previously, the nuclear positions and momenta are complex in general. Only when the initial conditions are $\bar{\mathbf{z}}(0) = \mathbf{z}^*(0)$ and $\bar{s}(0) = s^*(0)$, it is clear from equation 2.14 that the nuclear positions and momenta will remain real valued. This type of trajectory is of particular importance and will be referred to as a "real trajectory". It has been pointed out that for single surface dynamics, only solutions that start close to the real trajectory ($\bar{\mathbf{z}}(0) \approx \mathbf{z}(0)^*$) contribute significantly to the SC propagator[68, 67], mainly due to the overlap term in the action (equation 2.18): the SC amplitude decays exponentially as a function of the magnitude of $\mathbf{v}$ in equation 2.9. Hence one can take the real trajectory as an initial guess and use the Newton-Raphson (NR)[76] procedure to search for the exact solutions as long as the real trajectory gets close to the correct boundary conditions. This search algorithm has been applied to the multi-dimensional single-surface models and found successful[68]. Now we simply extend this "real trajectory search" algorithm to multi-surface systems with the definition of the real trajectory extended to the electronic degrees of freedom. In practice we find this "real trajectory search" algorithm works well for the non-adiabatic case, i.e. the NR procedure still converges to the important complex solutions starting from the real trajectory as a guess. However, unlike the single surface case, in some of these solutions, $\bar{s}(0)$ and $s^*(0)$ are significantly different from each other (far away from the real trajectory) but the amplitude obtained from such solutions can still strongly contribute to the SC propagator. One explanation is that the spin overlap term in the action does not make the

amplitude decay exponentially as a function of the distance between $\bar{s}(0)$ and $s^*(0)$, unlike in the case of nuclear degrees of freedom. Therefore one should not expect this term to strongly control the magnitude of the SC amplitude. The reason that the algorithm can still find these complex solution is possibly due to the fact that in two-state systems the search space for the spin variable is small enough for the NR procedure to always land on some solutions, real or complex. However, since in most applications the number of electronic states is usually small (two or three in most cases), we expect the "real trajectory search" algorithm will still work.

The computational cost of the root search depends on the cost of the NR procedure and the number of branches that are needed to construct SC correlation function. The NR procedure requires the stability matrix, which is also needed to compute the fluctuation determinant, hence the numerical effort of performing the NR procedure also scales as $(N+1)^3$. It is often difficult to foresee how many branches are necessary to be found. But previous applications to multiple dimensional Henon-Heiles systems[68] have shown that the number of relevant branches do not increase exponentially, if not at all, as the system dimensionality grows.

Finally, we note that under the real trajectory conditions, the Weyl Hamiltonian is exactly the mean field Hamiltonian used in the Ehrenfest method. Hence what we call a real trajectory is actually an Ehrenfest trajectory.

2.3 applications to test systems

In order to test the SC propagator, we applied it to the 3 scattering models proposed by Tully[46], namely the single avoided crossing, dual avoided crossing and extended coupling models. The non-analytic potential energy functions in Tully's original models are problematic. Since the SC propagator requires analytic continuation of the potential energy functions to be be carried out for complex valued $\mathbf{q}$, these potentials must be analytic. This will not

be a problem in *ab initio* calculations, where the potential energy is given as the root of a polynomial equation, giving a rigorously analytic energy expression. For the present case, we have simply replaced the implicit functions (e.g. a piece-wise exponential) with smooth analogs (e.g. a hyperbolic tangent). In all 3 cases, a wavepacket of the form $|\psi_i\rangle = |z_i, s_i = 0\rangle$ starts on the lower surface in the asymptotic region to the left. The mass of the particle is set to 2000, as in the original models.

Transmission and reflection probabilities from the lower electronic surface to both lower and upper surfaces as a function of the initial energy are calculated and compared to the quantum results. Such probability can be written in terms of the matrix element of a projection operator:

$$P = \lim_{t\to\infty} \langle\psi_i|e^{iHt}\hat{\mathbf{P}}e^{-iHt}|\psi_i\rangle, \tag{2.25}$$

where the projection operator $\hat{\mathbf{P}}$ is :

$$\hat{\mathbf{P}} = |n\rangle\langle n|\theta(\pm\hat{q}), \tag{2.26}$$

where $|n\rangle$ is the target electronic state and the step function θ takes the minus sign for reflection events and plus sign for transmission events. Since our method calculates the matrix elements of the propagator directly, it is desirable to write these probabilities in terms of the propagator. First we write a resolution of identity in terms of coherent states:

$$\hat{I} = \sum_m \sum_{\alpha,\beta} |z_\alpha, m > S^{-1}_{\alpha,\beta} < z_\beta, m|, \tag{2.27}$$

where $z_\alpha = \frac{q_\alpha + ip_\alpha}{\sqrt{2}}$ and $S_{\alpha,\beta} = \langle\mathbf{z}_\alpha|\mathbf{z}_\beta\rangle$. Due to the over-completeness of the coherent states, there are an infinite number of ways of choosing z_α's. For convenience we choose to scan over the position coordinate and keep the value of p_α's constant. The action of the projection

operator on the resolution of identity is:

$$\hat{\mathbf{P}}\hat{I} = \sum_{\alpha,\beta} |z_\alpha, n\rangle S^{-1}_{\alpha,\beta} \langle z_\beta, n|, \tag{2.28}$$

where q_α's are positive for transmission events and negative for reflection events and the value of p_α is chosen such that the total energy is conserved. Thus equation 2.25 can be rewritten in terms of the coherent state propagator as:

$$\begin{aligned} P &= \lim_{t\to\infty} \sum_{\alpha,\beta} \langle \psi_i | e^{iHt} | z_\alpha, n\rangle S^{-1}_{\alpha,\beta} \langle z_\beta, n | e^{-iHt} | \psi_i \rangle \\ &= \lim_{t\to\infty} \sum_{\alpha,\beta} U^*_{i,\alpha}(t) S^{-1}_{\alpha,\beta} U_{\beta,i}(t), \end{aligned} \tag{2.29}$$

where the propagator $U_{\beta,i}(t) = \langle z_\beta, n | e^{-iHt} | \psi_i \rangle$ is directly calculated from the SC approximation. The inversion of the overlap matrix is via the SVD method to remove near linear dependence of the canonical coherent states.

For the purpose of comparison, we also compute the same quantities using the Ehrenfest method and the SH method. In the Ehrenfest calculations, initial conditions of the classical variables are sampled from the Wigner distribution of the initial wavepacket. The "fewest switches" algorithm[46] is used in the SH calculations. For both methods, 2000 trajectories were run to obtain statistically significant results. Finally, Sun and Miller have applied the mapping SC-IVR method discussed in the introduction to the same three model systems[6]. As we present our results, we will also point out important physical similarities and differences between the two methods.

As mentioned before, in general it is not clear how many relevant branches will be needed. For one dimensional scattering systems, one expects the number of branches to be only a few. In actual calculations, we found in almost every case a single branch is enough to give accurate SC approximation. In results presented below, unless otherwise stated, the number of branches included in the SC approximation is one.

2.3.1 Single avoided crossing

The diabatic potentials are:

$$\begin{aligned} V_{00} &= A\tanh(Bq) \\ V_{01} &= Ce^{-Dq^2} \\ V_{11} &= -V_{00} \end{aligned}$$

where $A = 0.01$, $B = 1.6$, $C = 0.005$ and $D = 1.0$.

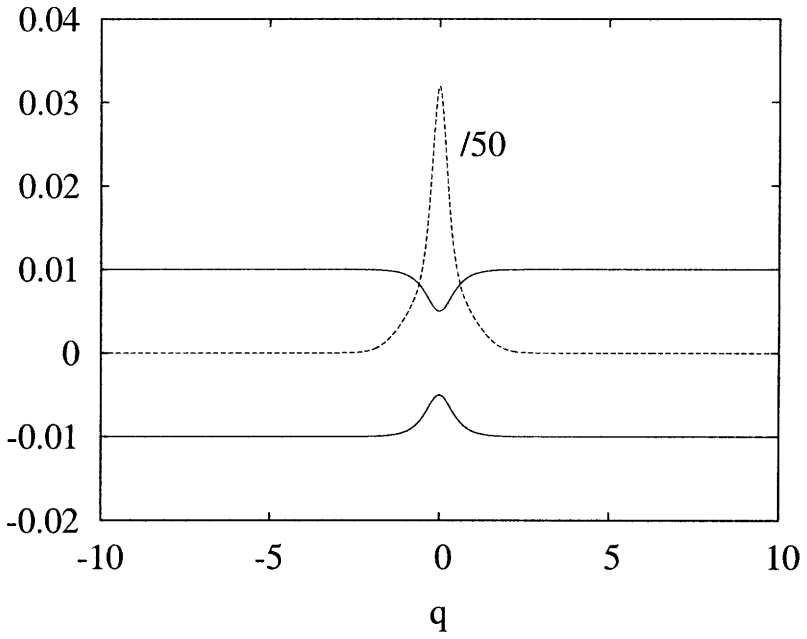

Figure 2.1: The adiabatic surfaces (solid lines) and the coupling strength (dashed line) for the single avoided crossing model.

Figures 2.2 and 2.3 show that the SC results are quantitative at high energies, down to $p_0 = 10$. The results from the Ehrenfest, the SH and the mapping SC-IVR calculations are also accurate in this energy range[6]. This is expected since at sufficiently high momenta, the dynamics is essentially classical and all classically based methods should reach the same limit. As p_0 drops below the upper surface barrier, the lower→upper transmission probabilities soon drop to zero. In figure 2.3, the SH results show a discontinuity as a direct result of classical

energy conservation while the SC method predicts a more smooth curve. This demonstrates that the SC method correctly predicts the energy barrier and is able to include the WKB-type tunneling effects. The same feature is observed in the mapping SC-IVR results[6], indicating this is a typical feature of SC approaches . In the Ehrenfest method, however, the mean field has a lower barrier than the actual upper surface and hence it predicts much higher transmission probabilities. This is also shown in figure 2.3, where the predicted barrier from the Ehrenfest method is at $p_0 \approx 5$, which corresponds to the lower surface barrier, rather than the actual upper barrier at $p_0 \approx 9$. As a result, the lower→lower transmission probabilities (figure 2.2), in the range from $p_0 \approx 5$ to $p_0 \approx 9$, are underestimated in the Ehrenfest model.

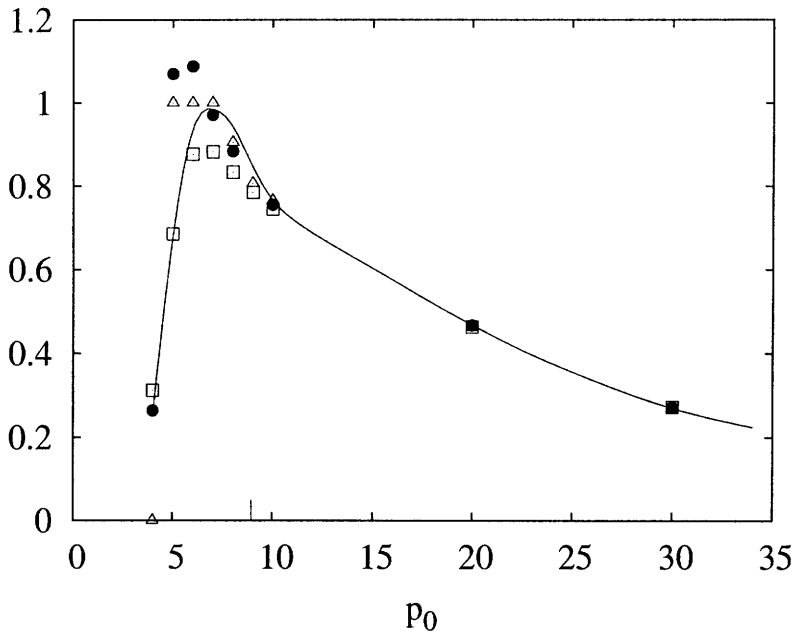

Figure 2.2: Single avoided crossing model, lower-lower transmission probability. The solid line is the quantum mechanical results, unfilled squares are the Ehrenfest results, unfilled triangles are the SH results and solid circles are the SC results. The hash mark corresponds to the upper surface barrier ($E_0 = 0.02$).

A closer look at figure 2.2 shows the SC lower→lower transmission probability at $p_0 = 8$ is slightly lower than the quantum result. To the see the origin of this inaccuracy, we plot the absolute value of the quantum and the SC wavefunctions in figure 2.4. The quantum wavefunction has two peaks, indicating the wavepacket is temporarily trapped inside the

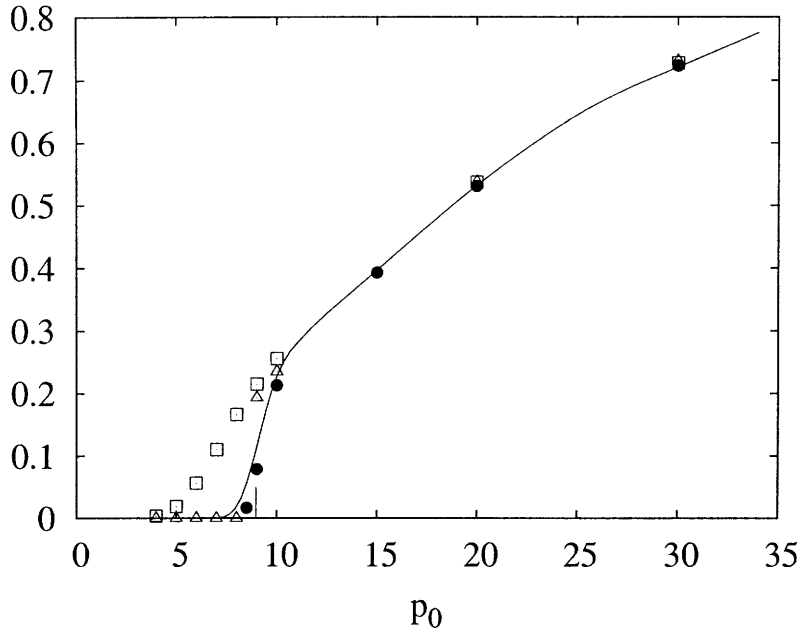

Figure 2.3: Single avoided crossing model, lower-upper transmission probability. The solid line is the quantum mechanical results, unfilled squares are the Ehrenfest results, unfilled triangles are the SH results and solid circles are the SC results.The hash mark corresponds to the upper surface barrier ($E_0 = 0.02$).

well on the upper adiabatic surface and escapes from it in series during each oscillation. The SC branch in figure 2.4 captures the first escaped portion and misses the ones that arrive later. This results in a slightly smaller transmission probability. Another error evident in figure 2.2 is that the probabilities at $p_0 = 5$ and $p_0 = 6$ are greater than 1. This is explained in figure 2.5, where we plot the absolute value of the quantum and SC wavefunctions at $p_0 = 5$. The peak on the SC wavefunction is due to nearby caustics, which makes the determinant in equation 2.19 nearly zero. This introduces a big error into the integration of the SC wavefunction and the resulting probability becomes greater than 1. We note that the mapping SC-IVR also gives probabilities greater than 1 in the same momentum range[6], although the errors are smaller. At p_0 below 5, only reflection on the lower surface is accessible to the wavepacket and all methods, again, give accurate answers.

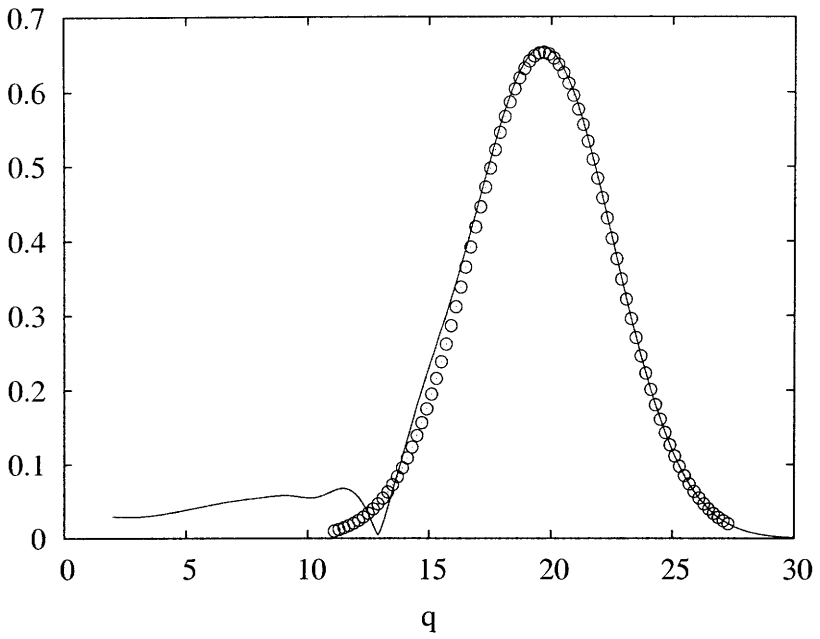

Figure 2.4: Magnitude of the spatially resolved wave function: $\left|\langle q,p_f,\text{lower}|e^{-i\hat{H}t}|q_0,p_0,\text{lower}\rangle\right|$, where $q_0 = -8$, $p_0 = 8$, $p_f = 8$ and $t = 3400$ au. The solid line is the quantum result and empty circles are the SC result. The SC correlation function misses the later recurrences from resonances.

2.3.2 Dual avoided crossing

The diabatic potentials are:

$$\begin{aligned} V_{00} &= 0 \\ V_{01} &= Ce^{-Dq^2} \\ V_{11} &= -Ae^{-Bq^2} + E_0, \end{aligned}$$

where $A = 0.1$, $B = 0.28$, $E_0 = 0.05$, $C = 0.015$ and $D = 0.06$.

Figure 2.7 shows the lower-lower transmission probabilities. The SC calculations are accurate for all energies above the classical barrier ($\log E = -3$) while the SH and Ehrenfest results start to be less accurate at $\log E < -1$. This shows that the quantum interference effects (Stueckelberg oscillations[77]) are well captured by the SC approximation. This is

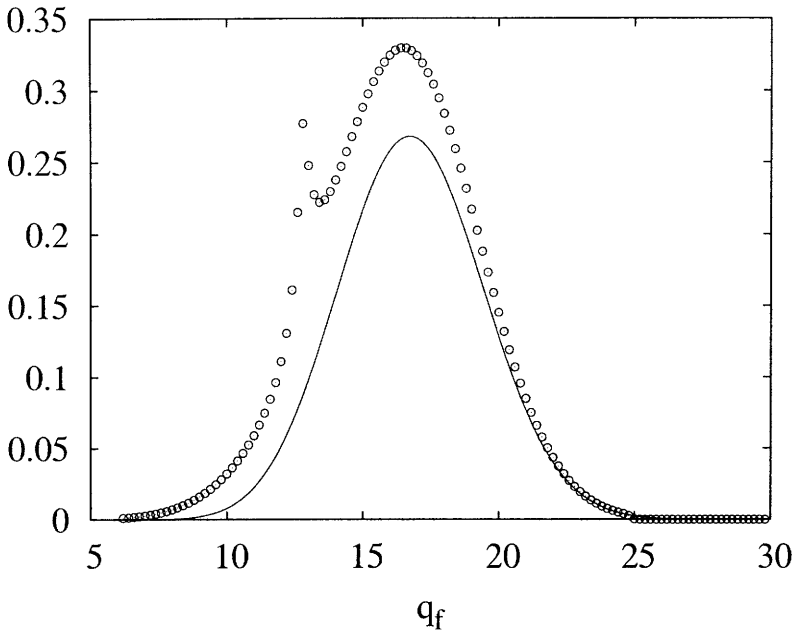

Figure 2.5: Magnitude of the spatially resolved wave function: $\left|\langle q,p_f,\text{lower}|e^{-i\hat{H}t}|q_0,p_0,\text{lower}\rangle\right|$, where $q_0 = -8$, $p_0 = 5$, 5 and $t = 1000$ au. The solid line is the quantum result and empty circles are the SC result.

mainly due to the phase information provided by the SC propagator, which is ignored by both Ehrenfest and SH method. Also, in the SC treatment, the transition from the lower to the upper surface is continuous via a particular Weyl Hamiltonian adjusted for the boundary conditions. Transitions in the Ehrenfest method are also continuous but it predicts a final state in which a single particle populates both surfaces. Therefore the mean field used in the Ehrenfest method is not ideally suited to describe a particle ending up on a single surface. On the other hand, the SH method does cause the particle to transmit to a single asymptotic surface but it destroys some quantum coherence when a sudden switch is made. Therefore neither of these two methods shows the correct Stueckelberg oscillations, especially at lower energies. The mapping SC-IVR also shows correct oscillatory behavior of the transmission probabilities at $\log E > -2$ but gives inaccurate results at lower energies[6]. Thus, we see that SC methods typically give a better description of interference effects than their mixed-quantum-classical counterparts, which should be expected. The inaccuracy of the mapping

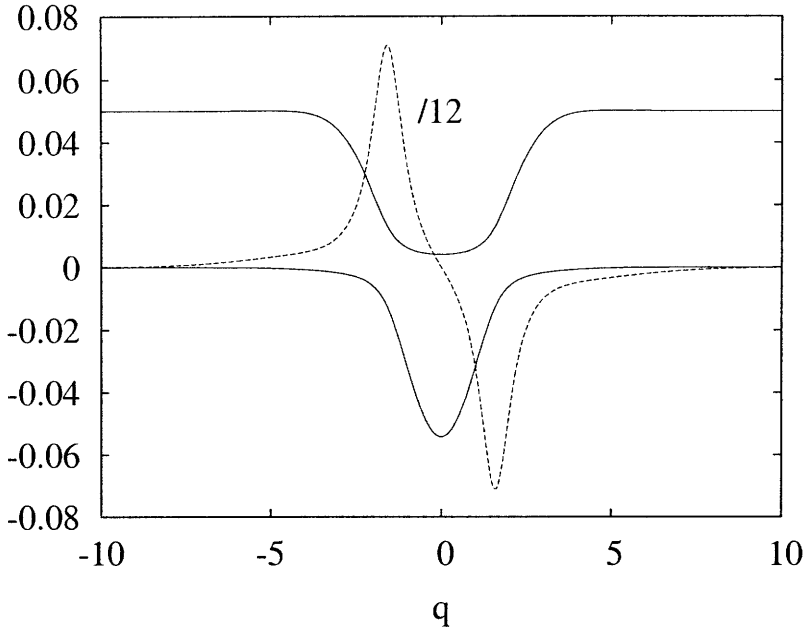

Figure 2.6: The adiabatic surfaces (solid lines) and the coupling strength (dashed line) for the dual avoided crossing model.

SC-IVR for $-3 < \log E < -2$ may be due to the divergent behavior of the fluctuation determinant at long time[6].

In the lower upper transmission calculations, figure 2.8 shows the SC method starts to fail at higher energies ($\ln E \approx -2$) than it did in the lower lower transmission calculations. The Ehrenfest and SH results start to show inaccurate oscillations at roughly the same energy. Thus we see an immediate drawback of the SC method: since there are no reflections, the probabilities of ending up on the upper and lower surface should add up to 1. However, this is not true for the SC results below $\ln E = -2$. The lack of norm conservation is due to the exclusion of non-stationary paths[47] in the path integral. The norm-conservation in our SC formulations is only correct to within the stationary path approximation. In the higher energy ($\log E > -2$) portion of figure 2.7 and 2.8, where the energy of the wavepacket is well above the barrier top, we see probabilities are well conserved. At lower energies, when the quadratic approximation of the path integral in equation 2.11 becomes inadequate and higher terms need to be taken into consideration, the SC propagator starts to lose probability

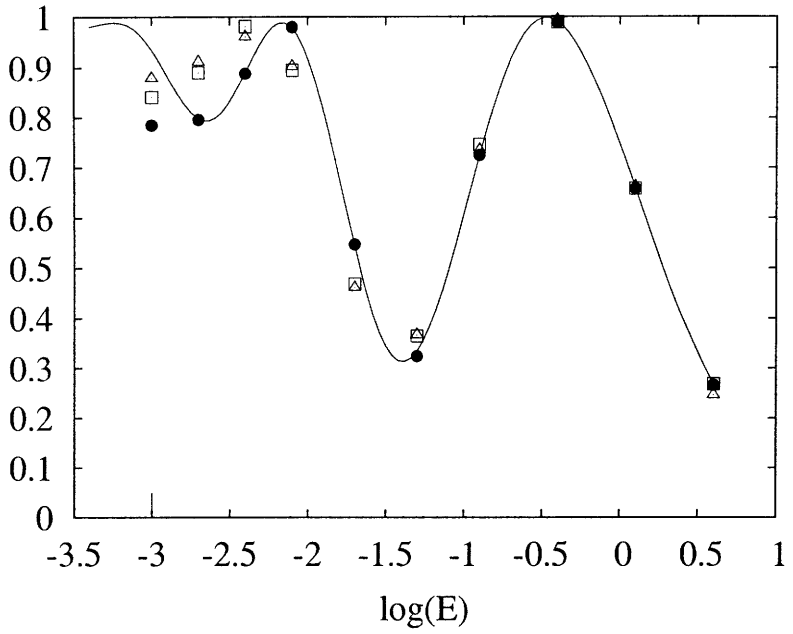

Figure 2.7: Dual avoided crossing model, lower-lower transmission probability. Lines are the quantum mechanical results, unfilled squares are the Ehrenfest results, unfilled triangles are the SH results and solid circles are the SC results. The harsh mark corresponds to the upper surface barrier ($E = 0.05$).

conservation. The mapping SC-IVR results[6] also lack norm conservation at $\log E < -2$ and we expect this to be common for other SC-IVR methods[50, 7, 63] as well.

2.3.3 Extended coupling

The diabatic potentials are:

$$\begin{aligned} V_{00} &= -A \\ V_{01} &= B(\tanh(Cq) + 1) \\ V_{11} &= A, \end{aligned}$$

where $A = 0.0006$, $B = 0.1$ and $C = 0.9$.

Our SC method, the Ehrenfest method and the SH method all produce accurate lower-lower transmission probabilities (figure 2.10). However, the Ehrenfest method greatly over-

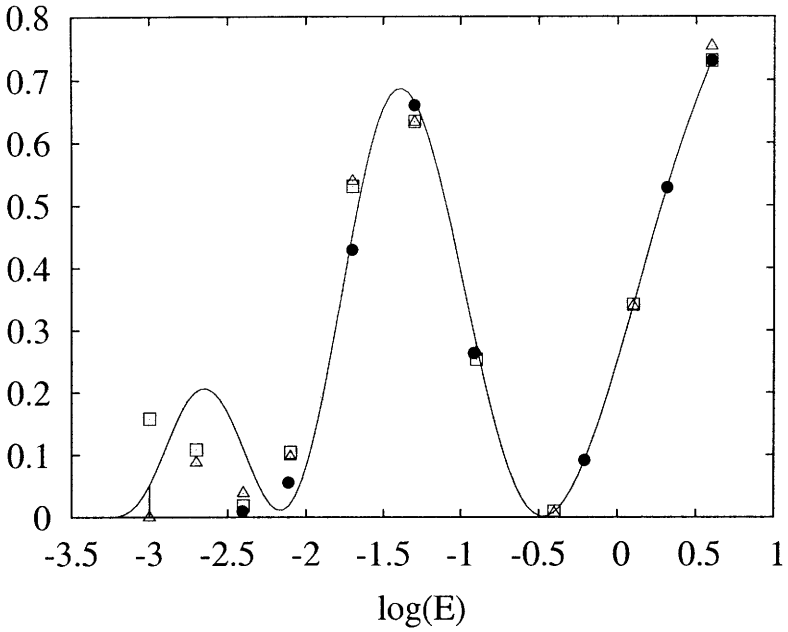

Figure 2.8: Dual avoided crossing model, lower-upper transmission probability. The solid line is the quantum mechanical results, unfilled squares are the Ehrenfest results, unfilled triangles are the SH results and solid circles are the SC results. The hash mark corresponds to the upper surface barrier ($E = 0.05$).

estimates the lower-upper transmission probabilities for $p_0 < 25$ (figure 2.11). Similar to the single avoided crossing model, in which the mean field has a much lower energy barrier than the actual barrier of the upper surface, the Ehrenfest method shows no barrier at all in this model. The SC results are much better. Figure 2.11 shows an exponential decaying SC probability of upper surface transmission around the energy barrier. Hence we see even when the mean field is quite unphysical, the SC method is still able to describe the dynamics well. The SC results, however, decay at slightly higher initial momenta than the actual barrier, $p_0 \approx 28.3$. This inaccuracy in the SC lower-upper transmission probabilities arises from caustics. The probabilities at $p > 33$ in figure 2.11 are from one branch, meaning the initial conditions from which the SC propagators are computed are a continuous connected family. When continuing this branch to $p_0 = 32$, a strong peak in the wavefunction from nearby caustics is found. This is a strong indication that there exist other branches close to each other in phase space. Across $p_0 = 32$, this branch picks up a damping factor and gives a

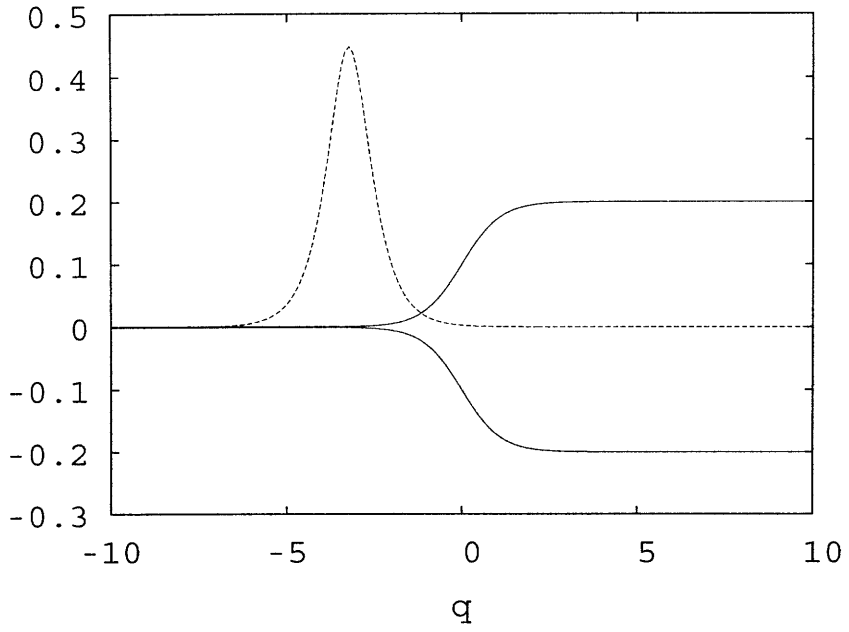

Figure 2.9: The adiabatic surfaces (solid lines) and the coupling strength (dashed line) for the extended coupling with reflection model.

small amplitude and at the same p_0, another branch is found to give larger amplitudes. The probabilities at $p_0 < 32$ shown in figure 2.11 are from this new branch. In this particular case, $p_0 = 32$ can be considered as a branch cut point[78], where one branch provides accurate approximations on one side of it and damped results on the other side. The importance of branches alternates across this cut. In this case, we cannot compare our method to the mapping SC-IVR because for this model, the only SC-IVR calculations involve transitions between diabatic states, which makes comparison difficult[6].

The appearance of caustics, in our SC approximation, is commonly seen when the initial energy is near the energy barrier of the upper surface. In this particular example, suppose a wavepacket starts with $p_0 = 30$ on the lower surface. It transmits to the lower surface with a final momentum at $p_f \approx 41$ and to the upper surface at $p_f \approx 10$. Figure 2.10 and 2.11 show that the SC method performs well for the former event but not so well for the latter. The reason is that the former event is closer to the Ehrenfest prediction so that only a small modification of the mean field is needed to construct the Weyl Hamiltonian. In the case of

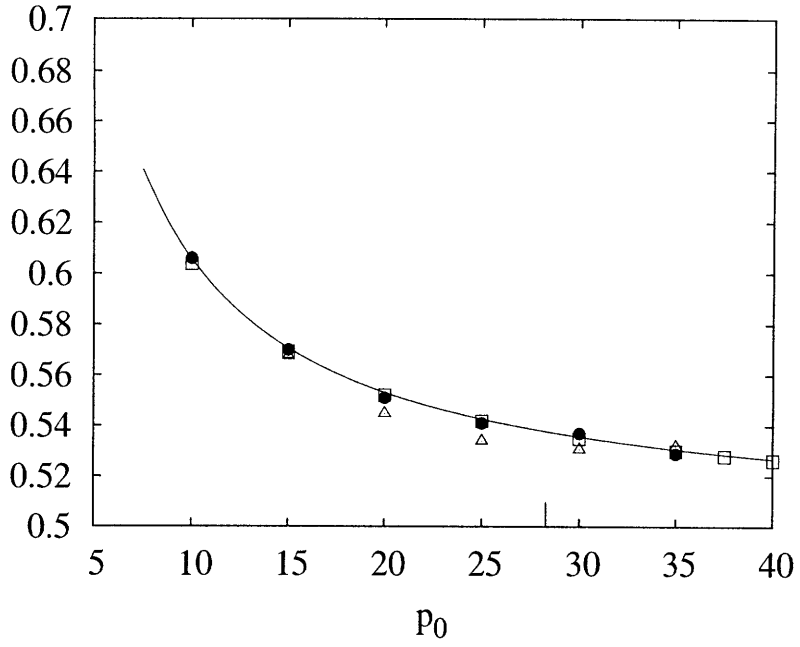

Figure 2.10: Extend coupling with reflection model, lower-lower transmission probability. The solid line is the quantum mechanical results, unfilled squares are the Ehrenfest results, unfilled triangles are the SH results and solid circles are the SC results. The hash mark corresponds to the upper surface barrier ($E = 0.2$).

the lower upper transmission event, however, one can imagine a rather large modification must be made in order to change the final momentum of the particle from 41 to 10. Caustics are often visible under such situations and more than one branch is often found. As a result, the SC amplitude becomes less accurate. For example, in this model, the SC lower upper transmission probability at $p_0 = 30$ is damped (figure 2.11) and we have found two branches at this initial momentum.

When the behaviors of wavepackets on different surfaces become physically distinct (one part transmits and one reflects), we see the appearance of multiple branches. For instance, in the calculations of reflection probabilities with $p_0 = 15$, we have found many different reflected branches. Figure 2.12 shows 3 branches we found when computing the SC correlation functions of that reflection event. No caustics are found in any of these branches and therefore they are well separated from each other. They all seem to carry some significant weights, but, unfortunately, the sum of them does not seem to reproduce the quantum wave-

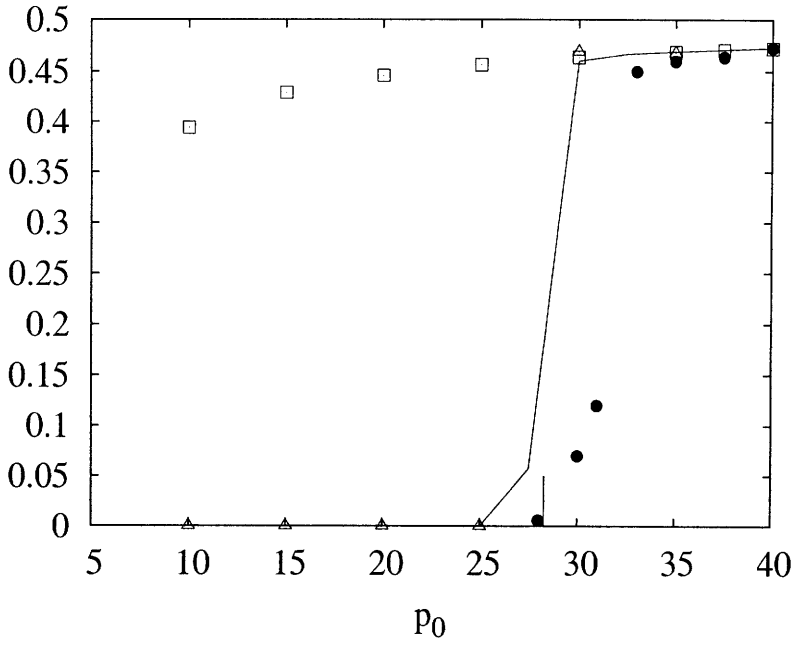

Figure 2.11: Extended coupling with reflection model, lower-upper transmission probability. The solid line is the quantum mechanical results, unfilled squares are the Ehrenfest results, unfilled triangles are the SH results and solid circles are the SC results. The hash mark corresponds to the upper surface barrier ($E = 0.2$).

function. This is true for all reflection energies. At this point, there is no clear indication whether we have found all branches or not. Also it is hard to tell which branch should be included in the sum to recover the full SC propagator. For these reasons, we do not present the SC reflection probabilities but conclude our SC propagator is not well-suited to the task.

2.4 discussions

Our method is closely related to the Ehrenfest method and may be viewed as a generalization of it. In the Ehrenfest method, a single set of initial conditions determines the evolution of the wavepacket. Hence the mean field that governs the dynamics is entirely determined by the initial conditions regardless of the final conditions. One consequence is that the Ehrenfest method does not satisfy microscopic reversibility[18, 8]. As a result, detailed balance is not satisfied by the Ehrenfest method. On the other hand, the Weyl Hamiltonian in the SC

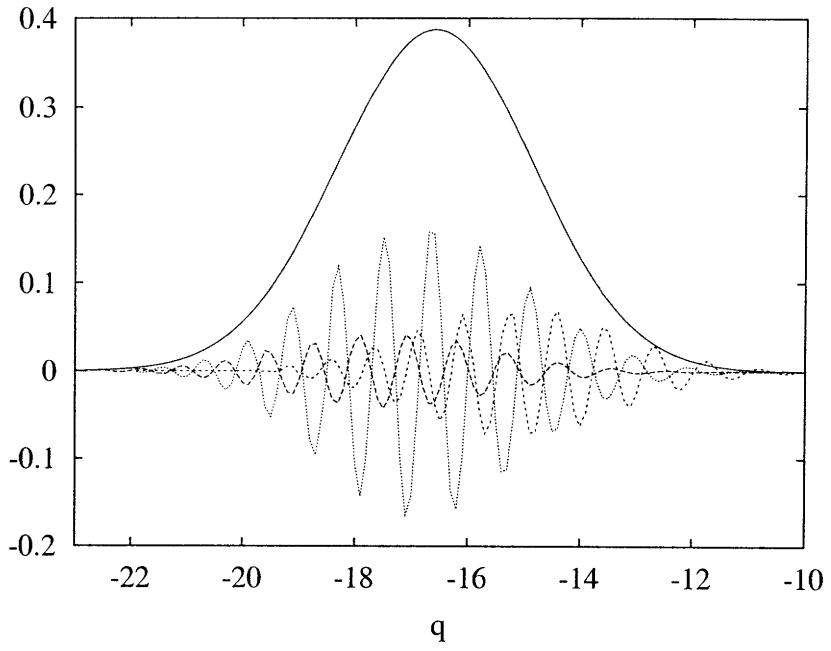

Figure 2.12: The spatially resolved wave function: $\langle q, p_f, \text{lower}|e^{-i\hat{H}t}|q_0, p_0, \text{lower}\rangle$, where $q_0 = -8$, $p_0 = 15$, $p_f = -15$ and $t = 4000$ au. The solid line is the magnitude of the wavefunction from the quantum calculation and the broken lines are the real part of the wavefunction from three SC branches. It seems all 3 branches carry some significant portion of the total amplitude.

propagator is determined by both initial conditions and final conditions. The SC propagator satisfies time reversal symmetry since the initial conditions and final conditions come in pairs: the initial conditions become the final conditions when the dynamics is run backward in time and the final conditions become the initial conditions. This initial-final conditions interchange results in a complex conjugation of the Weyl Hamiltonian, which is precisely what time reversal requires and the detailed balance is thus satisfied. We also note that our Weyl Hamiltonian is very similar to the "Pechukas force"[55]. The only difference is that the derivation of Pechukas follows the strict stationary phase approximation and only the real part of the action is made stationary while in our formulation the whole complex action is subject to the stationary condition.

In terms of results, we note that in all testing cases, whenever the Ehrenfest results are accurate, so is the SC propagator. In the cases where the Ehrenfest fails, the SC results

can still be quantitative, as can be seen from figure 2.7. The SC method faces problems when the mean field becomes a poor reference. In that case, one can imagine that a rather larger modification to the mean field is needed to construct the Weyl Hamiltonian. In another word, since the solution is far away from the starting point, one would expect to see nonlinear behaviors, i.e., caustics and multiple branches. The former is often seen when the mean field prediction just starts to differ from the final boundary conditions. For example, in the single avoided crossing model, when the initial energy of the wavepacket is near the energy barrier of the upper surface such that the final momentum on the upper surface is much lower than what the mean field predicts, caustics will be visible on the SC wavefunction. Figure 2.5 provides a good example of this. When the mean field becomes poorer and predicts significantly different final wavepacket than what the final boundary conditions require, nonlinear effects become stronger and multiple branches appear. An example is the calculation of reflection probabilities in the extended coupling model, where the mean field predicts no reflection at all. We see, in figure 2.12, that several branches all carry some amplitude. Unfortunately the sum does not seem to produce an accurate approximation to the quantum result.

This deficiency can be better understood in an analytically solvable model. Consider two uncoupled harmonic potentials separated horizontally by $2A$ (the mass is set to 1):

$$\begin{aligned} V_{00} &= \frac{1}{2}(q+A)^2 \\ V_{01} &= 0 \\ V_{11} &= \frac{1}{2}(q-A)^2. \end{aligned} \tag{2.30}$$

The Weyl Hamiltonian is:

$$H_w(z,s,\bar{z},\bar{s}) = z\bar{z} + (1+A^2)/2 + qA\frac{s\bar{s}-1}{s\bar{s}+1}. \tag{2.31}$$

The equations of motion for this system are:

$$
\begin{aligned}
\dot{z} &= -i(z+\lambda) \\
\dot{\bar{z}} &= i(\bar{z}+\lambda) \\
\dot{s} &= i2Aqs \\
\dot{\bar{s}} &= -i2Aq\bar{s},
\end{aligned}
\tag{2.32}
$$

where $\lambda = \frac{A}{\sqrt{2}}\frac{s\bar{s}-1}{s\bar{s}+1}$. Since $\frac{d}{dt}(s\bar{s}) = 0$, the wavepacket evolves under a Weyl Hamiltonian with constant weight on each surface. These weights are determined by solving for the initial value of $\bar{s}$. In the Ehrenfest method, the initial value is given by $\bar{s}(0) = s_i^*$, which corresponds to a harmonic oscillator centered at $A\frac{|s_i|^2-1}{|s_i|^2+1}$ while the quantum result is clearly two harmonic oscillators centered at $-A$ and A superimposed together.

To see what the Weyl Hamiltonian gives, we integrate equation 2.32:

$$
\begin{aligned}
z &= (z_i+\lambda)e^{-it} - \lambda \\
\bar{z} &= (z_f^*+\lambda)e^{i(T-t)} - \lambda \\
s &= s_i e^{i2A\int_0^T q(t)dt} \\
\bar{s} &= \bar{s}_0 e^{-i2A\int_0^T q(t)dt}.
\end{aligned}
\tag{2.33}
$$

Applying the boundary condition $\bar{s}(T) = s_f^*$, we have the boundary equation for $\bar{s}(0)$:

$$
\begin{aligned}
\ln(s_f^*/\bar{s}_0) &= 2m\pi i - i\sqrt{2}A \\
&\quad [i(z_i+z_f^*+2\lambda)(e^{-iT}-1) - 2\lambda T]
\end{aligned}
\tag{2.34}
$$

where m is the index of a particular branch of $\ln \bar{s}_0$. If we only consider solving for $\bar{s}_0$ at

periods of the oscillators ($T = 2n\pi$), equation 2.34 can be simplified:

$$\ln(s_f^*/\bar{s}_0) + 2m\pi i = i2TA^2 \frac{\bar{s}_0 s_i - 1}{\bar{s}_0 s_i + 1}. \tag{2.35}$$

If the wavepacket either starts on a single electronic state ($s = 0$ for the right state and $s = \infty$ for the left state) or ends on a single state, it is obvious that the SC result is one branch and exact. However, when the wavepacket start on a mixture of the right and left states (s_i takes a finite nonzero value) and ends on a mixture (s_f is nonzero and finite), this equation is nonlinear and will have different solutions at each different branch surface labeled by m.

To get any further insight, one must solve equation 2.35. Here we calculate the autocorrelation functions of a wavepacket starting on mixed electronic states. With a small mixing (figure 2.13), we can see the presence of several branches and each seems to give an accurate approximation to the quantum result at certain times. The new branches are signaled by the appearance of caustics. When the mixing becomes large (figure 2.14), the branches are well separated. Each branch gives some amplitude, however, in this case it is very difficult to envision the sum of these branches leading to useful result. This is consistent with our observation from the three testing models: a poor mean field reference leads to caustics and eventually multiple branches. Figure 2.13 and 2.14 also show that the superposition principle in quantum mechanics is not obeyed by the SC method:

$$\begin{aligned} \langle z, s|\hat{U}_{SC}(t)|z, s\rangle \quad \neq \quad & \langle z, 0|\hat{U}(t)|z, 0\rangle \\ & + |s|^2 \langle z, 1|\hat{U}(t)|z, 1\rangle, \end{aligned} \tag{2.36}$$

where the results on the left hand side corresponds to the dotted lines in figure 2.13 and 2.14 and the results from the right hand side are exact.

Clearly the quality of the SC propagator depends on the boundary conditions used. In the uncoupled system, it is obvious to use a single electronic state to start with. But in coupled

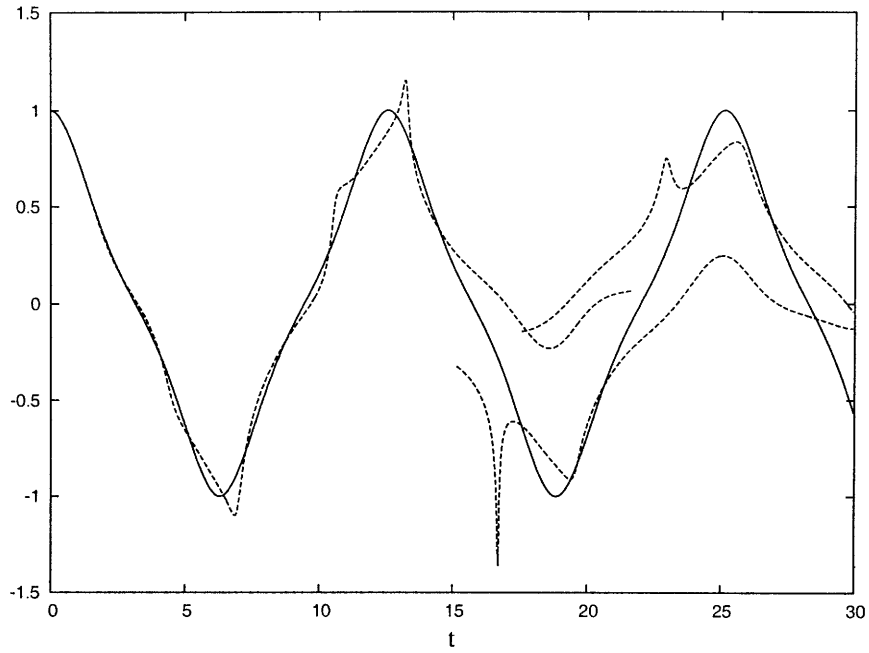

Figure 2.13: The autocorrelation functions of the uncoupled harmonic system, with $q = 1.2$ $p = -0.5$, $s = 0.15$ and $A = 1$. The solid line is the quantum result and dashed lines are SC branches.

systems, for example, in the extended coupling model, even if the wavepacket starts on a single asymptotic state, both electronic states become populated after it travels through the coupling region. So in real calculations, there is not an easy way to pick the correct boundary conditions.

2.5 Conclusions

A SC method of treating nonadiabatic dynamics is presented and tested on model systems. The use of spin coherent states allows the electronic degrees of freedom to be represented by continuous classical-like variables and an exact path integral can be written in the coherent state representation. Our SC propagator is derived as a stationary path approximation (SPA) to the similarity transformed coherent state path integral. The similarity transform we apply to the coherent states is necessary for the SC trajectory to meet arbitrary boundary conditions. The resulting SC propagator obeys time reversal symmetry and detailed balance.

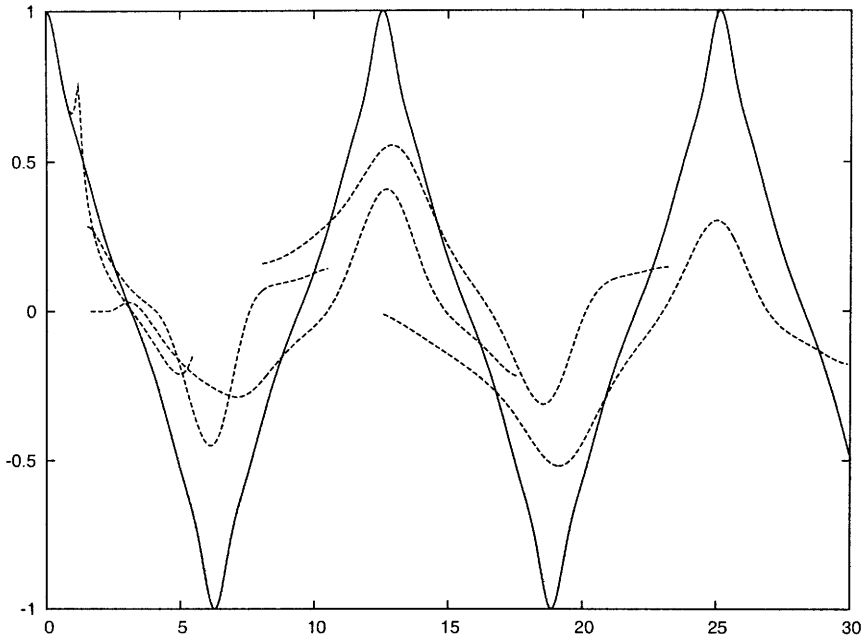

Figure 2.14: The autocorrelation functions of the uncoupled harmonic system, with $q = 1.2$ $p = -0.5$, $s = 0.5$ and $A = 1$.

Our results show the performance of the SC method is quite good when the mean field remains a reliable reference, in accord with early applications using spin coherent states alone to treat electronic structure problems[79]. On the whole, the SC propagator captures quantum interference effects and tunneling is also well-described. These merits are also present in the popular mapping SC-IVR[7, 6], as would be expected from their similar origins: both techniques approximate the quantum propagator via the SPA. In particular, the favorable N^3 scaling of our method with the number of degrees of freedom makes this a very promising method for approximating the nonadiabatic quantum dynamics of large systems.

However, when the mean field becomes a poor reference, problems arise. In all three model problems, we found when the initial energy is near the energy threshold of the upper surface, where the wavepacket on the upper surface has much lower momentum than the wavepacket on the lower surface, strong peaks from caustics are shown on the SC wavefunctions. When the initial momenta are in the range where both transmission and reflection

caused by nonadiabatic transitions are significant, multiple branches start to appear. The amplitudes of these branches all seem to contribute to the total SC propagator and the summation of all such branches do not resemble the quantum answer. Nevertheless, we also found that whenever multiple branches exist, we can always find at least a few of them using the NR procedure, starting from the real trajectory. Hence in practice, the presence of caustics and multiple branches provide us a way to judge the quality of the SC result a priori.

We also showed that multiple branches and caustics are present in uncoupled systems. In the uncoupled harmonic oscillators model (equation 2.31), where the nuclear dynamics is linear, the boundary equation of the spin variables (equation 2.34) is not and gives rise to multiple branches. Depending on the boundary conditions, the SC results can be exact, have peaks from caustics or break into many well separated branches.

In the future, it would be interesting to see how the SC propagator performs in multi-dimensional systems, with the hope that the large phase space may place caustics far away the SC trajectories. Also, ultrafast processes in bound state systems may only require a few nuclear vibrations so the SC formalism may provide more accurate approximations for this type of short time dynamics. A number of such model systems exist and they provide a broad range of testing cases for the SC method[80, 43, 81, 2, 82]. Another direction is to extend the SC treatment to systems with more than two electronic states. The present limitation can be lifted by generalizing the spin coherent state so that an arbitrary number of electronic degrees of freedom can be included. Such extension would allow us to study more complex systems such as the internal conversion in the benzene cation[83].

Chapter 3

A Langevin equation approach to electron transfer reactions in the diabatic basis

3.1 Introduction

The Born-Oppenheimer approximation, in which nuclei are assumed to classically move on a single electronic surface, often suffices to explain many chemical processes. The approximation, however, is not always valid. For example, in an electron transfer (ET) reaction, the transitions between multiple electronic states are inherently quantum mechanical and require treatment beyond Born-Oppenheimer. The need for theoretical understanding of ET reactions is overwhelming because of the important role ET reactions play in many areas of science and engineering, such as in photosynthesis[84], solar cell design[85] and the development of light-emitting devices[86]. Recent observations of vibrational dynamics during the course of electron transfer[87] put further emphasis on the development of appropriate simulation tools. Because it is currently impossible to simulate the quantum dynamics of both electronic and nuclear degrees of freedom for these technologically relevant systems, the most common approach for ET dynamics has historically involved treating the electronic degrees of freedom quantum mechanically while maintaining a classical description

of the nuclei. While this approach is physically appealing due to its close connection with the Born Oppenheimer picture, there is no uniquely defined framework for marrying quantum and classical dynamics. As a consequence, incorporating quantum effects into classical simulation has remained a difficult problem.

There has been, however, much progress toward resolving this problem. Ehrenfest dynamics[14], surface hopping (SH)[3] and *ab initio* multiple spawning (AIMS)[5] have all made important contributions. The surface hopping method is the *de facto* method of choice for describing quantum transitions in the adiabatic basis using classical trajectories. The primary features that recommend surface hopping are: correct thermal relaxation[8], the inclusion of electronic quantum coherence[88] and the relative ease of use. In some ways, AIMS can be thought of as a clever and practical extension of SH. It is actually exact in principle and by careful sampling of the initial wavepackets, one can potentially use a relatively small number of classical trajectories to achieve convergence[89]. One common feature of both methods is the use of adiabatic surfaces to reduce number of hops or spawnings. The adiabatic basis is unappealing for ET reactions, both because one tends to think in terms of *diabatic* ET states rather than adiabats and because the dipole moment operator is discontinuous in the vicinity of a typical conical intersection between adiabats [9]. (In the diabatic basis the transition dipole is smooth over the nuclear coordinate.) Ehrenfest is better for ET reactions in this sense: it can be applied equally well to either the adiabatic or diabatic representation. It also has the advantage that the dynamics conserves total energy and quantum coherences are well preserved. However, it has recently been found to lead to erroneous long time equilibrium in some cases[8] and one needs to be careful whether the mean field approximation in the method is physical. A number of semi-classical methods[7, 90, 4] that can be used to treat ET systems have also been developed . For model systems, quantitative results can often be obtained. For realistic systems, these methods require a very large number of trajectories to converge the results and so far this has limited their application.

Another approach to mixed quantum-classical dynamics - which is essentially indepen-

dent in spirit from the methods above - is to employ Langevin equations or master equations to reduce the dynamics. Techniques in this area include the well known non-interacting blip approximation (NIBA)[26, 32], the Bloch-Redfield equations[38] and the more recent generalizations of the NIBA[30, 31, 36, 35, 29], just to name a few. These equations are often named master equations when dealing with populations and called Generalized Langevin equations or generalized quantum master equations when other observables, such as coherences[38, 40], are included in the equations of motion. This approach has the advantage that the intractable quantum dynamics in multi-dimensional space is condensed to a few relevant memory kernels. These Langevin equations are exact in principle and connect the initial non-equilibrium state and the long time equilibrium state through the balance of fluctuations and frictions[28]. In practice, one cannot obtain the exact memory kernels and a number of methods of approximation have been developed in the hope of obtaining accurate results with a minimum of effort. The common approach is to expand the memory kernels perturbatively. Depending on the particular choice of the perturbation and the way the power series is truncated and summed, various approximate quantum master equations can be derived[32, 31, 38, 29, 35, 36, 91, 92, 93, 40, 30]. The problem in each case is the range of validity: these truncated equations are only valid when the perturbation is small enough. For a given ET system, this may or may not be true and careful justification of the method is needed[27, 94, 95]. The infinite variety of available Langevin equations is both a blessing and a curse. On one hand, there is nearly always a set of Langevin equations that can be formulated for a given problem that will give accurate answers at a reduced cost. However, by the same token, the technical difficulty of deriving the specific equation and approximating its kernel restricts these techniques only to relative experts.

In this chapter, we propose a Generalized Langevin equation that gives accurate short time *and* long time behavior of the population dynamics in an ET reaction. To ensure the correct long time behavior, we choose to evolve the population *fluctuations* around their predicted equilibrium values. In order to estimate the equilibrium populations, we perform

a simple variational calculation for the equilibrium density matrix, where the original Hamiltonian is rotated to the electronic reference frame that minimizes the first order free energy [96, 93]. This serves two purposes. First, the new reference Hamiltonian gives the best approximation to the equilibrium density matrix at zeroth order and provides the needed equilibrium populations for the Langevin equation. Second, because the perturbation is small in the optimal reference frame, a second order perturbative expansion of the memory kernel in powers of the diabatic coupling becomes extremely reliable. We test this method for a simple ET reaction modeled by a spin-boson Hamiltonian with Debye spectral density. By comparing of our results to numerically exact simulations[95], we find in most cases the Langevin equation expanded to second order gives accurate results even when the perturbation is fairly large. At short time, the second order expansion ensures an accurate description and, at long time, the populations reach the prescribed equilibrium at a well-defined rate. To apply the Langevin equation, one only needs to compute a time correlation function of the diabatic coupling, which makes the method feasible in *ab initio* molecular dynamics.

The article is organized as follows: In section II, a simple derivation of the Langevin equation and the memory kernels is presented and the optimization of the frame is described as well. In section III, results from benchmark calculations are compared with numerically exact results and the strengths and weaknesses of the method are evaluated. Comparisons of the present approach to similar existing quantum master equations are made in the section IV. Future work and a brief summary are provided in section V.

3.2 The Langevin equation and the optimal reference frame

3.2.1 The optimal reference frame

For a two-state ET model, the total Hamiltonian can be written as:

$$\hat{H} = \begin{pmatrix} \hat{h}_1(\mathbf{p},\mathbf{q}) & \hat{V}(\mathbf{q}) \\ \hat{V}(\mathbf{q}) & \hat{h}_2(\mathbf{p},\mathbf{q}) \end{pmatrix}, \tag{3.1}$$

where $\hat{h}_1$ and $\hat{h}_2$ are the diabatic Hamiltonians on state $|1\rangle$ and $|2\rangle$ respectively, $\hat{V}$ is the diabatic coupling matrix element and $\mathbf{q}$ and $\mathbf{p}$ are the nuclear position and momentum, respectively. The equilibrium density matrix of the system at an inverse temperature β is $\hat{\rho}_{eq} = \frac{1}{\mathrm{tr}_A e^{-\beta\hat{H}}} e^{-\beta\hat{H}}$. Of course, the exponentiation can not be done analytically and to begin with we introduce a perturbative description for the equilibrium state. If one simply expands the Hamiltonian in the interstate coupling $\hat{V}$, the equilibrium density matrix can be written as:

$$\hat{\rho}^{eq} = \frac{1}{\mathrm{tr}_N e^{-\beta\hat{h}_1} + \mathrm{tr}_N e^{-\beta\hat{h}_2}} \begin{pmatrix} e^{-\beta\hat{h}_1} & 0 \\ 0 & e^{-\beta\hat{h}_2} \end{pmatrix} + \mathcal{O}(\hat{V}). \tag{3.2}$$

Truncations at low orders in Eq. 3.2 are typically only valid when the perturbation $\hat{V}$ is small compared to the energy gap between the two electronic states. It is therefore advantageous to transform the Hamiltonian so that the equilibrium density is as accurate as possible. In

this article we choose to transform $\hat{H}$ by rotating the electronic degrees of freedom:

$$\begin{aligned}
\hat{\tilde{H}} &= \begin{pmatrix} \cos\theta & \sin\theta \\ -\sin\theta & \cos\theta \end{pmatrix} \hat{H} \begin{pmatrix} \cos\theta & -\sin\theta \\ \sin\theta & \cos\theta \end{pmatrix} \\
&= \begin{pmatrix} \hat{h}_{av} + \hat{C}(\mathbf{q})\frac{\cos 2\theta}{2} + \hat{V}(\mathbf{q})\sin 2\theta & -\hat{C}(\mathbf{q})\frac{\sin 2\theta}{2} + \hat{V}(\mathbf{q})\cos 2\theta \\ -\hat{C}(\mathbf{q})\frac{\sin 2\theta}{2} + \hat{V}(\mathbf{q})\cos 2\theta & \hat{h}_{av} - \hat{C}(\mathbf{q})\frac{\cos 2\theta}{2} - \hat{V}(\mathbf{q})\sin 2\theta \end{pmatrix} \\
&= \begin{pmatrix} \hat{\tilde{h}}_1 & 0 \\ 0 & \hat{\tilde{h}}_2 \end{pmatrix} + \begin{pmatrix} 0 & \hat{\tilde{V}}(\mathbf{q}) \\ \hat{\tilde{V}}(\mathbf{q}) & 0 \end{pmatrix} \\
&= \hat{\tilde{H}}_0 + \hat{\tilde{V}}(\mathbf{q})\sigma_x
\end{aligned} \tag{3.3}$$

where $\hat{h}_{av} = \frac{1}{2}(\hat{h}_1 + \hat{h}_2)$ and $\hat{C}(\mathbf{q}) = \frac{1}{2}(\hat{h}_1 - \hat{h}_2)$. Since the transformation is unitary, the exact results remain invariant under this rotation. However, a truncated perturbation series will behave differently upon different transformations. Roughly speaking, one should expect better results if the transformation decreases the magnitude of the perturbation. By minimizing the Gibbs-Bogoliubov free energy[96, 93], the optimal rotation can be selected without explicit knowledge of the true equilibrium density. Choosing $\hat{\tilde{V}}$ as the new perturbation, the Gibbs-Bogoliubov inequality is:

$$A \leq A_B(\theta) = -\frac{1}{\beta} \ln \mathrm{tr} e^{-\beta \hat{\tilde{H}}_0} + \langle \hat{\tilde{V}} \hat{\sigma}_x \rangle_0, \tag{3.4}$$

where the thermal average of the perturbation is over the equilibrium distribution of the reference Hamiltonian $\hat{\tilde{H}}_0$. The second term on the right hand side of Eq. 3.4 vanishes so that the Gibbs-Bogoliubov free energy for this particular system becomes:

$$A_B(\theta) = -\frac{1}{\beta} \ln[\mathrm{tr}_N(e^{-\beta \hat{\tilde{h}}_1} + e^{-\beta \hat{\tilde{h}}_2})]. \tag{3.5}$$

Minimizing A_B by varying θ provides a more reliable approximation of the equilibrium density matrix at zeroth order:

$$\hat{\rho}^{eq} \approx \frac{1}{\mathrm{tr}_N(e^{-\beta\hat{\bar{h}}_1} + e^{-\beta\hat{\bar{h}}_2})} \begin{pmatrix} e^{-\beta\hat{\bar{h}}_1} & 0 \\ 0 & e^{-\beta\hat{\bar{h}}_2} \end{pmatrix}, \tag{3.6}$$

which is valid as long as $\hat{\bar{V}}$ is small. The equilibrium populations at zeroth order are:

$$\begin{aligned} P_1^{eq} &\approx \frac{\mathrm{tr}_N e^{-\beta\hat{\bar{h}}_1}}{\mathrm{tr}_N e^{-\beta\hat{\bar{h}}_1} + \mathrm{tr}_N e^{-\beta\hat{\bar{h}}_2}} \\ P_2^{eq} &\approx \frac{\mathrm{tr}_N e^{-\beta\hat{\bar{h}}_2}}{\mathrm{tr}_N e^{-\beta\hat{\bar{h}}_1} + \mathrm{tr}_N e^{-\beta\hat{\bar{h}}_2}} \end{aligned} \tag{3.7}$$

and to the lowest order in $\hat{\bar{V}}$ any non-equilibrium initial state should relax to these values at long time. We note that physically the rotated electronic states also correspond to diabatic states, because the rotation parameters are *fixed* (i.e. they do not depend on the nuclear operators $\mathbf{p}$ and $\mathbf{q}$). The new diabatic states do not correspond to the original diabatic ET states $|1\rangle$ and $|2\rangle$, but are rather to some linear combinations of the original diabatic basis states. Thus, the plan of attack here is to transform from the ET diabatic states into the optimal diabatic basis (where the perturbative approach is expected to work best), run the dynamics to obtain the observables of interest and then transform back to the original basis to analyze the results.

The advantages of using the variationally optimized frame are two-fold. First we have a reliable description for the equilibrium state of the system to which the initial non-equilibrium state should relax. Second, some of the coherent motion in the ET basis is transformed to incoherent population decay in the optimal frame such that an incoherent picture - such as Fermi's Golden Rule - might be more accurate in the rotated basis than in the raw ET basis. We note that the idea of optimizing the Hamiltonian for *thermodynamics* and then using the resulting model for the *dynamics* has been used quite frequently in the literature For

example, Harris and Silbey [91, 92, 93] have used this principle to define an optimal polaron reference to define an "optimal" Bloch-Redfield equation. In this article, we shall thoroughly test this ansatz against numerically exact results in several different parameter regimes.

3.2.2 The Langevin equation

The Hamiltonian for a two-state electron transfer system can be written as:

$$\hat{H} = \begin{pmatrix} \hat{h}_1(\mathbf{p},\mathbf{q}) & \hat{V}(\mathbf{q}) \\ \hat{V}(\mathbf{q}) & \hat{h}_2(\mathbf{p},\mathbf{q}) \end{pmatrix} \tag{3.8}$$

where $\hat{h}_1$ and $\hat{h}_2$ are the diabatic Hamiltonians on state $|1\rangle$ and $|2\rangle$, respectively. $\hat{V}$ is the diabatic coupling matrix element, and $\mathbf{q}$ and $\mathbf{p}$ are the nuclear position and momentum. The observable that we are interested in is the time-dependent population fluctuation on state $|1\rangle$:

$$\delta P_1(t) = P_1(t) - P_1^{eq} = \frac{\mathrm{tr}[\hat{\rho}_0 e^{i\hat{H}t}\delta\hat{P}_1 e^{-i\hat{H}t}]}{\mathrm{tr}\hat{\rho}_0} \tag{3.9}$$

where ρ_0 is the initial density matrix, the population fluctuation operator is $\delta\hat{P}_1 = |1\rangle\langle 1| - P_1^{eq}$, $P_1(t)$ is the time dependent population and P_1^{eq} is the equilibrium population on state $|1\rangle$.

In order to derive the two-hop Langevin equation, we first define a projection operator $\mathbf{P}$[33, 28, 34] as:

$$\mathbf{P}B = \frac{(\hat{B},\delta\hat{P}_1)}{(\delta\hat{P}_1,\delta\hat{P}_1)}\delta\hat{P}_1. \tag{3.10}$$

The inner product in the above equation is defined as an average of the operator product over the initial density matrix:

$$(\hat{A},\hat{B}) = \frac{\mathrm{tr}\hat{\rho}_0\hat{A}\hat{B}}{\mathrm{tr}\hat{\rho}_0}. \tag{3.11}$$

With the projection operator defined, one can write down the generalized Langevin equation

using the Mori's method[34]:

$$\delta\dot{\hat{P}}_1(t) = -\int_0^t K(s)\delta\hat{P}_1(t-s)ds + \hat{F}(t) \tag{3.12}$$

where $K(s)$ is the memory kernel and $\hat{F}(t)$ is the generalized noise operator. The noise operator take the form:

$$\begin{aligned} \hat{F}(t) &= e^{t(1-\mathbf{P})\mathbf{L}}(1-\mathbf{P})\mathbf{L}\delta\hat{P}_1 \\ &= (1-\mathbf{P})\mathbf{L}\sum_{n=0}^{\infty}\frac{[(1-\mathbf{P})\mathbf{L}]^n}{n!}\delta\hat{P}_1 \end{aligned} \tag{3.13}$$

where $\mathbf{L}$ is the Liouville operator such that $\mathbf{L}\hat{A} = i[\hat{H}, \hat{A}]$ for any operator $\hat{A}$ in the Hilbert space. Because of the complementary operator $(1-\mathbf{P})$ in equation 3.13, the noise operator is orthogonal to $\delta\hat{P}_1$as it describes the dynamics outside the relevant space defined by the projection operator $\mathbf{P}$. Therefore, by multiplying equation 3.12 with the operator $\delta\hat{P}_1$ and averaging over ρ_0, the noise term disappears[28] and we are left with:

$$\dot{C}(t) = -\int_0^t K(s)C(t-s)ds \tag{3.14}$$

where $C(t)$ is the autocorrelation function of the operator $\delta\hat{P}_1$:

$$C(t) = (\delta\hat{P}_1(t), \delta\hat{P}_1). \tag{3.15}$$

In general, the autocorrelation function is not exactly the time-dependent population fluctuation that we are interested in, however, if we restrict the initial density to be entirely on state $|1\rangle$, the autocorrelation function becomes directly proportional to $(\delta\hat{P}_1(t))$. To be precise, we require ρ_0 to be $e^{-\beta h_N}|1\rangle\langle 1|$ where $e^{-\beta h_N}$ is any nuclear distribution and h_N is

not necessarily h_1. Then, equation 3.15 becomes:

$$\begin{aligned} C(t) &= (\delta\hat{P}_1(t), \delta\hat{P}_1) \\ &= \frac{\mathrm{tr}\rho_0 \delta\hat{P}_1(t)\delta\hat{P}_1}{\mathrm{tr}\rho_0} \\ &= \frac{\mathrm{tr}\delta\hat{P}_1\rho_0\delta\hat{P}_1(t)}{\mathrm{tr}\rho_0} \\ &= \frac{\mathrm{tr}(|1\rangle\langle 1| - P_1^{eq})(e^{-\beta h_N}|1\rangle\langle 1|)\delta\hat{P}_1(t)}{\mathrm{tr}\rho_0} \\ &= (1 - P_1^{eq})(\delta\hat{P}_1(t)) \end{aligned} \tag{3.16}$$

Hence we can rewrite equation 3.14 as:

$$\delta\dot{P}_1(t) = -\int_0^t K(s)\delta P_1(t-s)ds. \tag{3.17}$$

Equation 3.17 shows the population fluctuation obeys autoregression without noise. The linear convolution relation is essentially a specialized version of the more general Langevin equation, which would also possess a noise term [97]:

$$\dot{A}(t) = -\int_0^t K'(t-s)A(s)ds + f(t). \tag{3.18}$$

In our derivation, the noise term vanishes by design because the noise term is always orthogonal to the subspace spanned by the observable.

3.2.3 A perturbative treatment of the Langevin equation

In order to use Eq. 3.17, one must have knowledge of both the equilibrium population and the memory kernel. The exact evaluations of these two quantities are difficult and approximations must be made. An approximation to the equilibrium density matrix has already been made using a perturbative method (Eq. 3.6). In this section, we employ a similar perturbative treatment to derive an approximate memory kernel $K(t)$.

Using standard time-dependent perturbation theory, the time dependent population fluctuation $\delta P_1(t)$ can be expanded as a power series in the diabatic coupling $\hat{\hat{V}}$:

$$\delta P_1(t) = P_1(t) - P_1^{eq} = \delta P_1^{(0)}(t) + \delta P_1^{(2)}(t) + \cdots \tag{3.19}$$

where

$$\begin{aligned} \delta P_1^{(0)}(t) &= P_1 - P_1^{eq(0)} && (3.20) \\ \delta P_1^{(2)}(t) &= -P_1^{eq(2)} - 2\mathrm{Re}\int_0^t d\tau \int_0^\tau ds \langle e^{i\hat{\hat{h}}_1 \tau} \hat{\hat{V}} e^{-i\hat{\hat{h}}_2(\tau - s)} \hat{\hat{V}} e^{-i\hat{\hat{h}}_1 s} \rangle && (3.21) \\ \cdots &= \cdots \end{aligned}$$

and the first order term vanishes due to the nature of the perturbation. The symbol $P_1^{eq(k)}$ is the equilibrium population to k^{th} order in $\hat{\hat{V}}$. To be consistent with Eq. 3.6 we will neglect $P_1^{eq(k)}$ with $k \geq 2$ in what follows. The second order term $\delta P_1^{(2)}(t)$ describes a coherent two-hop process in which the electron hops from $|\bar{1}\rangle$ to $|\bar{2}\rangle$ at time s and then hops back to $|\bar{1}\rangle$ at time t. The intermediate hopping time s is then averaged over to obtain the second order correction. Higher order terms can be similarly derived and they represent coherent four-, six-, eight-... hopping processes.

The memory kernel can also be expanded in power series of $\hat{\hat{V}}$:

$$K(t) = K^{(0)}(t) + K^{(2)}(t) + \cdots \tag{3.22}$$

By substituting these power series into Eq. 3.17 and matching terms with the same power of $\hat{\hat{V}}$, we have:

$$\begin{aligned} 0 &= -\int_0^t K^{(0)}(s) ds \\ \delta \dot{P}_1^{(2)}(t) &= -\int_0^t ds K^{(2)}(t-s) \delta P_1^{(0)} && (3.23) \\ \cdots &= \cdots \end{aligned}$$

Rearranging terms above we find that $K^{(0)}(t) = 0$ and $K_1^{(2)} = \frac{-\delta\ddot{P}_1^{(2)}}{\delta P_1^{(0)}}$. Replacing $K(t)$ by its second order approximation $K^{(2)}(t)$ in Eq. 3.17 results in a two-hop Langevin equation:

$$\delta\dot{P}_1(t) = -\int_0^t ds K^{(2)}(t-s)\delta P_1(s). \tag{3.24}$$

Equation 3.24 is a cumulant-like approximation for the population fluctuation. If one again expands Eq. 3.24 in powers of $\hat{\hat{V}}$, the results are:

$$\delta\dot{P}_1^{(2n+2)} = -\int_0^t ds K^{(2)}(t-s)\delta P_1^{(2n)}(s), \tag{3.25}$$

Thus, populations higher than second order in $\hat{\hat{V}}$ are approximated by the convolution of the lower order population with the two-hop kernel. To put it another way, all correlated hopping processes higher than second order in $\hat{\hat{V}}$ are neglected. Therefore, even if the perturbation, $\hat{\hat{V}}$, is not small, one might expect the two-hop approximation to be valid if the populations relax to their equilibrium values faster than these multiple-hop processes can occur. Thus, high frequency nuclear motions and a large separation in the equilibrium locations of the different electronic states are likely to enhance the range of validity of Eq. 3.24.

At long time, the Markovian version of Eq. 3.24 is:

$$\delta\dot{P}_1(t) = -\tilde{K}^{(2)}\delta P_1(t) \tag{3.26}$$

where $\tilde{K}^{(2)} = \int_0^\infty K^{(2)}(t)dt$ and the solution is:

$$P(t) = \delta P_1(0)\ e^{-\tilde{K}^{(2)}t} + P_1^{eq}. \tag{3.27}$$

Thus, the system decays toward equilibrium at a well-defined rate $\tilde{K}^2$.

Eq. 3.24 is the primary result of this article. It describes the non-Markovian relaxation of the population toward equilibrium. Approximating the memory kernel by its second order

expansion results in a two-hop Langevin equation(THLE), where repeated applications of the two-hop event dictate the population dynamics. The population obtained from the THLE is accurate at short time(the initial population decay) since only the two-hop process is relevant. At long time, the population will relax to a prescribed equilibrium value(P_1^{eq}) according to Eq. 3.27. The second order kernel in Eq. 3.24 has a well defined semiclassical correspondence and could be computed using *ab initio* molecular dynamics, which makes this an appealing technique for on-the-fly simulations.

3.2.4 Self-consistent hybrid approach

To obtain numerically exact results for the spin-boson model we use the self-consistent hybrid (SCH) method[94, 95]. The basic idea of the SCH method is to introduce an iterative convergence procedure in a dynamical hybrid approach. Thereby the overall system is first partitioned into a *core* and a *reservoir*, based on any convenient but otherwise rather arbitrary initial guess. A dynamical hybrid calculation is then carried out, with the core treated via a numerically exact quantum mechanical method and the reservoir treated via a more approximate method. The key concept of the SCH is its second step: the optimization of the core-reservoir partition. Thereby, the size of the core, as well as other variational parameters, is systematically increased in repeated hybrid calculations to achieve numerical convergence. This makes the method variational in nature and leads to convergence to the true quantum results.

The method we choose to treat the core is the multilayer multi-configuration time-dependent Hartree (MCTDH) theory[98] which allows one to treat a rather large system quantum mechanically. Various approximate methods can be used to treat the reservoir, e.g., classical mechanics, semiclassical initial value representations, or quantum perturbation theories. In the applications discussed in this paper we use classical mechanics to treat the reservoir, except at low temperatures, where it was advantageous to treat the highest frequency motions via perturbation theory.

3.3 Results

In order to test the modified second order Langevin equation, we perform benchmark calculations using the simple spin-boson model with Debye spectral density, where numerically exact results have been obtained previously[95]. The Hamiltonian used is:

$$\hat{H} = \hat{H}_S + \hat{H}_{SB} + \hat{H}_B, \tag{3.28}$$

where the bath Hamiltonian is $\hat{H}_B = \frac{1}{2}\sum_j(\hat{p}_j^2 + \omega_j^2\hat{x}_j^2)$, the system Hamiltonian is $\hat{H}_S = \begin{pmatrix} \epsilon & \Delta \\ \Delta & -\epsilon \end{pmatrix}$ and the system-bath coupling is $\sigma_z\sum_j c_j\hat{x}_j$. The spectral density of the bath is in the Debye form:

$$J(\omega) = \frac{\pi}{2}\sum_j \frac{c_j^2}{\omega_j}\delta(\omega - \omega_j) \tag{3.29}$$

and

$$J(\omega) = \frac{\eta\omega_c\omega}{\omega_c^2 + \omega^2}. \tag{3.30}$$

The coupling strength η is related to the reorganization energy in the ET theory[99] through $\lambda = 2\sum_j \frac{c_j^2}{\omega_j^2} = 2\eta$ and the critical frequency ω_c is inversely proportional to the longitudinal relaxation time of the solvent[100]. The system is completely specified by the set of parameters β, ω_c, ϵ, Δ and η. Following reference[100, 94, 95], we set $\Delta = 1$ and other parameters are measured in units of Δ.

In accord with reference[95], our initial density matrix is

$$\hat{\rho}(0) = \begin{pmatrix} \hat{\rho}_B & 0 \\ 0 & 0 \end{pmatrix} \tag{3.31}$$

where $\hat{\rho}_B$ is the equilibrium distribution of the bare bath. In cases where the Hamiltonian $\hat{H}$ is rotated to $\hat{\tilde{H}}$, we choose the initial conditions to correspond to a completely occupied

upper state in the rotated frame and the initial nuclear density matrix is unaltered. We note that the THLE (Eq. 3.24) is technically only applicable when the nuclei are initially in equilibrium in their respective diabatic states. However, in order to compare with the exact results, we relax the restriction in this particular application. As will be shown shortly, we find no artifacts resulting from this approximate initial state.

The rotated spin-boson Hamiltonian is given below:

$$\hat{\tilde{H}} = \hat{\tilde{H}}_{SB} + \hat{\tilde{H}}_B + \hat{\tilde{H}}_S \tag{3.32}$$

where

$$\begin{aligned}
\hat{\tilde{H}}_S &= \begin{pmatrix} \bar{\epsilon} & \bar{\Delta} \\ \bar{\Delta} & \bar{\epsilon} \end{pmatrix} \\
\hat{\tilde{H}}_B &= \hat{H}_B \\
\hat{\tilde{H}}_{SB} &= \cos 2\theta \hat{\sigma}_z \sum_j c_j \hat{x}_j \\
\bar{\Delta} &= -\sin 2\theta \sum_j c_j \hat{x}_i + (\Delta \cos 2\theta - \epsilon \sin 2\theta) \\
\bar{\epsilon} &= \epsilon \cos 2\theta + \Delta \sin 2\theta
\end{aligned} \tag{3.33}$$

and, treating $\bar{\Delta}$ as the perturbation, the Gibbs-Bogoliubov free energy bound is:

$$A_B(\theta) = -\frac{1}{\beta} \ln(\cosh \beta\bar{\epsilon}) - \frac{\eta}{2} \cos^2 2\theta. \tag{3.34}$$

When η is large, the second term in Eq. 3.34 dominates and suggests $\theta = 0$ corresponds to the optimal frame. This is consistent with the well known fact that the effects of correlated multiple hopping events are small in a fast dissipating system[91, 31] thus the THLE is a good approximation with $\theta = 0$. When η is small, the optimal frame favors a maximized bias, $\bar{\epsilon}$, which in turn approximately diagonalizes the Hamiltonian.

We compute the average values of $\langle \sigma_z \rangle$ (which measures population decay) and $\langle \sigma_x \rangle$

(which addresses coherence decay) because in certain parameter regimes, the dynamics of $\langle\sigma_z\rangle$ can be accurate but $\langle\sigma_x\rangle$ may be qualitatively wrong[27] and thus a simple presentation of $\langle\sigma_z\rangle$ can sometimes give a misleading picture of the accuracy of the approximation. The computation of $\langle\sigma_x\rangle$ follows what is outlined in reference[31], in which the populations are computed first by Eq. 3.24 and subsequently used in the calculation of $\langle\sigma_x\rangle$

$$\langle\sigma_x(t)\rangle = \mathrm{Im}\int_0^t [A(t,s)P_2(s) - B(t,s)P_1(s)]ds \tag{3.35}$$

where $A(t,s) = \langle e^{i\hat{\hat{h}}_2 t}e^{-i\hat{\hat{h}}_1(t-s)}\hat{\hat{V}}e^{i\hat{\hat{h}}_2 s}\rangle$ and $B(t,s) = \langle e^{i\hat{\hat{h}}_1 t}e^{-i\hat{\hat{h}}_2(t-s)}\hat{\hat{V}}e^{i\hat{\hat{h}}_1 s}\rangle$ and again, the average is over $\hat{\rho}_N(0)$. Eq. 3.35 is obtained by first writing down the exact equation of motion for the coherence

$$\langle\sigma_x(t)\rangle = \mathrm{Im}\int_0^t \mathrm{tr}_N e^{-i\hat{\hat{h}}_1(t-s)}(\hat{\hat{V}}\hat{\rho}_2(s) - \hat{\rho}_1(s)\hat{\hat{V}})e^{i\hat{\hat{h}}_2(t-s)}ds \tag{3.36}$$

and approximating the diagonal density matrix by

$$\begin{aligned}\hat{\rho}_1(t) &= P_1(t)e^{-i\hat{\hat{h}}_1 t}\hat{\rho}_N(0)e^{i\hat{\hat{h}}_1 t} \\ \hat{\rho}_2(t) &= P_2(t)e^{-i\hat{\hat{h}}_2 t}\hat{\rho}_N(0)e^{i\hat{\hat{h}}_2 t}.\end{aligned} \tag{3.37}$$

The kernels $A(t,s)$ and $B(t,s)$ represent the amplitude of going from one state to another in a one-hop process. Hence, Eq. 3.35, is also a cumulant-like approximation for the coherence, like the THLE. Since Eq. 3.36 is already first order in $\hat{\hat{V}}$, Eq. 3.35 is correct through first order in $\hat{\hat{V}}$ and higher orders are approximated by repeated two-hop processes that are drawn in via P_1 and P_2. Thus the expected range of validity of Eq. 3.35 is similar to that of the THLE, although it is founded on the somewhat different formal approximations.

In order to apply the THLE, one must compute the second order correlation function that appears in $\dot{P}_1^{(2)}$. Although this correlation function will need to be computed on-the-fly

in general, for the Spin-Boson problem it can be computed analytically:

$$\begin{aligned}
\dot{P}_1^{(2)} &= -2\mathrm{Re}\int_0^t \mathrm{tr}_N \hat{\rho}_B e^{i\hat{\tilde{h}}_1 t}\hat{\tilde{V}}e^{-i\hat{\tilde{h}}_2(t-s)}\hat{\tilde{V}}e^{-i\hat{\tilde{h}}_2 t} \\
&= -2\mathrm{Re}\int_0^t ds e^{\cos^2 2\theta\{-Q(t-s)+i[Q'(t)-Q'(t-s)-Q'(s)]\}+2i\bar{\epsilon}(t-s)} \\
&\quad \{(\bar{\Delta}+i\frac{\sin 4\theta}{4}[-P(t-s)+iP'(t)-iP'(t-s)]) \\
&\quad (\bar{\Delta}-i\frac{\sin 4\theta}{4}[P(t-s)-iP'(s)+iP'(t-s)])+\frac{\sin^2 2\theta}{4}[R(t-s)-iR'(t-s)]\}
\end{aligned} \tag{3.38}$$

where the bath correlations functions are:

$$\begin{aligned}
Q(t)+iQ'(t) &= \frac{4}{\pi}\int_0^\infty d\omega \frac{J(\omega)}{\omega^2}[\coth\frac{\beta\omega}{2}(1-\cos\omega t)+i\sin\omega t] \\
P(t)+iP'(t) &= \frac{4}{\pi}\int_0^\infty \frac{J(\omega)}{\omega}[\coth\frac{\beta\omega}{2}\sin\omega t+i\cos\omega t] \\
R(t)+iR'(t) &= \frac{4}{\pi}\int_0^\infty J(\omega)[\coth\frac{\beta\omega}{2}\cos\omega t+i\sin\omega t].
\end{aligned} \tag{3.39}$$

Other important quantities, such as the memory kernel $\tilde{K}^{(2)}(t)$, can all be conveniently expressed in terms of $\dot{P}_1^{(2)}(t)$.

3.3.1 Systems without electronic bias ($\epsilon = 0$)

With $\epsilon = 0$, the Gibbs-Bogoliubov free energy bound is:

$$A_B(\theta) = -\frac{1}{\beta}\ln[\cosh(\beta\Delta\sin 2\theta)]-\frac{\eta}{2}\cos^2 2\theta. \tag{3.40}$$

Eq. 3.40 is nonlinear but it is easy to see that the minimum for the first term(effective driving force) is $\theta = \frac{\pi}{4}$ and its maximum occurs at $\theta = 0$. For the second term(the reorganization energy), $\theta = 0$ is the maximum and $\theta = \frac{\pi}{4}$ is the minimum. Therefore, when one of the two terms dominates over another, the minimum of $A_B(\theta)$ can be identified as the minimum of the dominant term. When the reorganization energy is much larger than the effective

driving force, the minimum of $A_B(\theta)$ occurs at $\theta = 0$ and the unrotated frame should be used to carry out the calculation. In this special case, the equilibrium population on each surface is known to be $\frac{1}{2}$ by symmetry. When the reorganization energy is small the optimal basis becomes the "pure dephasing reference system"[36], in which $\theta = \frac{\pi}{4}$. In this reference, the interstate coupling Δ becomes the effective bias $\bar{\epsilon}$ and the system bath coupling $\hat{H}_{SB}$ becomes the interstate coupling $\bar{\Delta}$ in the new frame. The equilibrium populations in the pure dephasing frame are estimated to be $P_1^{eq} = \frac{e^{-\beta\Delta}}{e^{-\beta\Delta}+e^{\beta\Delta}}$ and $P_2^{eq} = \frac{e^{\beta\Delta}}{e^{-\beta\Delta}+e^{\beta\Delta}}$, to the zeroth order of $\hat{H}_{SB}$.

Case I ($\beta\Delta = 0.5$, $\eta = 0.5\Delta$ and $\omega_c = 5\Delta$)

To begin with, we look at a system where the diabatic coupling Δ is small, making the THLE an excellent approximation. Here the critical frequency of the bath, ω_c, is five times the perturbation Δ, resulting in nonadiabatic electron transfer. The reorganization energy is moderate: $E_r = 2\eta = \Delta$. The temperature here is low compared to the critical frequency but moderate compared to the interstate coupling, with the inverse temperature $\beta\Delta = 0.5$. Figure 3.1(a) shows that the evolution of $\sigma_z(t)$ from both the THLE and the exact calculation. As expected, $\sigma_z(t)$ agrees very well with the exact result, which exhibits relatively quick decoherence and the whole course of electron transfer completes in a short time span, due to a fast bath. Figure 3.1(b) displays the evolution of $\sigma_x(t)$ from both calculations. Examination of figure 3.1(b) reveals that the approximation to $\sigma_x(t)$ is also quantitative, despite the fact that Eq. 3.35 is only correct to the first order in Δ.

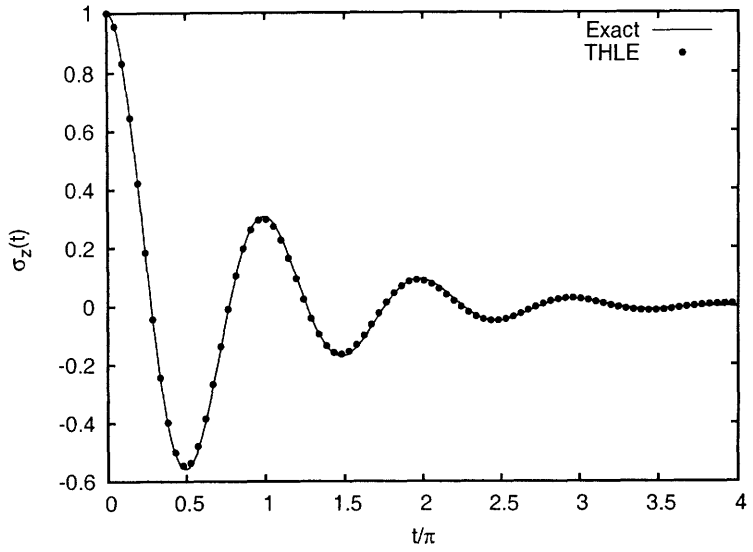

(a)

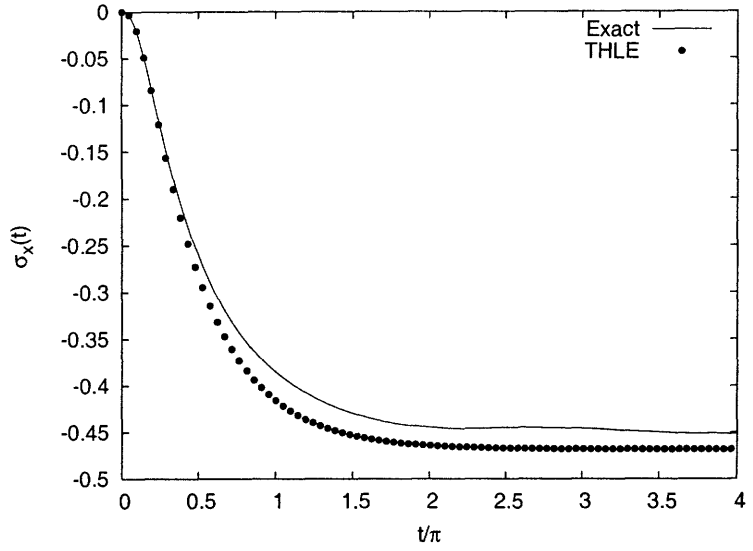

(b)

Figure 3.1: The dynamics of (a) $\sigma_z(t)$ and (b) $\sigma_x(t)$ in the optimal frame($\theta = 0$), for the Spin Boson Case I ($\beta\Delta = 0.5$, $\eta = 0.5\Delta$ and $\omega_c = 5\Delta$).

Case II ($\beta\Delta = 0.5$, $\eta = 0.5\Delta$ **and** $\omega_c = 0.25\Delta$)

As the perturbation increases, the two-hop approximation becomes less accurate. To see this effect, we decrease the critical frequency of the bath from $\omega_c = 5\Delta$ in Case I to $\omega_c = 0.25\Delta$, making the electron transfer adiabatic. The system-bath coupling and the inverse temperature are kept unchanged: $\eta = 0.5\Delta$ and $\beta\Delta = 0.5$. Figure 3.2(a) shows further

oscillations in the exact result are missed by the THLE, which predicts much faster damping. One obvious reason is that the critical frequency ω_c is only a quarter of the perturbation Δ, therefore one would not expect the second order truncation to be sufficient. Another reason, perhaps less obvious, is that the system bath coupling, $\eta = 0.5\Delta$, is only moderate in this case, which also leads to slow damping of quantum oscillations, a longer coherence time, and more coherent multiple-hop events. The approximate $\sigma_x(t)$ (Figure 3.2(b)) is qualitatively correct and it reaches a final value of -0.46 at long time, compared to -0.34 from the exact result.

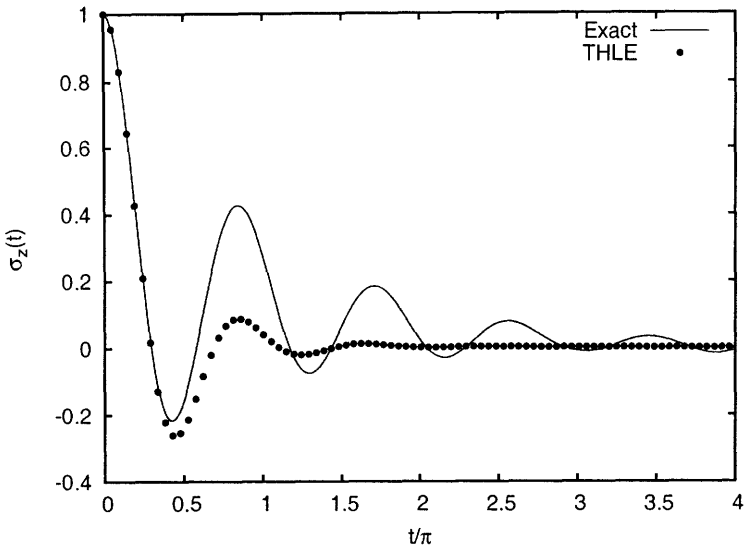

(a)

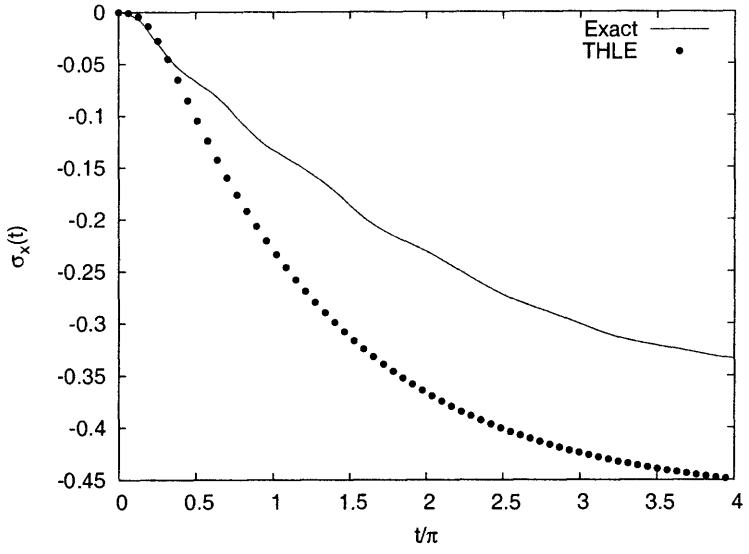

(b)

Figure 3.2: The dynamics of (a) $\sigma_z(t)$ and (b) $\sigma_x(t)$ in the optimal frame($\theta = 0$), for the Spin Boson Case II ($\beta\Delta = 0.5$, $\eta = 0.5\Delta$ and $\omega_c = 0.25\Delta$).

Case III ($\beta\Delta = 5$, $\eta = 0.5\Delta$ and $\omega_c = 0.25\Delta$)

Case II is a pathological case for the THLE, and one might expect even worse results if the temperature or the system bath coupling is lowered, since both lead to slower damping. However, if these parameters are lowered by much the minimum of the free energy will move to $\theta = \frac{\pi}{4}$, making η the new perturbation and Δ an energy bias. This system actually

favors fast damping and the THLE is well suited to the dynamics of such an ET reaction. To demonstrate, we increase the inverse temperature β in Case II to $\beta\Delta = 5$, a ten fold decrease in temperature. We also run calculations in both the un-optimal($\theta = 0$) and the optimal($\theta = \frac{\pi}{4}$) frame, allowing one to see the importance of using the optimal frame. For clarity, we will refer to the THLE in the optimal frame simply as the Langevin equation (LE). Figure 3.3(a) shows the evolution of $\sigma_z(t)$ in the un-optimal frame with the LE. The exact result shows more persistent oscillations and a longer time for electron transfer completion compared to what is seen in Case II. The approximate $\sigma_z(t)$, agrees quite well with the exact result. But figure 3.3(b) shows the evolution of $\sigma_x(t)$ in the same frame soon becomes less than -1. Clearly, coherence above one in magnitude must be considered a serious error. This is a well known problem for similar perturbative methods, such as the non-interacting blip approximation at low temperature, where $\sigma_z(t)$ is guaranteed to go to zero at long time but $\sigma_x(t)$ can even diverge [27]. Fortunately, the optimal frame comes to the rescue. In the optimal frame $\theta = \frac{\pi}{4}$, which effectively switches the roles of σ_x and σ_z: what once was a coherence is now a population and vice versa. This has a profound effect on the dynamics as well as the initial conditions. For consistency, we will always show the evolution of $\sigma_x(t)$ and $\sigma_z(t)$ in the *unrotated* frame, regardless of the frame in which the simulations are performed. In general, the rotated results ($\tilde{\sigma}_x(t)$, $\tilde{\sigma}_z(t)$) can be obtained easily from a linear combination of $\sigma_x(t)$ and $\sigma_z(t)$. In the present case, the extreme value $\theta = \frac{\pi}{4}$ means that the initial value of σ_z is actually *zero* - our initial state is a coherence in the original diabatic basis. Further, $\sigma_z(t)$ from the THLE stays essentially at zero for all time ($< 10^{-16}$, and therefore not shown) and it agrees very well with the exact $\sigma_z(t)$ in the same frame, which is zero within the numerical errors ($< 10^{-3}$). Thus, the population remains evenly distributed between left and right for all times. On the other hand, as seen in figure 3.4, the exact $\sigma_x(t)$ now displays incoherent relaxation. Also, the long time limit of $\sigma_x(t)$ is close to -1, as it should be, instead of -2.5 as it was in the un-optimal frame. Note that the predicted equilibrium is not exact, but this should be expected. The quality of $\sigma_x(t)$ from

the THLE is vastly improved compared to what is seen in figure 3.3(b) for $\sigma_x(t)$, illustrating the benefits of the optimal frame in this case.

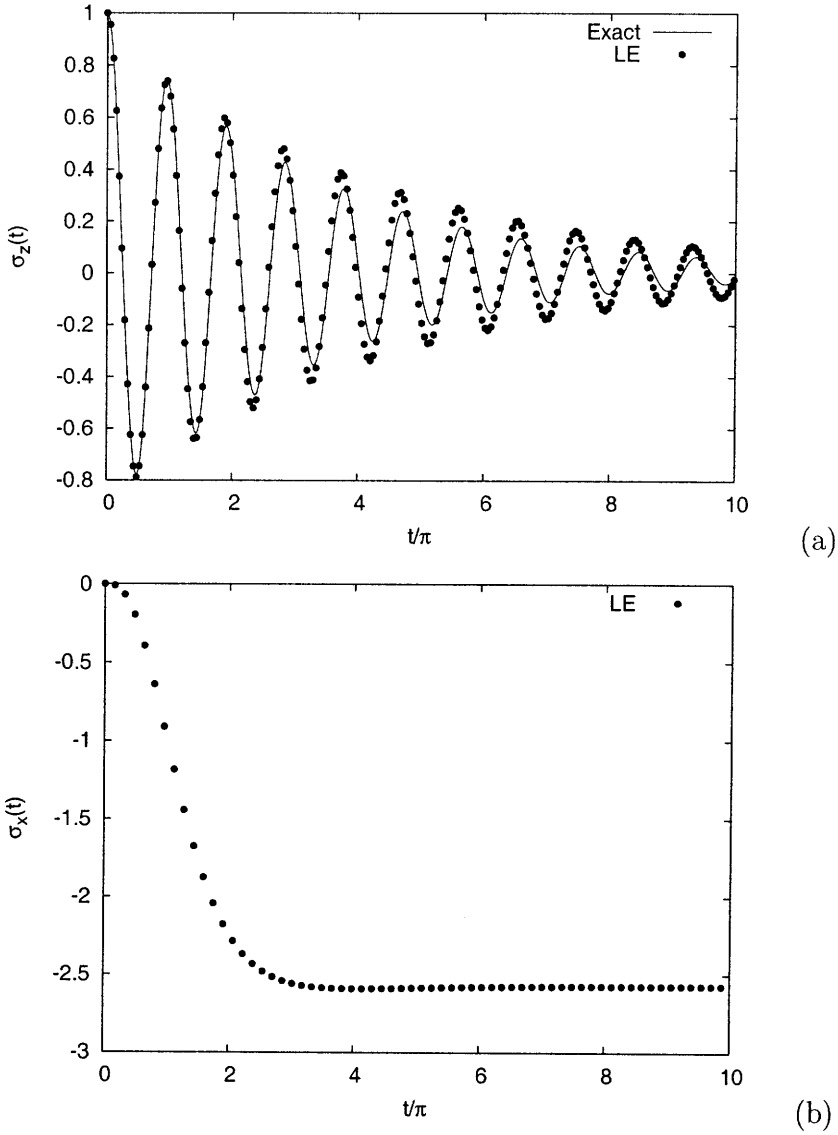

Figure 3.3: The dynamics of $\sigma_z(t)$ in the un-optimal frame($\theta = 0$), for the Spin Boson Case III ($\beta\Delta = 5$, $\eta = 0.5\Delta$ and $\omega_c = 0.25\Delta$).

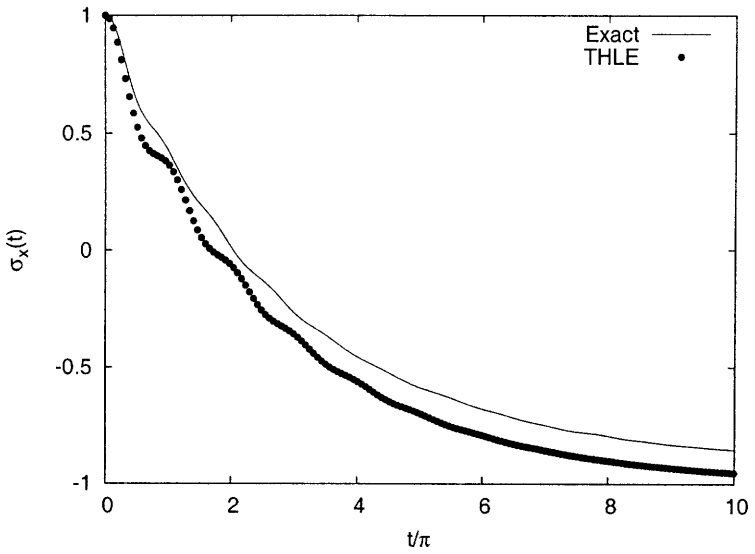

Figure 3.4: The dynamics of $\sigma_x(t)$ in the optimal frame($\theta = \frac{\pi}{4}$), for the Spin Boson Case III($\beta\Delta = 5$, $\eta = 0.5\Delta$ and $\omega_c = 0.25\Delta$).

Case IV ($\beta\Delta = 0.5$, $\eta = 5\Delta$ and $\omega_c = \Delta$)

So far we have observed the performance of the THLE in systems where the perturbation is either very small($\omega_c = 5\Delta$) or very large($\omega_c = 0.25\Delta$). In order to explore the range of applicability of the THLE we now look at an intermediate regime, where ω_c is comparable to the perturbation Δ. We set the critical frequency equal to the perturbation in magnitude: $\omega_c = \Delta$ with the other parameters: $\eta = 5\Delta$ and $\beta\Delta = 1$. Figure 3.5 shows very good agreement is achieved between the THLE and the exact result. Here $\sigma_z(t)$ initially decreases quickly to half of its initial value but eventually reaches a long tail of exponential decay at a smaller rate. Due to the relatively large system bath coupling $\eta = 5$, there are no visible oscillations in population. The large system bath coupling strongly contributes to the accuracy of the approximate result since coherent multiple-hop events are suppressed by the large dephasing effects even at the presence of a moderately strong perturbation. It is interesting to note that in reference[95], the non-interacting blip approximation[26] fails to describe the long time relaxation of $\sigma_z(t)$ correctly for this case. This is possibly due to the fact that all incoherent hops are included in the current approximation but not in the

non-interacting blip approximation[27].

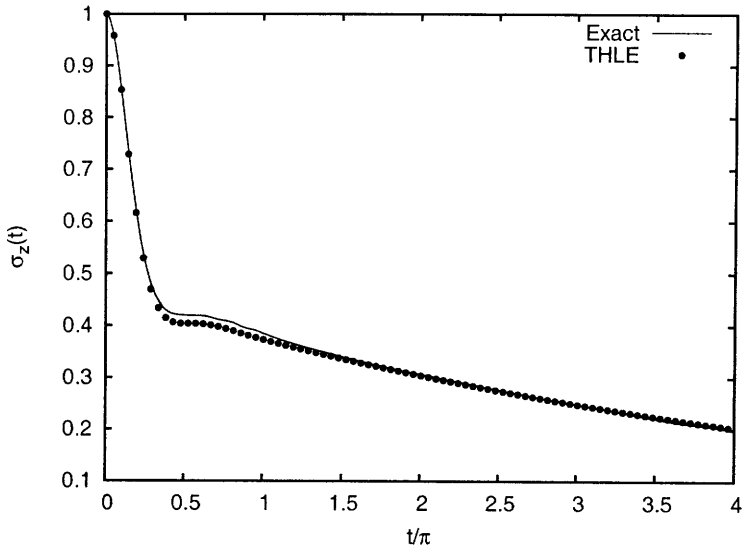

Figure 3.5: The dynamics of $\sigma_z(t)$ in the optimal frame($\theta = 0$), for the Spin Boson Case IV ($\beta\Delta = 1$, $\eta = 5\Delta$ and $\omega_c = 1\Delta$)

3.3.2 Systems with electronic bias ($\epsilon \neq 0$)

Systems with bias are fundamentally different from their unbiased counterparts in many aspects. As observed in reference [95], most approximate methods give worse predictions in the presence of a bias. Furthermore, in the unbiased cases, it is clear the long time limit of $\sigma_z(t)$ must be zero, for $\theta = 0$. But with a bias, the limit of $\sigma_z(t)$ is not known in closed form and different approximations in general will predict different long time values. Finally, from Eq. 3.34, we can no longer tell that the minimum of the free energy bound is at either $\theta = 0$ or $\theta = \frac{\pi}{4}$. The precise location of the minimum now depends on the particular parameters and has to be found numerically.

Case V ($\beta\Delta = 0.5$, $\eta = 0.5\Delta$, $\omega_c = 5\Delta$ and $\epsilon = \Delta$)

Again we start with a system where the diabatic coupling Δ is small. All parameters are the same as in case I but now we set $\epsilon = 1$. As Figure 3.6(a) shows, in the un-optimal

frame($\theta = 0$), the exact $\sigma_z(t)$ exhibits moderate decoherence and relaxes to an equilibrium value at -0.39. The LE result shows good agreement for the initial decay but later oscillations deviate slightly from the exact result and it predicts a lower equilibrium value, -0.45. The comparison between the approximate and exact $\sigma_x(t)$'s (Figure 3.6(b)) shows a similar behavior: the approximate $\sigma_x(t)$ is accurate at short time but only qualitatively correct at longer time and reaches a equilibrium value of -0.38, instead of -0.42. Since V is small in this case, one would have perhaps expected better agreement for this situation. These observations illustrate the above-mentioned difficulties in the presence of an electronic bias.

Things look somewhat different in the optimal basis, which in this case corresponds to the angle $\theta = 0.083\pi$. The results of $\sigma_z(t)$ and $\sigma_x(t)$ in the optimal frame are shown in Figure 3.7(a) and 3.7(b), respectively. Note that the rotation of the electronic states changes the initial conditions so that the initial population on the upper surface is somewhat less than unity and there is significant coherence in the initial density matrix. Compared to the results in a frame where $\theta = 0$, improvements are seen in both $\sigma_z(t)$ and $\sigma_x(t)$. In figure 3.7(a), $\sigma_z(t)$ from the THLE remains in phase with the exact result at all times. The long time value of σ_z is also improved: the THLE predicts -0.44, also in fairly good agreement with the exact result, -0.40. The small deviation here is due to errors in our approximate equilibrium density matrix, which results in inexact equilibrium populations. The agreement in σ_x is of similar quality to σ_z. Thus, the optimal frame provides a noticeable, if not breathtaking, improvement in the approximate dynamics.

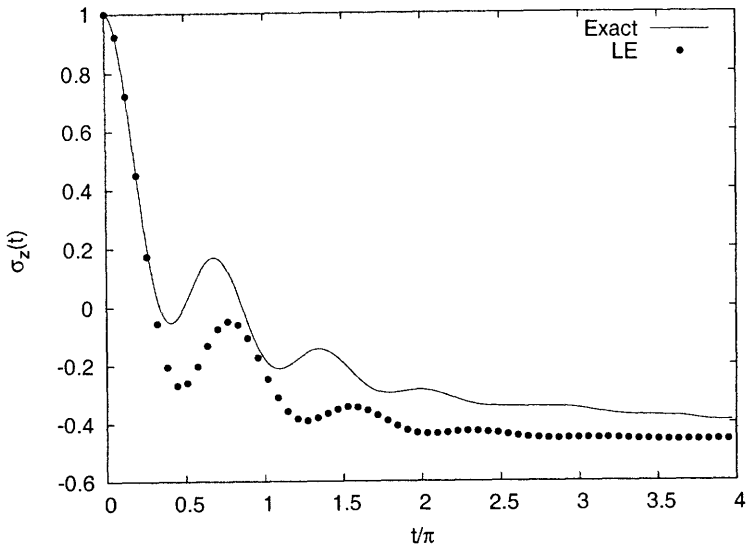

(a)

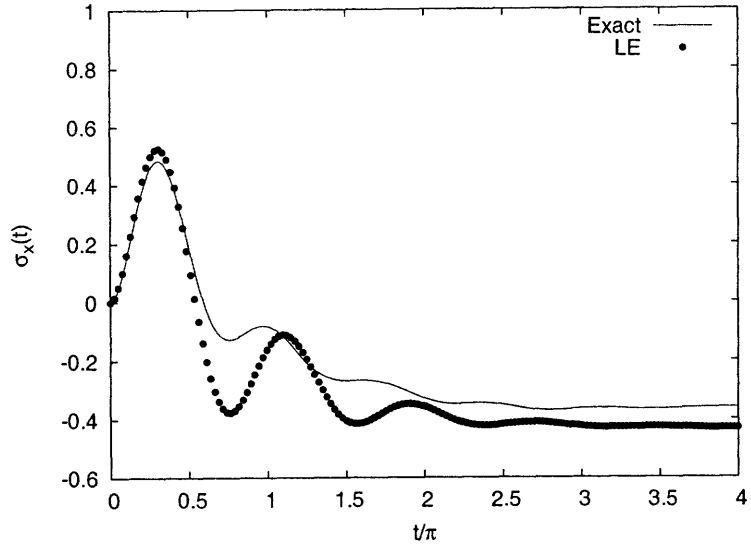

(b)

Figure 3.6: The dynamics of (a) $\sigma_z(t)$ and (b) $\sigma_x(t)$ in the un-optimal frame($\theta = 0.083\pi$), for the Spin-Boson Case V ($\beta\Delta = 0.5$, $\eta = 0.5\Delta$, $\omega_c = 5\Delta$ and $\epsilon = 1\Delta$).

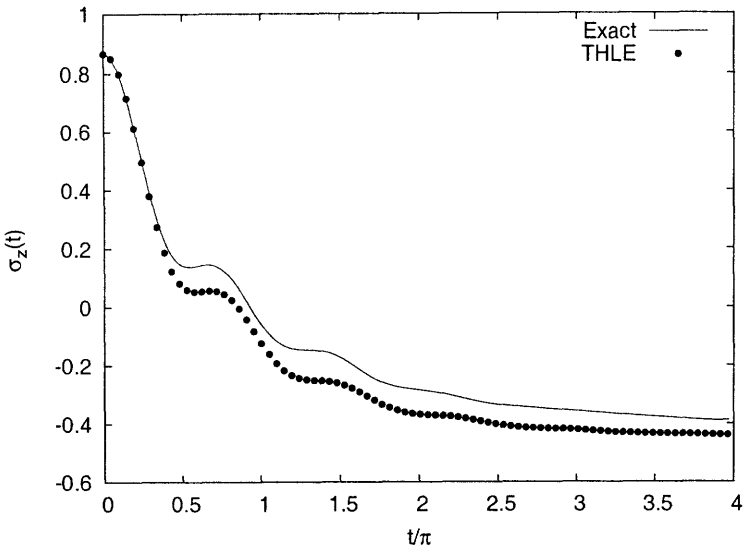

(a)

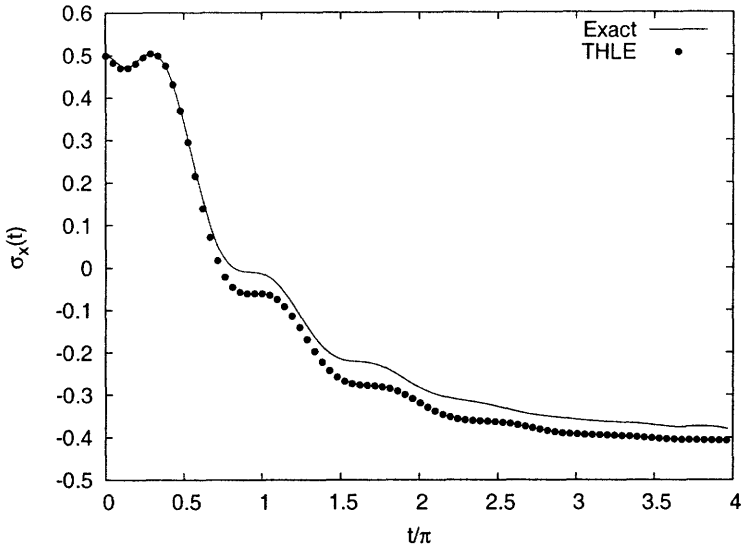

(b)

Figure 3.7: The dynamics of (a) $\sigma_z(t)$ and (b) $\sigma_x(t)$ in the optimal frame($\theta = 0.083\pi$), for the Spin-Boson Case V ($\beta\Delta = 0.5$, $\eta = 0.5\Delta$, $\omega_c = 5\Delta$ and $\epsilon = 1\Delta$).

Case VI ($\beta\Delta = 50$, $\eta = 0.5\Delta$, $\omega_c = 5\Delta$ **and** $\epsilon = \Delta$)

While the differences of using the optimal and un-optimal frames are not drastic at a high temperature such as $\beta\Delta = 0.5$, the situation changes when the system is at very low temperature. We now study the same system at $\beta\Delta = 50$. In order to emphasize the importance the optimal frame, we again perform calculations in both unrotated and optimal frame. Com-

parisons between the two reference frames show that only the optimal frame is physically correct for the THLE in the low temperature limit.

Figure 3.8(a) shows the evolution of $\sigma_z(t)$ for the un-optimal frame $\theta = 0$. The exact $\sigma_z(t)$ decays to -0.729 with continuously damped oscillations throughout the course of population transfer. The LE result, however, shows undamped and out of phase oscillations at longer time and $\sigma_z(t)$ reaches -1, indicating that the system will completely localize in the lower diabatic state at equilibrium. Such prediction is a simple result of Eq. 3.7:

$$\lim_{t\to\infty} \sigma_z(t) = -\tanh(\beta\epsilon). \tag{3.41}$$

On the other hand, in the weak coupling limit[27, 95], the correct long time limit turns out to be

$$\lim_{t\to\infty} \sigma_z(t) = -\frac{\epsilon}{\sqrt{\Delta_{eff}^2 + \epsilon^2}} \tanh(\beta\sqrt{\Delta_{eff}^2 + \epsilon^2}). \tag{3.42}$$

In the weak coupling limit, $\sqrt{\Delta_{eff}^2 + \epsilon^2}$ can be interpreted as the Rabi frequency of an effective two level system and $-\frac{\epsilon}{\sqrt{\Delta_{eff}^2+\epsilon^2}}$ is directly related to the weight of each diabatic state in the effective lower adiabatic state. Eq. 3.42 shows it is the effective lower adiabatic state that will be completely occupied, not the lower diabatic state as predicted by Eq. 3.41. For this parameter setting , the effective Rabi frequency works out to be 1.37Δ and $\lim_{t\to\infty} \sigma_z(t) = -0.729$[95].

The difference between -1 from Eq. 3.41 and -0.729 from Eq. 3.42 is physically significant since the wrong state is occupied in the former case. In figure 3.8(b), we also see that the approximate $\sigma_x(t)$ oscillates wildly without damping while the exact result shows relaxation to -0.65 with very slow damping, similar to the exact $\sigma_z(t)$.

These results suggest that the frame where $\theta = 0$ is not the most appropriate frame for a perturbative treatment. In the optimal frame, where $\theta = 0.098\pi$, the effective bias $\bar{\epsilon}$ becomes 1.39Δ, very close to 1.37Δ, the Rabi frequency of the effective two level system. Thus the new diabatic states can be thought as pseudo-adiabatic states since they resemble

the true adiabatic states near equilibrium. Figure 3.9 shows that the evolution of $\sigma_z(t)$ and $\sigma_x(t)$ in the optimal frame. We first note that the long time value of $\sigma_z(t)$ from the THLE is essentially correct, aside from some small, persistent oscillations. These oscillations are slightly out of phase with the exact result, and are underdamped, but the agreement with the exact results is good. Examination of Figure 3.9(b) once again indicates that $\sigma_x(t)$ from the THLE is of similar accuracy to $\sigma_z(t)$. The clear implication of these results is that the rotation to the optimal electronic frame is *required* if one wishes to control the long-time populations in the THLE. We will return to this point in the discussion.

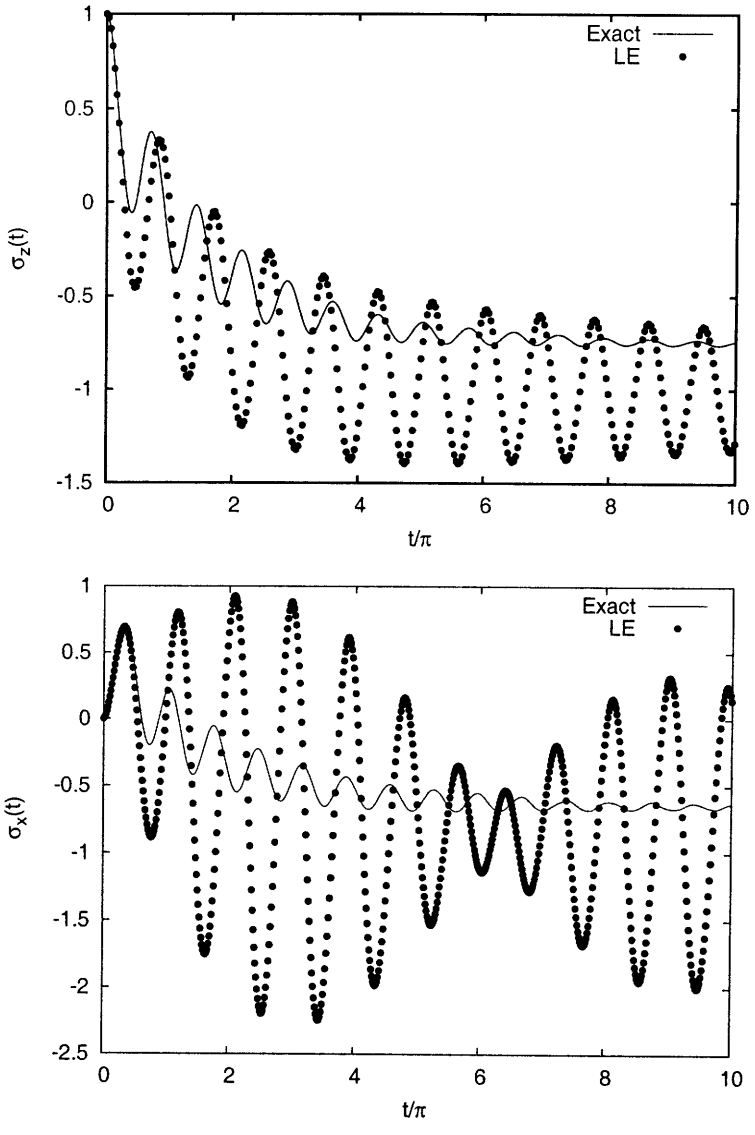

Figure 3.8: The dynamics of (a) $\sigma_z(t)$ and (b) $\sigma_x(t)$ in the un-optimal frame($\theta = 0$), for the Spin Boson Case VI ($\beta\Delta = 50$, $\eta = 0.5\Delta$, $\omega_c = 5\Delta$ and $\epsilon = 1\Delta$).

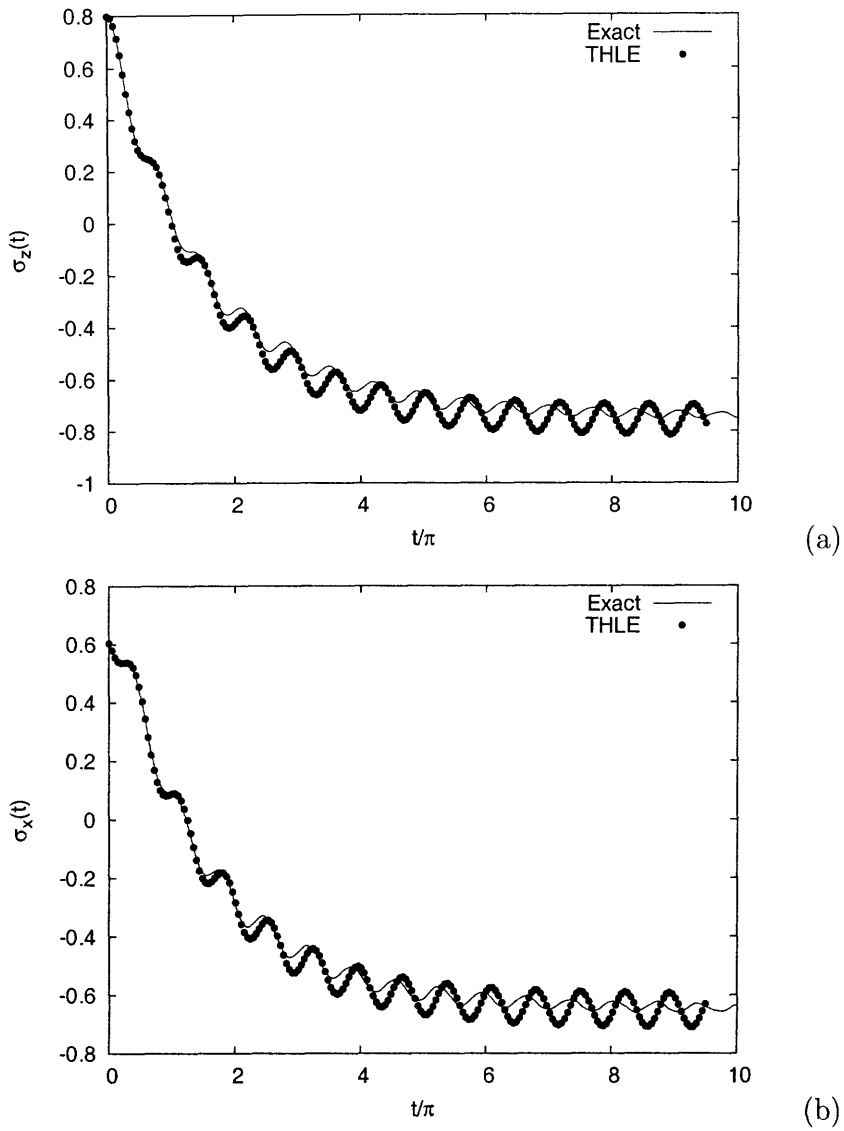

Figure 3.9: The dynamics of (a) $\sigma_z(t)$ and (b) $\sigma_x(t)$ in the optimal frame($\theta = 0$), for the Spin Boson Case VI ($\beta\Delta = 50$, $\eta = 0.5\Delta$, $\omega_c = 5\Delta$ and $\epsilon = 1\Delta$).

Case VII ($\beta\Delta = 0.5$, $\eta = 0.5\Delta$, $\omega_c = 0.25\Delta$ **and** $\epsilon = \Delta$)

So far the current treatment has been successful, but still one can always find pathological regimes, even in the optimal frame. If we choose a system where the perturbation Δ is large compared to the critical frequency ω_c, but comparable to η and ϵ, it is possible that the simple rotation is unable to find a frame where the perturbation is small enough. To show such

systems exist, we set $\omega_c = 0.25\Delta$, $\epsilon = \Delta$, $\eta = 0.5\Delta$ and $\beta\Delta = 0.5$. We only show the result of $\sigma_z(t)$ in the optimal frame, where $\theta = 0.083\pi$. In figure 3.10, the exact result displays some initial underdamped relaxation and eventually switches to an exponential decay. Our result exhibits a very different behavior and only agrees with the exact result for the initial decay. Since the minimization of the perturbation is not so effective with this parameter setting, terms beyond the second order in the memory kernel are expected to have strong effects on the dynamics. For example, the oscillations seen in the exact result might be due to coherent four-hop and six-hop terms. Neglect of these terms will naturally lead to poor agreement, similar to what we have seen in Case II.

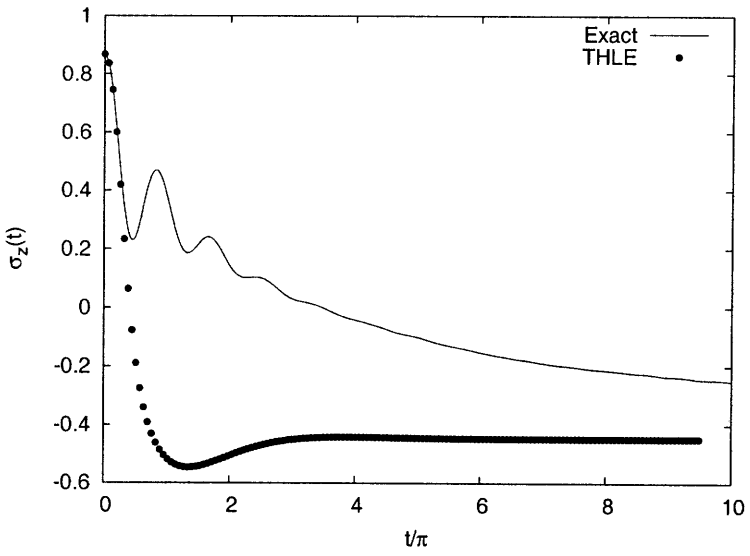

Figure 3.10: The dynamics of $\sigma_z(t)$ in the optimal frame($\theta = 0.083\pi$), for the Spin Boson Case VII ($\beta\Delta = 0.5$, $\eta = 0.5\Delta$,$\omega_c = 0.25\Delta$ and $\epsilon = 1\Delta$).

3.4 Discussion

The population dynamics of the spin-boson model have been widely studied and many approximate quantum master equations similar to the THLE exist. The non-interacting blip approximation(NIBA) [32, 26] is probably the most recognizable and similar to the THLE. Traditionally it is associated with the spin-boson system in the unrotated frame ($\theta = 0$),

where the diabatic coupling operator is a constant, Δ. For a more general electron transfer system, linear Langevin equations governing the population dynamics have also been derived using either the projection operator technique[30, 35, 36, 29] or by simply assuming fast bath relaxations[31]. All of the above approximations share a common feature: a noise term is present in the Langevin equation. Furthermore, they can all be written in the form of Eq. 3.18 with varying definitions of the memory kernel and the noise term. The presence of the noise term is the major difference between the THLE in the current article and these traditional Langevin equations, or quantum master equations since the relevant variables are diagonal elements in the density matrix.

By elimination of the noise term, the THLE is guaranteed to give the prescribed equilibrium values at long time. On the other hand, equation 3.18 relies on the balance of fluctuation and dissipation for the correct population relaxations. Though Eq. 3.18 is an exact expression, a similar perturbative treatment as used in deriving Eq. 3.24, if used on Eq. 3.18, can result in serious problems at long time, as we now show.

When the relevant variable is the population rather than its fluctuation, Eq. 3.18 becomes:

$$\dot{P}_1(t) = -\int_0^t K'(t-s)P_1(s)ds + f(t). \tag{3.43}$$

The derivation used for Eq. 3.24 may be applied to derive the second order expressions of the memory kernel $K'(t)$ and the noise $f(t)$. The projection operator method can also be used[33, 30, 31, 35]. Here we simply quote the results:

$$\begin{aligned} K'^{(2)}(t) &= -[\ddot{P}_1^{(2)}(t) + \ddot{P}_2^{(2)}(t)] \\ f^{(2)}(t) &= -\dot{P}_2^{(2)}(t) \end{aligned} \tag{3.44}$$

where the second order populations $P_1^{(2)}(t)$ and $P_2^{(2)}(t)$ have been defined previously. Replacing the exact kernel and the noise by their second order approximations results in a two-hop

Langevin equation with noise:

$$\dot{P}_1(t) = -\int_0^t K'^{(2)}(t-s)P_1(s)ds + f^{(2)}(t). \tag{3.45}$$

Again, a Markovian approximation to Eq. 3.45 reveals the long time behavior of $P_1(t)$:

$$\dot{P}_1(t) = -\tilde{K}'^{(2)}P_1(t) + \tilde{f}^{(2)} \tag{3.46}$$

where $\tilde{K}'^{(2)} = \int_0^\infty dsK'^{(2)}(s) = -\lim_{t\to\infty}[\dot{P}_1^{(2)}(t) + \dot{P}_2^{(2)}(t)]$ and $\tilde{f}^{(2)} = \lim_{t\to\infty} f^{(2)}(t) = -\lim_{t\to\infty} P_2^{(2)}(t)$. The solution of Eq. 3.46 is:

$$P_1(t) = [1 - \frac{\tilde{f}^{(2)}}{\tilde{K}'^{(2)} + \tilde{f}^{(2)}}]e^{-\tilde{K}'^{(2)}t} + \frac{\tilde{f}^{(2)}}{\tilde{K}'^{(2)} + \tilde{f}^{(2)}}. \tag{3.47}$$

The population on state $|\bar{1}\rangle$ decays from its initial value 1 at the rate of $\tilde{K}'^{(2)}$ to its final value $\frac{\tilde{f}^{(2)}}{\tilde{K}'^{(2)}+\tilde{f}^{(2)}}$. The second order rate $\tilde{K}'^{(2)}$ can be identified as the quantum golden rule rate:

$$\begin{aligned} \tilde{K}'^{(2)} &= -\lim_{t\to\infty}[\dot{P}_1^{(2)}(t) + \dot{P}_2^{(2)}(t)] \\ &= \int_0^\infty ds\langle e^{i\hat{\bar{H}}_0 s}\sigma_x\hat{\bar{V}}e^{-i\hat{\bar{H}}_0 s}\sigma_x\hat{\bar{V}}\rangle. \end{aligned} \tag{3.48}$$

The final equilibrium population on state one is:

$$\begin{aligned} \frac{\tilde{f}^{(2)}}{\tilde{K}'^{(2)} + \tilde{f}^{(2)}} &= \lim_{t\to\infty}\frac{\dot{P}_2^{(2)}(t)}{\dot{P}_1^{(2)}(t) + \dot{P}_2^{(2)}(t)} \\ &= \frac{\mathrm{tr}_N e^{-\beta\hat{\bar{h}}_1}\hat{\bar{V}}^2}{\mathrm{tr}_N e^{-\beta\hat{\bar{h}}_1}\hat{\bar{V}}^2 + \mathrm{tr}_N e^{-\beta\hat{\bar{h}}_2}\hat{\bar{V}}^2} \end{aligned} \tag{3.49}$$

where in the second step we have made use of the ergodic theorem. The equilibrium population predicted by the two-hop Langevin equation with noise in Eq. 3.49 is different from what is expected from the zeroth order approximation in Eq. 3.7. The thermo-dynamical

result in Eq. 3.7 is a controlled perturbative result and will be valid if one has taken steps to minimize $\hat{\tilde{V}}$. Eq. 3.49, however, does not correspond to any expansion of the equilibrium density matrix and its range of validity is, at best, questionable.

For a spin-boson problem in the unrotated frame, where the diabatic coupling $\hat{V}$ is a constant, Eq. 3.49 is equivalent to the zeroth order approximation in Eq. 3.7. However, in general the optimal frame is a rotation of the original system that gives a non-constant diabatic coupling $\hat{\tilde{V}}$. In this situation, Eq. 3.45 can give erroneous results. In order to illustrate this, we consider a general rotation of the system specified by the angle θ and the long time populations reached by Eq. 3.24(without noise) and Eq. 3.45(with noise) as a function of the angle θ. As a side note, due to the log-divergent behavior of the Debye spectral density, Eq. 3.49 happens to agree with Eq. 3.7 in all frames because the differences between the two are always finite, while the common terms always diverge. Thus, one essentially ends up comparing $\frac{P\infty}{\infty+a}$ to $\frac{P\infty}{\infty+b}$, which always results in the same answer. To give a more realistic picture here, we use the Ohmic spectral density instead:

$$J(\omega) = \frac{\pi}{2}\alpha\omega e^{-\omega/\omega_C}. \tag{3.50}$$

Due to the exponential cutoff, the Ohmic density gives finite bath integrals and a realistic variation of the equilibrium population. We choose the parameters to mimic Case V, since the diabatic coupling Δ is rather small in this case compared to the critical frequency $\omega_c = 5\Delta$. Hence, one would expect both Eq. 3.24 and Eq. 3.45 to work relatively well in any frame because both equations are correct to second order in the diabatic coupling. With an Ohmic bath, the reorganization energy is $2\alpha\omega_c$, therefore the value of α is set to $\frac{\eta}{\omega_c} = 0.1$ in order to reproduce the reorganization energy in case V, $2\eta = 1$. Figure 3.11 shows as the rotation angle θ changes, the long time population from Eq. 3.24 follows the exact result faithfully in the entire range of θ. On the other hand, the long time population from Eq. 3.45 shows wild oscillations and large deviations from the exact result in a rather random fashion. In

particular, the optimal angle for case V is $\theta = 0.083\pi$. At this value of θ, Eq. 3.45 predicts the population to reach -0.88 while Eq. 3.24 gives a long time value of -0.60, in close agreement with the exact result, which is -0.53.

This leads to the conclusion that while both equations are correct at short time due the perturbative nature, only Eq. 3.24, without the noise term, leads to the correct population relaxation at long time.

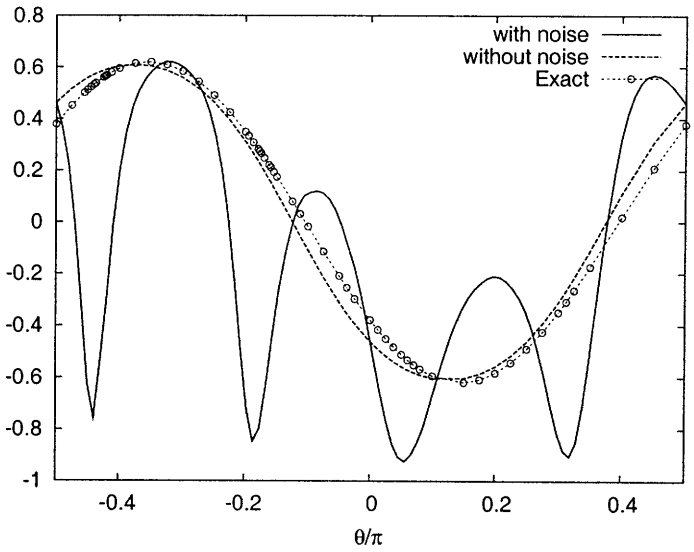

Figure 3.11: The long time limit of the rotated $\tilde{\sigma}_z$ obtained by Eq. 3.45(with noise) and Eq. 3.24(without noise), with $\beta\Delta = 0.5$, $\alpha = 0.1$, $\omega_c = 5\Delta$ and $\epsilon = 1\Delta$.

3.5 Conclusion

In this article, we developed a linear Langevin equation - the THLE - that can be used to describe the population dynamics in electron transfer systems. In this context, one chooses the *fluctuation* in the population from equilibrium as the relevant variable and treats the coupling, $\hat{V}$, between the two electronic states perturbatively. By rotating the electronic basis, it is possible to minimize the effect of the perturbation on both the equilibrium populations and the dynamics. The Langevin framework we propose is quite general and could easily be applied to other types of problems: all of the approximations are wrapped up in

the prediction of the equilibrium value of the relevant variable and the perturbative computation of the memory kernel. This framework is flexible and intuitive: the equations enforce the long time equilibration of the problem by design, and the short time dynamics are systematically improvable via controlled approximations to the memory kernel. In the present context, we find that surprisingly good results can be obtained even at lowest order (zeroth order populations and second order memory kernel).

In order to validate our results, benchmark calculations were performed on a simple spin-boson system with various parameter settings. When the diabatic coupling is small (Cases I and V), excellent agreement is found between the THLE results and the exact result. While this is expected, surprisingly good agreement is also reached where the diabatic coupling Δ is comparable in strength to the bath frequency ω_c (Case IV), as long as the reorganization energy is large. In this case, long-range decoherence makes coherent multiple-hop events less significant than the two-hop process. The THLE also gives good results in the small damping regime at low temperature (Cases III and VI), which is traditionally difficult for perturbative approximations of population dynamics[26, 94]. The only situation we have found where the THLE fails is when the diabatic coupling and reorganization are large and comparable to one another (Case II and Case VII). In this situation, multiple-hop events become important, and a more accurate expansion is likely called for. We find, interestingly, that the Langevin equation with a fluctuating force is much less reliable than one without it in terms of predicting the dynamics in the presence of an energy bias. We note that the difference between the two approaches lies entirely in the definition of the initial densities. In the latter case the initial density variation lives entirely inside the relevant space, whereas the fluctuating force reflects the portion of the initial variation that is outside the relevant operator space. Hence our results argue strongly that, when using Langevin equations for non-equilibrium dynamics, every effort should be made to eliminate the fluctuating force by an appropriate choice of initial states.

Application-wise, since the second order perturbation of the population have well-defined

semiclassical approximation, they may be obtained from classical simulations in an atomistic electron transfer system. The diabatic potential energies and the diabatic coupling could be computed on-the-fly along the classical trajectories using empirical valence bond [101, 102, 103] or constrained density functional theory [10, 12, 13, 11], for example. The computation effort here would be significant, as one needs to compute the equilibrium averaged time correlation function in Eq. 3.21. However, this is not significantly more effort than is required by an Eherenfest or surface-hopping treatment; in each case a swarm of trajectories must be propagated and it is simply a question of how many representatives are required to represent the ensemble. In particular, the short-time nature of the THLE memory kernel suggests that short-time trajectory data should be enough to extract the long time dynamics. In the near chapter, we will explore the possibility of sampling trjaectories to obtain the memory kernel and study the convergence of sampling in detail.

Chapter 4

Effects of Monte Carlo sampling on the Langevin equation in electron transfer dynamics

4.1 Introduction

The Monte Carlo sampling technique has been a valuable tool in the simulations of physical and chemical systems[104, 105]. Equilibrium properties of systems can routinely be obtained by Monte Carlo sampling in the entire phase space. For classical systems various importance sampling schemes have been developed to achieve better statistics with a fewer number of samplings[106]. The path integral Monte Carlo method is often the *de facto* choice for computing thermodynamic properties of quantum systems in the condensed phase[104, 107, 108, 109, 110, 111].

The applications of the Monte Carlo method can also be extended to the computation of time-dependent quantities such as the time correlation function:

$$C(t) = \int dqdpe^{-\beta H} A(t)B. \tag{4.1}$$

The distribution function is often used to generate initial values of $q's$ and $p's$. Then

trajectories are launched from these initial values to compute the time dependent quantities $A(t)B$. These quantities are then summed over to obtained the thermal average of the time correlation function. Monte Carlo sampling technique has been applied in such manner whether these observables A and B are classical, quantum mechanical or quasi-classical[95, 100, 19, 112].

The main limitation of Monte Carlo sampling techniques to realistic chemical systems is often the slow rate of convergence. As for *ab initio* calculations, such as the Car-Prrinello dynamics[105], the computational cost of running trajectories can be quite large and an excessive number of samplings to achieve statistical convergence can prohibit the practical use of Monte Carlo sampling. Therefore the efficiency of Monte Carlo sampling should be tested before one starts an expensive *ab initio* calculation. When it is revealed that a straightforward implementation is unlikely to yield satisfactory results within the computational constraint, smoothing techniques should be thought of and implemented to obtain better convergence.

In the previous section, we have proposed and validated the two-hop Langevin equation(THLE) approach to study real time population dynamics in an electron transfer system. Bench mark results proved to be promising and give hope for applications of the THLE to realistic chemical systems. In the THLE approach, one needs to compute the memory kernel, which is similar to the time correlation function seen in equation 4.1. However, these time correlation functions, in the simple spin-boson system, are evaluated by analytically integrating over the bath degrees of freedom, in order to test only the accuracy of the THLE. In general, it is not possible to have closes expressions of any non-trivial time-dependent quantities and either quantum or classical trajectories must be sampled to compute thermal averages. Since we are interested in *ab initio* simulations of electron transfer systems, evaluations of trajectories are likely to require long time and large computing resources. Therefore it is important to study the rate of convergence of the Monte Carlo sampling in evaluating the memory kernel needed for the THLE. In cases when too many trajectories are require

for statistical convergence, we develop smoothing techniques to improve the Monte Carlo sampling without running additional trajectories.

In section II, we propose an importance sampling scheme to evaluate the memory kernel. In section III, we apply the sampling scheme to the simple spin-boson system where the memory kernel can be evaluated analytically. Results from both the Monte Carlo and analytic evaluations are compared together across different parameter regimes. A simple functional form is also proposed to fit the Monte Carlo results to extract more information for a given number of trajectories. We end by summarizing the key features and feasibility of using the THLE with Monte Carlo sampling to study electron transfer systems as well as discussing further works need to be done to implement the THLE to a realistic system.

4.2 The Monte Carlo Scheme

The two-hop Langevin equation(THLE) is :

$$\delta\dot{P}_1(t) = -\int_0^t K^{(2)}(s)\delta P_1(t-s)ds. \tag{4.2}$$

It is convenient to integrate equation4.2 once:

$$\delta P_1(t) - \delta P_1(0) = -\int_0^t \bar{K}(s)^{(2)}(s)\delta P_1(t-s)ds \tag{4.3}$$

where $\bar{K}^{(2)}(t) = \int_0^t K^{(2)}(s)ds$. $\bar{K}^{(2)}(t)$ is the integrated kernel and maybe regarded as the time dependent electron transfer rate. Instead of decaying to zero at long time as the memory kernel $K^{(2)}(t)$, the integrated kernel decays to a constant, which is the long time decay rate of the population. Equation 4.3 does not involve any time derivative and can be easily solved using forward substitution.

For the spin-boson model, one can analytically integrate over the bath degrees of freedom. For a realistic system, where the potentially energy surface is not known globally, one must

resort to trajectory-based methods to compute the second order kernel, or equivalently, the second order population. To begin, we write in full the second order expression for the population:

$$\begin{aligned} P_1^{(2)}(t) &= -\int_0^t d\tau \int_0^\tau ds f(\tau, s). \\ f(\tau, s) &= \frac{2}{\mathrm{tr} e^{-\beta \hat{h}_N}} \mathrm{Re}\{ \mathrm{tr}[e^{-\beta \hat{h}_N} e^{i\hat{h}_1 \tau} V e^{-i\hat{h}_{@}(\tau - s)} V e^{-i\hat{h}_1 s}]\} \end{aligned} \tag{4.4}$$

The integrand f in equation 4.4 is the most costly part of the calculation. At first glance, the two-dimension function f depends both on τ and s therefore its calculation would require N^2 *ab initio* trajectories where N is the number of time steps. Nonetheless, it can be shown that the cost is only proportional to N.

By defining the dephasing operator $\hat{J}(t, \beta)$ as:

$$\hat{J}(t, \beta) = e^{i\hat{h}_2 t} V e^{-i\hat{h}_1 t} e^{-\frac{\beta}{2}\hat{h}_N}, \tag{4.5}$$

the function $f(\tau, s)$ can be rewritten as:

$$f(\tau, s) = 2\mathrm{Re} \frac{\mathrm{tr} \hat{J}^\dagger(\tau, \beta) \hat{J}(s, \beta)}{\mathrm{tr} \hat{\rho}_0}. \tag{4.6}$$

Any complete basis can then be used to evaluate the trace:

$$\begin{aligned} f(\tau, s) &= 2\mathrm{Re} \sum_n \frac{\langle n | \hat{J}^\dagger(\tau, \beta) \hat{J}(s, \beta) | n \rangle}{\mathrm{tr} e^{-\beta \hat{h}_N}} \\ &= 2\mathrm{Re} \sum_n \frac{\langle n, \tau; \beta | n, t; \beta \rangle}{\langle n | e^{-\beta h_n} | n \rangle} \frac{\langle n | e^{-\beta h_n} | n \rangle}{\mathrm{tr} e^{-\beta \hat{h}_N}}, \end{aligned} \tag{4.7}$$

where the hopped quantum state $|n, t; \beta\rangle = \hat{J}(s, \beta)|n\rangle$. Equation 4.7 suggests evaluating the trace by sampling the initial state $|n\rangle$ from the distribution $\frac{\langle n | e^{-\beta h_n} | n \rangle}{\mathrm{tr} e^{-\beta \hat{h}_N}}$. Such sampling can be carried out by, for example, the Metropolis sampling technique.

An often used and convenient representation for quasi-classical simulations[113][59, 60,

113] is the coherent state representation[69]. The identity operator in the coherent state representation is:

$$\hat{I}_n = \frac{1}{2\pi^M} \int |\mathbf{q}, \mathbf{p}\rangle\langle \mathbf{q}, \mathbf{p}| d\mathbf{q} d\mathbf{p} \tag{4.8}$$

where the M-dimensional canonical coherent state $|\mathbf{q}, \mathbf{p}\rangle$ is the product of one dimensional canonical coherent states

$$|\mathbf{q}, \mathbf{p}\rangle = \prod_{i=1}^{M} |q_i, p_i\rangle. \tag{4.9}$$

In the position representation, a canonical coherent state is a Gaussian wavepacket centered at q and p in phase space:

$$\langle x|z\rangle = \frac{1}{\sqrt{2\pi}} e^{-\frac{1}{2}(x-q)^2 + ip(x-\frac{q}{2})}. \tag{4.10}$$

A trace evaluated using the coherent state representation is then:

$$\mathrm{tr}A = \int \frac{d\mathbf{q}d\mathbf{p}}{2\pi^M} \langle \mathbf{q}, \mathbf{p}|A|\mathbf{q}, \mathbf{p}\rangle. \tag{4.11}$$

Equation 4.6 can then be written as:

$$\begin{aligned} f(\tau, s) &= 2\mathrm{Re} \int \frac{d\mathbf{q}d\mathbf{p}}{2\pi^M} \frac{\langle \mathbf{q}, \mathbf{p}|\hat{J}^\dagger(\tau, \beta)\hat{J}(s, \beta)|\mathbf{q}, \mathbf{p}\rangle}{\mathrm{tr}e^{-\beta h_N}} \\ &= 2\mathrm{Re} \int \frac{d\mathbf{q}d\mathbf{p}}{2\pi^M} \frac{\langle \mathbf{q}, \mathbf{p}; \tau, \beta|\mathbf{q}, \mathbf{p}; s, \beta\rangle}{\mathrm{tr}e^{-\beta h_N}} \\ &= 2\mathrm{Re} \int \frac{d\mathbf{q}d\mathbf{p}}{2\pi^M} \frac{\langle \mathbf{q}, \mathbf{p}; \tau, \beta|\mathbf{q}, \mathbf{p}; s, \beta\rangle}{\langle \mathbf{q}, \mathbf{p}|e^{-\beta h_N}|\mathbf{q}, \mathbf{p}\rangle} \frac{\langle \mathbf{q}, \mathbf{p}|e^{-\beta h_N}|\mathbf{q}, \mathbf{p}\rangle}{\mathrm{tr}e^{-\beta h_N}} \\ &= 2\mathrm{Re} \int \frac{d\mathbf{q}d\mathbf{p}}{2\pi^M} \rho(\mathbf{q}, \mathbf{p}; \beta) \frac{\langle \mathbf{q}, \mathbf{p}; \tau, \beta|\mathbf{q}, \mathbf{p}; s, \beta\rangle}{\langle \mathbf{q}, \mathbf{p}|e^{-\beta h_N}|\mathbf{q}, \mathbf{p}\rangle} \end{aligned} \tag{4.12}$$

where $|\mathbf{q}, \mathbf{p}; s, \beta\rangle = \hat{J}(s, \beta)|\mathbf{q}, \mathbf{p}\rangle$ and the initial density in coherent state representation is $\rho(\mathbf{q}, \mathbf{p}; \beta) = \frac{\langle \mathbf{q}, \mathbf{p}|e^{-\beta h_N}|\mathbf{q}, \mathbf{p}\rangle}{\mathrm{tr}e^{-\beta h_N}}$. The last line in equation 4.12 suggests that the trace can be evaluated using Monte Carlo method by taking the initial density $\rho(\mathbf{q}, \mathbf{p}; \beta)$ as the distribution function(or any valid distribution functions, but $\rho(\mathbf{q}, \mathbf{p}, \beta)$ is an obvious choice) for picking initial values of $\mathbf{q}'s$ and $\mathbf{P}'s$. Each initial wavepacket will then lead to a trajectory $|\mathbf{q}, \mathbf{p}; t, \beta\rangle$.

Since $\langle \mathbf{q}, \mathbf{p}; t, \beta|$ is the complex conjugate of $|\mathbf{q}, \mathbf{p}; t, \beta\rangle$, one only needs to compute various $|\mathbf{q}, \mathbf{p}; t, \beta\rangle's$ and compute their overlaps at different times. Hence the numerical cost scales as N, the number of time step instead of N^2.

It should be noted that for linear dynamics, i.e., harmonic bath, the hopped trajectory $|\mathbf{q}, \mathbf{p}; t, \beta\rangle$ is simple another coherent state with shifted $\mathbf{q}$ and $\mathbf{p}$ and can be computed analytically. However, in general, $|\mathbf{q}, \mathbf{p}; t, \beta\rangle$ needs to be computed either using exact quantum mechanics(as in the case of uncoupled bath modes) or using various quasi-classical approximations. The hopped trajectory $|\mathbf{q}, \mathbf{p}; t, \beta\rangle$ involves propagating the initial wavepacket $|\mathbf{q}, \mathbf{p}\rangle$ under $\hat{h}_N$ in imaginary time, $i\frac{\beta}{2}$, under the dynamics of state $|1\rangle$ forward in time, hopping to state $|2\rangle$ and finally propagating in state $|2\rangle$ backward in time. Since the propagation is always on a single surface for any given time, $|\mathbf{q}, \mathbf{p}; t, \beta\rangle$ has a very strong classical resemblance and many quasi-classical methods are available for its computation[5, 105, 113].

In summary, an *ab initio* calculation using the THLE involves three major approximations. The first is the THLE itself, where the second order kernel is assumed to be dominant. This approximation has been tested in several different parameter regimes in our previous work. The second approximation is the Monte Carlo evaluation of the trace in equation4.12. We will study its efficiency and potential improvement in the section that follows. We will leave validation of the last approximation, the quasi-classical approximation for the hopped trajectories, $|\mathbf{q}, \mathbf{p}; t, \beta\rangle$, to future work.

4.3 Results

In order to test the Monte Carlo scheme, we will employ the simple spin-boson system again, where the the semi-classical approximation of the hopped trajectories are exact due the harmonic bath. Therefore results will only reveal the errors from the Monte Carlo evaluation.

The initial density matrix is chosen to be

$$\hat{\rho}(0) = \begin{pmatrix} \hat{\rho}_y & 0 \\ 0 & 0 \end{pmatrix} \tag{4.13}$$

, where $\hat{\rho}_y$ is the distribution of the nuclei:

$$\hat{\rho}_y = e^{-\beta(H_0 - y\sum_i c_i x_i)}.$$

The parameter y specifies the average position of the nuclei. $y = -1$ corresponds to the equilibrium distribution on state $|1\rangle$. To be consistent with the previous chapter, we look at an non-equilibrium distribution with $y = 0$, referring to a nuclear distribution in between the equilibrium positions of state $|1\rangle$ and state $|2\rangle$. The matrix element in equation 4.12 can be calculated analytically:

$$\begin{aligned} f(\tau, s) &= \int d\mathbf{q}d\mathbf{p}\rho(\mathbf{q}, \mathbf{p}; \beta, y) \\ &= \exp\{\sum_i i\frac{2c_i}{\omega_i}e^{-\beta\omega_i/2}[(\cos\omega_i t - \cos\omega_i s)\frac{p_i}{\omega_i} \\ &= +(\sin\omega_i s - \sin\omega_i t)q_i] \\ &= -i\frac{2c_i^2}{\omega_i^3}y(\sin\omega_i t - \sin\omega_i s)(1 - e^{-\beta\omega_i/2}) \\ &= +\frac{2c_i^2}{\omega_i^3}[e^{-i\omega_i(t-s)} + i\sin\omega_i t - i\sin\omega_i s - 1] \end{aligned} \tag{4.14}$$

where the distribution function

$$\begin{aligned} \rho(\mathbf{q}, \mathbf{p}; \beta, y) &= \langle \mathbf{q}, \mathbf{p}|\hat{\rho}_y|\mathbf{q}, \mathbf{p}\rangle / \mathrm{tr}\hat{\rho}_y \\ &= \prod_i \frac{1 - e^{-\beta\omega_i}}{2\pi} e^{-\frac{1-e^{-\beta\omega_i}}{2}\omega_i(q_i - y\frac{c_i}{\omega_i^2})^2} e^{-\frac{1-e^{-\beta\omega_i}}{2\omega_i}p_i^2}. \end{aligned} \tag{4.15}$$

Note that the equation 4.14 can be computed analytically(see the previous chapter for de-

tails). However, to study the effects of Monte Carlo sampling on the computations of the memory kernel and the populations, we use the density function in equation 4.15 as the distribution function to sampling initial values of $q's$ and $p's$. The Monte Carlo results are then compared to the analytic results.

First we look at the convergence of the integrated memory kernel and the time dependent population with respect to the number of trajectories one has to sample. Since in reality we would like to study ultrafast electron transfer reactions, here we choose a fast bath with the critical frequency, $\omega_c = 5\Delta$. The system-bath coupling is chosen to be moderate with $\eta = 0.5\Delta$ and the temperature is finite, $\beta\Delta = 0.5$, since too low a temperature will only require a single trajectory for convergence. The energy bias in between the two electronic states is chosen to be $\epsilon = 1\Delta$, since in most realistic cases the donor and acceptor states have different energy levels.

Figure 4.1 shows convergence of the second order integrated memory kernel and the population with respect to different numbers of trajectories, as well as the standard deviation of the memory kernel. In fig4.1(a) the analytical memory kernel is oscillatory at short time and reaches a plateau around $t = 6$. Hence a strong non-Markovian behavior should be expected for the population. The Monte Carlo results start resembling the analytical kernel after 1000 trajectories with 200 trajectories being insufficient. At long time, however, the Monte Carlo results always show increasingly spurious oscillations around the long time rate. The reason is reflected in fig4.1(b) where the standard deviation is shown to decay as $1/\sqrt{N}$[111], where N is the number of trajectories. But for any given number of trajectories, the standard deviation grows linearly with t at long time. This is due to the fact that the integrated kernel is an integral over t; therefore the standard deviation accumulates over time. Fig4.1(c) shows the different population curves computed from memory kernels with different numbers of sampling trajectories. The curve constructed from 200 trajectories deviates significantly from the analytical result, even at short time, where most electron transfer takes place. However, both curves from 1000 and 4000 trajectories accurately reproduced

the analytical results at short time(before $t = 6$), after which the spurious oscillations seen in fig4.1(a) cause increasing error in the populations.

4.3.1 Fitting the kernel

Fig4.1 reveals several features about the Monte Carlo sampling scheme for the memory kernel and its subsequent use to compute the population. Clearly, with a sufficient number of trajectories, the memory kernel will converge for any time window one desires. On the other hand, one must sample a growing number of trajectories in order to converge the long time tail of the memory kernel. The short time behavior of the population is likely to converge quickly. The long time population, however, is affected by the spurious oscillation of the sampled kernel, and the error increases in time due to the memory effect.

A simple solution is to use more trajectories. This can be a problem for *ab initio* calculations since computing trajectories can be computationally expensive. It is also wasteful to use a large number of trajectories to force the memory kernel to become constant at long time since no new information is obtained once the integrated kernel reaches the right rate. To be more efficient, one can fit the memory kernel to a prescribed functional form, in which known qualitative behavior of the integrated memory kernel is built in, such as decaying to a constant at long time. This may enable one to use only a small number of trajectories(as in fig4.1, 1000 trajectories) to converge the short time non-Markovian part and remain at the right constant at long time. We also know that the integrated kernel is an odd function in t and that $\bar{K}(0) = 0$. So one could assume that the integrated memory takes the functional form:

$$\tilde{K}(t) = [R + \sum_{i=0}^{n} c_i J_{2i}(bt)] \tanh(at) \tag{4.16}$$

where R is the long time rate. The hyperbolic tangent function has the properties of being zero at $t = 0$ and constant at large t as well as being an odd function in t. $J'_{2i}s$ are even order Bessel functions of the first kind. They are used to simulate the non-Markovian behavior of

the integrated kernel at short time. Since the most valuable information is the short time non-Markovian behavior of the memory kernel, we use the inverse of the variance as the statistical weight of the fitting procedure:

$$L = \sum_i \frac{1}{Var[\bar{K}(t_i)]}[\bar{K}(t_i) - \tilde{K}(t_i)]^2$$

where L is the logistic function that we minimize by varying a, b, R and c_i's.

The fitting function is applied to the integrated kernel with 1000 trajectories. Fig4.2 shows the populations computed from the analytical, the fitted and the unfitted integrated kernels, with 1000 trajectories. The fit stops at 10 Bessel functions and addition of higher order functions shows no more significant improvement. The fitted population accurately reproduces the non-Markovian relaxation of the population at short time. The long time spurious oscillations observed in the unfitted result are also removed by the fitting procedure. Notice even with 4000 trajectories, the spurious oscillations persist without fitting, as seen in fig4.1(a). Thus, in this case, we observe that substantial savings in Monte Carlo sampling can be obtained by fitting un-converged results to rather simple functional form.

4.3.2 Rate of convergence in different regimes

The rate of convergence of the Monte Carlo sampling depends on various parameters in the spin-boson model. To examine the effects of different parameters on the Monte Carlo convergence, we perform calculations on systems with different energy bias as well as the system-bath coupling, with fixed numbers of trajectories.

To look at the effect of energy bias on the convergence of the population, we compute the populations from 1000 trajectories with different energy bias. Fig4.3 shows populations computed from 1000 trajectories with $\epsilon = 0$, 1Δ and 2Δ, while other parameters are the same as in figure4.1. In fig4.3(a), the energy bias is set to zero. The population remains coherent for longer time compared to what is seen in figure4.1(b) where $\epsilon = 1\Delta$, and oscillates

around its equilibrium value, $P = 0.5$. The Monte Carlo result only compares well to the analytical result up to $t = 4$, then significantly deviates from it. The fitted result shows significant improvement and agrees with the analytic result for all time. With $\epsilon = 1\Delta$, results in fig4.3(b) show the analytical result become more incoherent. The Monte Carlo result shows some improvement but the long time deviation is still visible. Again we see that the spurious oscillations are removed at long time by the fitted memory kernel. With the energy bias $\epsilon = 2\Delta$, the Monte Carlo result and the analytical results agree well for the entire time window. Both show damped oscillations and become exponentially decaying roughly after $t = 4$. In conclusion, as the energy bias increases, the population decay becomes more incoherent and the Monte Carlo result converges more quickly.

The energy bias, in the spin-boson model, measures the vertical distance between the two electronic states while the system-bath coupling parameter η measures the horizontal distance. To see the effects of the system-bath coupling strength on the convergence of the populations, we calculate the populations from 1000 trajectories with different values of η. Figure4.4 display populations with $\eta = 0.5\Delta$, 1Δ and 2Δ, with other parameters being identical to those used in figure4.1. Figure4.4(a) shows the population with a small system-bath coupling, $\eta = 0.5\Delta$. The analytical population remains coherent up to $t = 15$ and reaches its equilibrium value afterwards. The Monte Carlo result starts deviating from the analytical result at $t = 5$, while up to 20% population has not been transferred. The population from the fitted kernel remains accurate for longer time up to $t = 7$ and shows the correct relaxation at long time limit. However, it shows wrong oscillation periods between $t = 7$ and $t = 15$, where visible coherent relaxation is still visible. This suggests that in the small damping regime, more than 1000 trajectories might be needed to achieve better accuracy. Figure4.4(b) corresponds to a stronger system-bath coupling: $\eta = 1\Delta$. The analytical result shows much stronger decoherence than the previous case. The electron transfer is also faster in this case with the equilibrium value reached at $t = 7$, compared to $t = 15$ as in figure4.4(a). The agreement between the Monte Carlo result and the analytical

result has also improved. Though spurious oscillations around the equilibrium value are still present, good agreement is achieved before $t = 6$, where most electron transfer takes place. The population from the fitted kernel extends to range of accuracy beyond $t = 6$ and provides more realistic damping at long time. Figure4.4(c) shows, with an even stronger system-bath coupling, the population dynamics is almost incoherent and reaches its equilibrium at shorter time, around $t = 4$. The Monte Carlo result again agrees well with the analytical result up to the point where equilibrium is reached. Then it starts showing spurious oscillations, which have been observed consistently. The population from the fitted is seen to be accurate to all time. From the three cases in figure4.4, we may conclude that as the system-bath coupling becomes stronger, the population dynamics will become more incoherent and the electron transfer process will complete at faster pace. The Monte Carlo result is likely to converge more quickly for the short time but once electron transfer is complete, oscillations around the equilibrium value should be expected. The fitting procedure proves to be reliable in all three cases. In the strong coupling regime, figure 4.4(c) indicates the fitting procedure is likely to be the most effective.

4.4 Discussion and Conclusion

At the end of section II, we summarized the three major approximations involved in using the THLE to compute the population dynamics in a realistic electron transfer system: the THLE itself, the Monte Carlo sampling of trajectories and the quasi-classical approximation to these trajectories. In this article, we examined the second approximation: the Monte Carlo calculation of the integrated memory kernel.

By expressing the integrated memory kernel as the overlap of hopped trajectories at different times(equation 4.7), we showed that the computation of the memory kernel can be done in N time steps, with $N\Delta t$ being the total time of the simulation, instead of N^2 time steps. This leads to significant reduction in computing time. For example, an ultrafast

electron transfer reaction typically happens in the pico-second time window[19, 20]. The vibrational periods of the nuclei are on the scale of 20 fs, therefore a reasonable time step would on the order of 5 fs. A trajectory of 1ps will require $N = 200$ time steps, which requires 200 *ab initio* calculations in condensed phase. Suppose one *ab initio* calculation takes 5 minutes to complete, then the computation of this trajectory will take 1000 minutes, or approximately 17 hours. If the computation of the memory kernel scales as N^2, this means the memory kernel resulting from 1 initial condition will take $17 \times 20 = 340$ hours. The difference between 17 hours and 340 hours is significant: one is feasible and the other is not.

To test only the efficiency of Monte Carlo sampling, we applied the proposed importance sampling scheme to the spin-boson system, where the quasi-classical approximation to the trajectories is exact. By comparing the Monte Carlo results with the analytic result in various different regimes, we found that with a few thousand trajectories, the Monte Carlo result converge well for short time where most electron transfer takes place but shows unrealistic oscillations at long time. The statistical errors from the Monte Carlo procedure increases with time but since electron transfer tends to become exponential as time increases, valuable information from the integrated memory kernel, in fact, decreases. This enable us to fit the integrated memory kernel with prescribed functional forms and use the inverse of the variance as a weight function. The fitting procedure is shown to work well. It is especially effective at removing these spurious oscillations at long time when the dynamics becomes Markovian. From figure 4.1 and figure 4.2, we found the fitted result using 1000 trajectories is more accurate than the un-fitted result using 4000 trajectories. Keeping in mind that one trajectory could take 17 hours to compute, the reduction in computing time from the fitting procedure is considerable.

The rate of convergence from the Monte Carlo sampling is studied by scanning through the vertical(the energy bias ϵ) and horizontal energy(the system-bath coupling η) gaps in the spin-boson model. Figure 4.3 and 4.4 show that the sampling scheme is likely to work

well for system with large energy bias and large system-bath coupling. When the system-bath coupling is large, the electron transfer process is also likely to be fast and only shorter trajectories are needed, thus shortens the simulation time.

In future works, we will need to examine different quasi-classical strategies to approximate the hopped trajectories, which is the last assumptions in using the THLE. Due to the strong resemblance of the hopped trajectories to classical mechanics, various methods are available for its computation, such as the frozen-Gaussian approximation[113], the ring polymer dynamics[112] and the Herman-Kluk initial value representation[53, 60], just to name a few. We will also need to compute the equilibrium population P_1^{eq} from Monte Carlo sampling. However, since it is an equilibrium property that does not involve nonadiabatic dynamics, it is convergence is likely to be much quicker than the convergence of the integrated kernel.

Overall, the benchmark results from Monte Carlo procedure in the spin-boson model indicates feasibility in realistic systems, especially in cases of long-range electron transfer systems. The fitting procedure may substantially improve the convergence of the sampling procedure and keeps the number of trajectories need low.

(a)

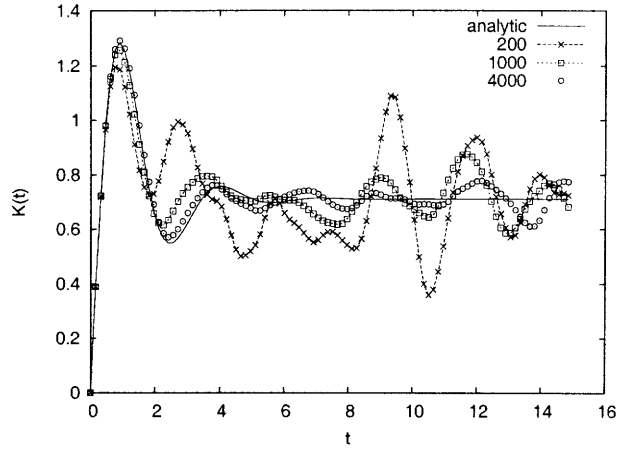

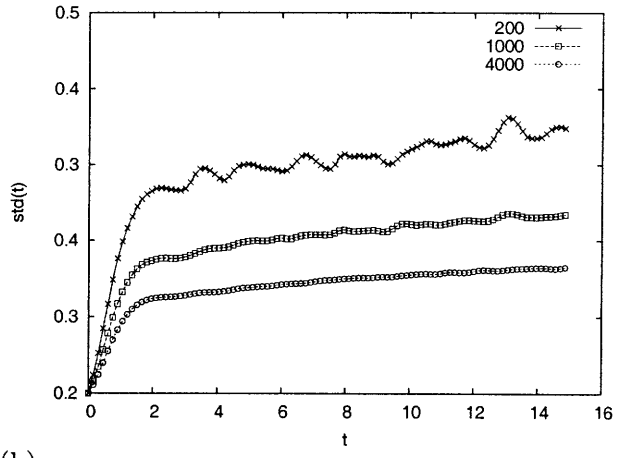

(b)

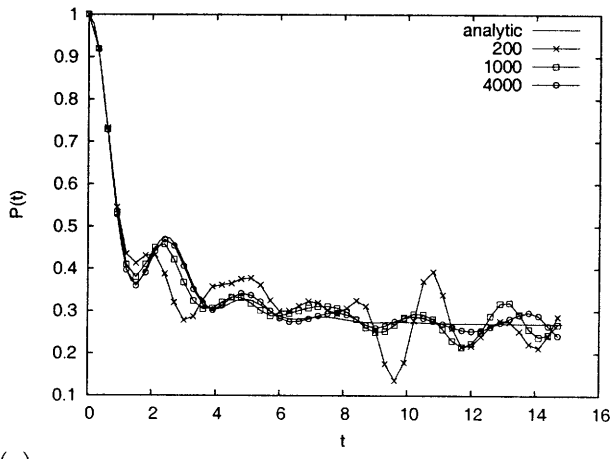

(c)

Figure 4.1: Convergence with respect to the number of Monte Carlo trajectories. The parameters are $\beta\Delta = .5$, $\omega = 5\Delta$, $\eta = 0.5\Delta$ and $\epsilon = 1\Delta$. (a) The second order kernel with 200, 1000 and 4000 Monte Carlo trajectories. The solid line is the analytical result. (b) Standard deviations of the second order kernel. (c) Populations computed using second kernels.

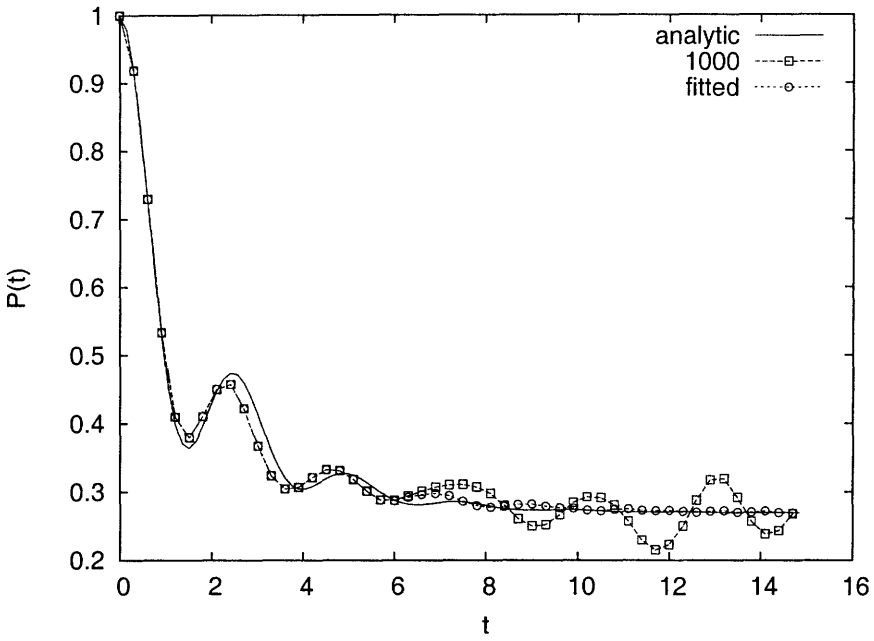

Figure 4.2: Comparison of the analytical result, the fitted result and the original Monte Carlo result with 1000 sampling trajectories. he parameters are $\beta\Delta = .5$, $\omega = 5\Delta$, $\eta = 0.5\Delta$ and $\epsilon = 1\Delta$.

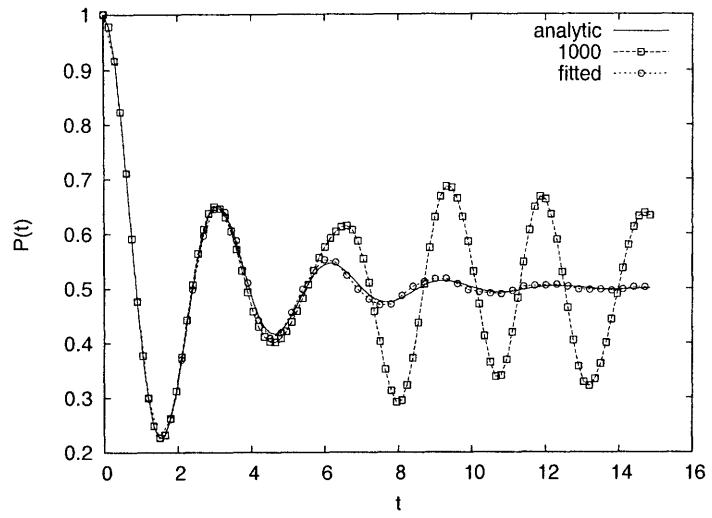

a

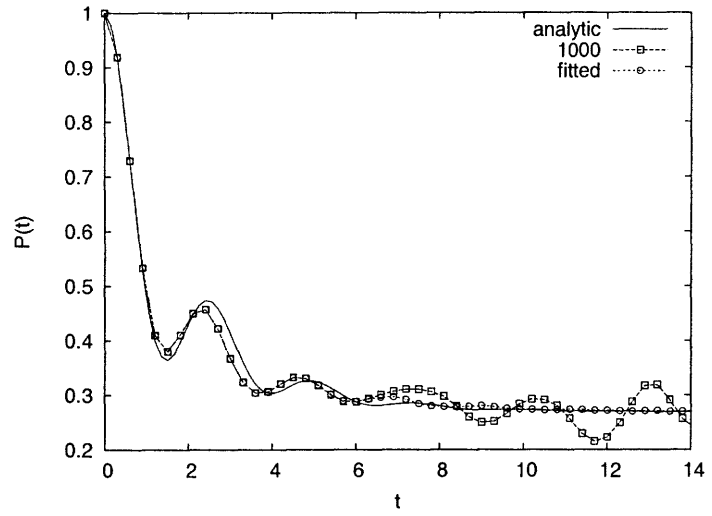

b

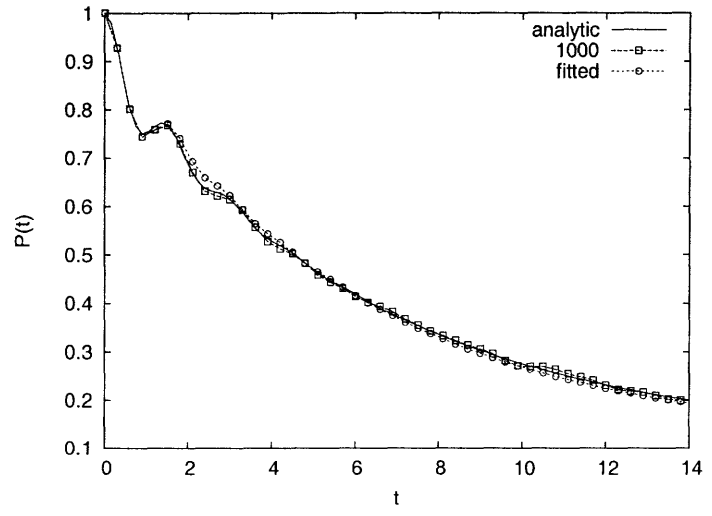

c

Figure 4.3: Quality of Monte Carlo results from 1000 samplings, with different energy bias. The parameters are $\beta\Delta = .5$, $\omega = 5\Delta$, $\eta = 0.5\Delta$. (a) $\epsilon = 0$ (b) $\epsilon = 1$ (c) $\epsilon = 2$

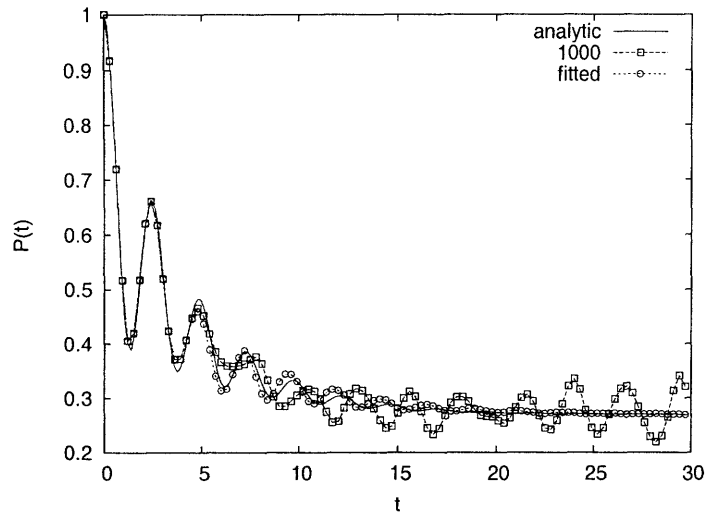

a

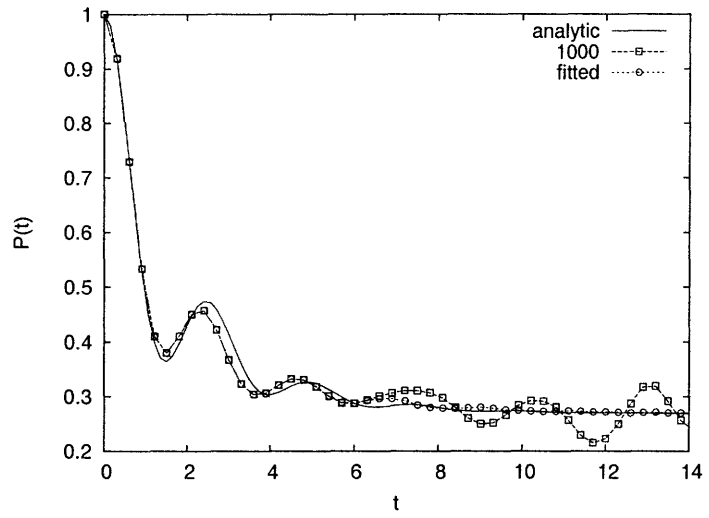

b

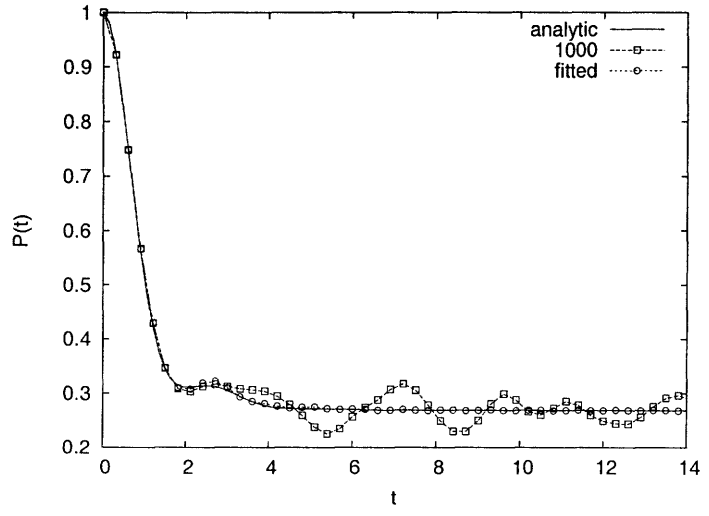

c

Figure 4.4: Quality of Monte Carlo results from 1000 samplings, with different energy bias. The parameters are $\beta\Delta = .5$, $\omega = 5\Delta$, $\eta = 0.5\Delta$. (a) $\epsilon = 0$ (b) $\epsilon = 1$ (c) $\epsilon = 2$

Chapter 5

Conclusion

The *ab initio* simulation of realistic electron transfer system has been a challenging topic for decades. One needs to overcome a number of problems for any hope of obtaining qualitatively correct result. These difficulties can be roughly categorized into the electronic structure and the nuclear dynamics area.

In terms of electronic structure calculations, DFT has been the most important tool in the box for large systems. However, the DFT is a ground-state theory, while for electron transfer problems, one must deal with excited states.

In the nuclear dynamics part, one faces the problem of combining the continuous nuclear motion in phase space and the transition in the discrete electronic states.

The constraint DFT method has been developed by the Van Voorhis group to answer the first question[10, 11, 12, 13]. My task is to develop methods for the second part, the nonadiabatic nuclear dynamics so that the constraint DFT can be used to perform on-the-fly *ab initio* simulations.

Two approaches have been tried. The first is the semi-classical approximation we discussed in chapter II. The idea is to map the discrete electronic states into a continuous representation, the spin-coherent states. Then we can write down the path integral of the nonadiabatic system in the spin-coherent states and the usual stationary phase approximation can be applied. Unfortunately, we found the "classical equation of motion" from such

treatment involves making the nuclei move on a mean-field thus unable to describe branchings. The inherent inability of the semi-classical approximation to conserve probability is another unfavorable observation. We conclude the semi-classical approach is not robust enough to be implemented further.

The second approach, the THLE, is much more successful. By carefully choosing the observable and the projection operator, we are able to show that the population fluctuation follows a linear regression equation. In principle it is equivalent of converting the problem of computing the population into computing the memory kernel. However, the memory kernel, in many cases, truncates quickly in powers of the inter-state coupling. By using a variational argument we can also optimize the inter-state coupling to facilitate the convergence of low order approximations. Furthermore, the expression of the memory kernel strongly suggests quasi-classical methods can be used for its computation. Bench mark results give us confidence of the THLE and make us ready to venture further into the real applications.

A small step toward the ultimate goal is taken before we completely depart from testing cases. In a realistic simulation we are guaranteed to use Monte Carlo sampling to compute anything thermal average. Since *ab initio* calculations are expensive, it makes sense to first try Monte Carlo on a simple system to tell whether it is possible at all to achieve convergence before one runs out of computing resources. Again, bench mark results are encouraging. Furthermore, we found a simple method of fitting the memory kernel can vastly reduce the number of trajectories needed. The conclusion is that it is indeed possible to extend the application of the THLE to the real world.

Nevertheless, the road to predicting unknown chemical systems from the first principle is rocky. For example, just actually finding the optimal frame can be a difficult task on its own. But I hope my work in the area of nonadiabatic dynamics may be a successful starting point for others and possible new graduate students in our group and finally the THLE can be fully implemented and join the surface hopping method as another major establishment in the field.

Bibliography

[1] G. Stock and M. Thoss. Classical description of nonadiabatic quantum dynamics. *Adv. Chem. Phys.*, 131:243, 2005.

[2] H. Köppel, W. Domcke, and L. S. Cederbaum. Multimode molecular dynamics beyond the Born-oppenheimer approximation. *Adv. Chem. Phys.*, 57:59, 1984.

[3] J. C. Tully. Molecular dynamics with electronic transitions. *J. Chem. Phys.*, 93:1061, 1990.

[4] X. G. Song and T. Van Voorhis. A coherent state approach to semiclassical nonadiabatic dynamics. *J. Chem. Phys.*, 124:134104, 2006.

[5] M. Ben-Nun, J. Quenneville, and T.J. Martinez. Ab initio multiple spawning: Photochemistry from first principles quantum molecular dynamics. *J. Phys. Chem. A*, 104(22):5161–5175, 2000.

[6] X. Sun and W. H. Miller. SC IVR for electronic nonadiabatic molecular dynamics. *J. Chem. Phys.*, 1069(15):5346, 10 January 1997.

[7] G. Stock and M. Thoss. Semiclassical description of nonadiabatic quantum dynamics. *Phys. Rev. Lett.*, 78(4):578, 7 August 1996.

[8] P. V. Parandekar and J. C. Tully. Mixed quantum-classical equilibrium. *J. Chem. Phys.*, 122:094102, 2005.

[9] G. Stock. Classical description of nonadiabatic photoisomerization processes and their real-time detection via femtosecond spectroscopy. *J. Chem. Phys.*, 103:10015, 1995.

[10] Q. Wu and T. Van Voorhis. Direct optimization method to study constrained systems within density-functional theory. *Phys. Rev. A*, 72(2):24502, 2005.

[11] Q. Wu and T. Van Voorhis. Direct calculation of electron transfer parameters through constrained density functional theory. *J. Phys. Chem. A*, 110(29):9212, 2006.

[12] Q. Wu and T. Van Voorhis. Constrained density functional theory and its application in long-range electron transfer. *J. Chem. Theory Compt.*, 2:765, 2006.

[13] Q. Wu and T. Van Voorhis. Extracting electron transfer coupling elements from constrained density functional theory. *J. Chem. Phys.*, 126:164105, 2006.

[14] P. Ehrenfest. *Z. Phys.*, 45(455):1927, 1927.

[15] M. Head-Gordon and J.C. Tully. Vibrational relaxation on metal surfaces: Molecular-orbital theory and application to CO/Cu (100). *J. Chem. Phys.*, 96:3939, 1992.

[16] X. Li, J. C. Tully, H. B. Schlegel, and M. J. Frisch. Ab initio Ehrenfest dynamics. *J. Chem. Phys.*, 123:084106, 2005.

[17] O. V. Prezhdo and P. J. Rossky. Mean-field molecular dynamics with surface hopping. *J. Chem. Phys.*, 107:825, 1997.

[18] U. Müller and G. Stock. Surface-hopping modeling of photoinduced relaxation dynamics on coupled potential-energy surface. *J. Chem. Phys.*, 107(16):6230, 14 July 1997.

[19] C. F. Craig, W. R. Duncan, and O. V. Prezhdo. Trajectory surface hopping in the time-dependent kohn-sham approach for electron-nuclear dynamics. *Phys. Rev. Lett.*, 95(16):163001–163001, 2005.

[20] B. F. Habenicht, C. F. Craig, and O. V. Prezhdo. Time-Domain Ab Initio Simulation of Electron and Hole Relaxation Dynamics in a Single-Wall Semiconducting Carbon Nanotube. *Phys. Rev. Lett.*, 2006:187401, 2006.

[21] S. Hammes-Schiffer and J. C. Tully. Proton-transfer in solution - molecular-dynamics with quantum transitions. *J. Chem. Phys.*, 101(6):4657, 1994.

[22] S. Y. Kim and S. Hammes-Schiffer. Molecular dynamics with quantum transitions for proton transfer: Quantum treatment of hydrogen and donor-acceptor motions. *J. Chem. Phys.*, 119(8):4389, 2003.

[23] L. Blancafort, P. Hunt, and M. A. Robb. Intramolecular electron transfer in bis(methylene) adamantyl radical cation: A case study of diabatic trapping. *J. Chem. Phys.*, 127(10):3391, 2005.

[24] P. Cattaneo, M. Persico, and A. Tani. Nonadiabatic processes in solution: molecular dynamics and surface hopping. *Chem. Phys.*, 246(1-3):315, 1999.

[25] H. G. Solari. Galuber's coherent states and the semiclassical propagator. *J. Math. Phys.*, 27(5):1351, 3 January 1986.

[26] A. J. Leggett, S. Chakravarty, A. T. Dorsey, M. P. A. Fisher, A. Garg, and W. Zwerger. Dynamics of the dissipative two-state system. *Rev. Mod. Phys.*, 59(1):1–85, 1987.

[27] U. U. Weiss. *Quantum Dissipative Systems.* World Scientific, 1999.

[28] R. Zwanzig. *Nonequilibrium Statistical Mechanics.* Oxford University Press US, 2001.

[29] A. A. Golosov and D. R. Reichman. Critical tests of a new master equation approach to nonadiabatic quantum dissipative systems. *Chem. Phys.*, 296(2):129–134, 2004.

[30] M. Sparpaglione and S. Mukamel. Dielectric friction and the transition from adiabatic to nonadiabatic electron transfer. I. Solvation dynamics in Liouville space. *J. Chem. Phys.*, 88:3263, 1988.

[31] J. Cao. Effects of bath relaxation on dissipative two-state dynamics. *J. Chem. Phys.*, 112(15):6719, 2000.

[32] C. Aalangul, N. Pottier, and D. Saint-James. Spin-boson systems: equivalence between the dilute-blip and the Born approximations. *J. Phys. (Paris)*, 47(10):1657–1661, 1986.

[33] R. Zwanzig. Ensemble Method in the Theory of Irreversibility. *J. Chem. Phys.*, 33:1338, 1960.

[34] H. Mori. Transport, collective motion, and Brownian motion. *Prog. Theor. Phys.*, 33:423, 1965.

[35] A. A. Golosov and D. R. Reichman. Reference system master equation approaches to condensed phase charge transfer processes. II. Numerical tests and applications to the study of photoinduced charge transfer reactions. *J. Chem. Phys.*, 115:9862, 2001.

[36] A. A. Golosov and D. R. Reichman. Reference system master equation approaches to condensed phase charge transfer processes. I. General formulation. *J. Chem. Phys.*, 115:9848, 2001.

[37] X. G. Song and T. Van Voorhis. A Langevin equation approach to electron transfer reactions in the diabatic basis. *J. Chem. Phys.*, 129:144502, 2008.

[38] D. Egorova, M. Thoss, W. Domcke, and H. Wang. Modeling of ultrafast electron-transfer processes: Validity of multilevel Redfield theory. *J. Chem. Phys.*, 119:2761, 2003.

[39] Q. Shi and E. Geva. A semiclassical generalized quantum master equation for an arbitrary system-bath coupling. *J. Chem. Phys.*, 120:10647, 2004.

[40] Q. Shi and E. Geva. A new approach to calculating the memory kernel of the generalized quantum master equation for an arbitrary system–bath coupling. *J. Chem. Phys.*, 119:12063, 2003.

[41] J. Cao. A phase space study of Bloch Redfield theory. *J. Chem. Phys.*, 107:3204, 1997.

[42] S. Jang, J. Cao, and R. J. Silbey. Fourth-order quantum master equation and its Markovian bath limit. *J. Chem. Phys.*, 116:2705, 2002.

[43] W. Domcke and G. Stock. Theory of ultrafast nonadiabatic excited-state processes and their spectroscopic detection in real time. *Adv. Chem. Phys.*, 100:1, 1997.

[44] H.-D. Meyer and W. H. Miller. Classical analog for electronic degrees of freedom in non-adiabatic collision processes. *J. Chem. Phys.*, 70(7):3214, 1979.

[45] W. H. Miller and C. W. McCurdy. Classical trajectory model for electronically non-adiabatic collision phenomena - classical analog for electronic degrees of freedom. *J. Chem. Phys.*, 69(11):5163, 1978.

[46] J. C. Tully. Molecular dydnamics with electronic transitions. *J. Chem. Phys.*, 93(2):1061, 2 April 1990.

[47] D. F. Coker and L. Xiao. Methods for molecular-dynamics with nonadiabatic transitions. *J. Chem. Phys.*, 102(1):496, 1995.

[48] J. C. Tully and R. K. Preston. Trajectory Surface Hopping Approach to Nonadiabatic Molecular Collisions: The Reaction of H+ with D2. *J. Chem. Phys.*, 55(2):562, 1971.

[49] D. F. Coker and S. Bonella. Land-map, a linearized approach to nonadiabatic dynamics using the mapping formalism. *J. Chem. Phys.*, 122(19):194102, 2005.

[50] M. Thoss and G. Stock. Mapping approach to the semiclassical description of nonadiabatic quantum dynamics. *Phys. Rev. A*, 59(1):64, January 1999.

[51] F. Webster, P. J. Rossky, and R. A. Friesner. Nonadiabatic processes in condensed matter: semi-classical theory and implementation. *Compt. Phys. Commun.*, 63:494, 1991.

[52] M. F. Herman and J. C. Arce. A semiclassical surface hopping formalism for solvent-induced vibrational-relaxation. *Chem. Phys.*, 193(2-3):335, 1994.

[53] M. F. Herman. A semiclassical surface hopping propagator for nonadiabatic problems. *J. Chem. Phys.*, 103(18):8081, 1995.

[54] S. Bonella and D. F. Coker. Semicassical implementation of the mapping Hamiltonian approach for nonadiabatic dynamics using focused initial distribution sampling. *J. Chem. Phys.*, 118(10):4370, 2003.

[55] P. Pechukas. Time-dependent semiclassical scattering theory. 2. Atomic collisions. *Phys. Rev.*, 181(1):174, 1969.

[56] H.-D. Meyer and W. H. Miller. Classical-models for electronic degrees of freedom - derivation via spin analog and application to Fstar+H2-]F+H2. *J. Chem. Phys.*, 71(5):2156, 1979.

[57] M. Thoss, H. B. Wang, and W. H. Miller. Self-consistent hybrid approach to complex systems: Application to the spin-boson model with Debye spectral density. *J. Chem. Phys.*, 115(7):2991, 2001.

[58] N. C. Balis and D. G. Truhlar. Trajectory-surface hopping study of NA(3P2P)+H2-]NA(3S3S)+H2(V',J',THETA). *J. Chem. Phys.*, 79(3):1334, 1983.

[59] M. F. Herman and E. Kluk. A semiclassical justification for the use of non-spreading wavepackets in dynamics calculations. *Chem. Phys.*, 91(1):27, 1984.

[60] K. G. Kay. Integral expressions for the semiclassical time-dependent propagator. *J. Chem. Phys.*, 100(6):4377, 1994.

[61] M. Thoss, W. H. Miller, and G. Stock. Semiclassical description of nonadiabatic quantum dynamics: Application to the S-1-S-2 conical intersection in pyrazine. *J. Chem. Phys.*, 112(23):10282, 2000.

[62] A. Raa, G. A. Worth, H.-D. Meyer, and L. S. Cederbaum. Molecular dydnamics of pyrazine after excitation to the S-2 electronic state using a realistic 24-model Hamiltonian. *J. Chem. Phys.*, 110(1):241, 1999.

[63] A. Lucke, C. H. Mak, and J. T. Stockburger. Semiclassical dynamics of nonadiabatic transitions in disrete-state systems using spin coherent-state path integrals. *J. Chem. Phys.*, 111(24):10843, 1999.

[64] G. Zaitsev. Spin phase-space semiclassics for weak spin-orbit coupling. *J. Phys. A.*, 35:L721, 2002.

[65] M. Pletyukhov and G. Zaitsev. Semiclassical theory of spin-orbit interaction in the extended phase space. *J. Phys. A.*, 36:5181, 2003.

[66] M. Pletyukhov, C. Amann, M. Mehta, and M. Brack. Semiclassical theory of spin-orbit interactions using spin coherent states. *Phys. Rev. Lett.*, 89(11):116601, 2002.

[67] T. Van Voorhis and E. J. Heller. Similarity transformed semiclassical dynamics. *J. Chem. Phys.*, 119(23):12153, 25 September 2003.

[68] T. Van Voorhis and E. J. Heller. Nearly real trajectories in complex semiclassical dynamics. *Phys. Rev. A*, 66:050501, 4 November 2002.

[69] J. R. Kaluder and B. S. Skagerstam. *Coherent states, Applications in Physics and Mathematical Physics.* World Scientific, Singapore, 1985.

[70] H. G. Solari. Semiclassical treatment of spin system by means of coherent states. *J. Math. Phys.*, 28(5):1097, 7 January 1987.

[71] E. J. Heller. Phase space interpretation of semiclassical theory. *J. Chem. Phys.*, 67(7):3339, 1 October 1977.

[72] M. Stone, K. Park, and A. Garg. The semiclassical propagator for spin coherent states. *J. Math. Phys.*, 41(12):8025, 30 August 2000.

[73] A. Alscher and H. Grabert. Semiclassical dynamics of the Jaynes-Cummings model. *Eur. Phys. J. D*, 14:127, 2000.

[74] Y. Weissman. Semiclassical approximation in the coherent states representation. *J. Chem. Phys.*, 76(8):4067, 15 April 1982.

[75] J. Kerchan, P. Leboeuf, and M. Saraceno. Semiclassical approximations in the coherent-state representation. *Phys. Rev. A*, 40(12):6800, 19 June 1989.

[76] W. H. Press, S. A. Teukolsky, W. T. Vellerling, and B. P. Flannery. *Numerial Recipes in C.* Cambridge University Press, Cambridge, 2nd edition, 1992.

[77] E. E. Nikitin. *Theory of Elementary Atomic and Molecular Process in Gases.* Clarendon, Oxford, 1974.

[78] D. Huber and E. J. Heller. Generalized Gaussian wave packet dynamics. *J. Chem. Phys.*, 87(9):5302, 29 July 1987.

[79] T. Van Voorhis and D. R. Reichman. Semiclassical representations of electronic structure and dynamics. *J. Chem. Phys.*, 120(2):579, 13 October 2003.

[80] R. Schneider and W. Domcke. S1-S2 conical intersection and ultrafast S2-S1 internal-conversion in pyrazine. *Chem. Phys. Lett.*, 150(3-4):235, 16 September 1988.

[81] B. Wolfseder and W. Domcke. Intramelecular electron-transfer dynamics in the inverted regime: Quantum mechanical multi-mode model including dissipation. *Chem. Phys. Lett.*, 259(1-2):113, 30 August 1996.

[82] L. Seidner and W. Domcke. Microscopic modeling od photoisomerization and internal-conversion dynamics. *Chem. Phys.*, 186(1):27, 15 August 1994.

[83] H. Köppel. New ultrafast nonradiative decay mechanism in the benzene radical cation. *Chem. Phys. Lett.*, 205:361, 1993.

[84] P. F. Barbara, T. J. Meyer, and M. A. Ratner. Contemporary issues in electron transfer research. *J. Phys. Chem*, 100:13148–13168, 1996.

[85] U. Bach, D. Lupo, P. Comte, J. E. Moser, F. Weissörtel, J. Salbeck, H. Spreitzer, and M. Grätzel. Solid-state dye-sensitized mesoporous TiO 2 solar cells with high photon-to-electron conversion efficiencies. *Nature*, 395(6702):583, 1998.

[86] M. Segal, M. Singh, K. Rivoire, S. Difley, T. Van Voorhis, and M. A. Baldo. Extrafluorescent electroluminescence in organic light-emitting devices. *Nature Materials*, 6:374–378, 2007.

[87] H. Lee, Y. C. Cheng, and G. R. Fleming. Coherence dynamics in photosynthesis: Protein protection of excitonic coherence. *Science*, 316(5830):1462, 8 July 2007.

[88] G. Stock. A semiclassical self-consistent-field approach to dissipative dynamics: The spin–boson problem. *J. Chem. Phys.*, 103:1561, 1995.

[89] M. D. Hack, A. M. Wensmann, D. G. Truhlar, M. Ben-Nun, and T. J. Martinez. Comparison of full multiple spawning, trajectory surface hopping, and converged quantum mechanics for electronically nonadiabatic dynamics. *J. Chem. Phys.*, 115:1172, 2001.

[90] X. Sun and W. H. Miller. Semiclassical initial value representation for electronically nonadiabatic molecular dynamics. *J. Chem. Phys.*, 106:6346, 1997.

[91] R. A. Harris and R. Silbey. On the stabilization of optical isomers through tunneling friction. *J. Chem. Phys.*, 78:7330, 1983.

[92] R. A. Harris and R. Silbey. Variational calculation of the tunneling system interacting with a heat bath. II. Dynamics of an asymmetric tunneling system. *J. Chem. Phys.*, 83:1069, 1985.

[93] R. Silbey and R. A. Harris. Variational calculation of the dynamics of a two level system interacting with a bath. *J. Chem. Phys.*, 80(6):2616, 16 December 1983.

[94] H. B. Wang, M. Thoss, and W. H. Miller. Systematic convergence in the dynamical hybrid approach for complex systems: A numerical exact methodolgy. *J. Chem. Phys.*, 115(7):2979, 15 August 2001.

[95] M. Thoss, H. Wang, and W.H. Miller. Self-consistent hybrid approach for complex systems: Application to the spin-boson model with Debye spectral density. *J. Chem. Phys.*, 115:2991, 2001.

[96] R. Mazo and M. Girandeau. Variational Methods in Statistical Mechanics. *Adv. Chem. Phys.*, 1973.

[97] H. P. Breuer and F. Petruccione. *The Theory of Open Quantum Systems.* Oxford University Press, 2002.

[98] H. Wang and M. Thoss. Multilayer formulation of the multiconfiguration time-dependent Hartree theory. *J. Chem. Phys.*, 119:2126, 2003.

[99] H. Sumi and R. A. Marcus. Dynamical effects in electron transfer reactions. *J. Chem. Phys.*, 84:4894, 1986.

[100] H. Wang, X. Song, D. Chandler, and W. H. Miller. Semiclassical study of electronically nonadiabatic dynamics in the condensed-phase: Spin-boson problem with Debye spectral density. *J. Chem. Phys.*, 110:4828, 1999.

[101] A. Warshel and R. M. Weiss. An empirical valence bond approach for comparing reactions in solutions and in enzymes. *J. Am. Chem. Soc.*, 102:6218, 1980.

[102] S. R. Billeter, S. P. Webb, P. K. Agarwal, T. Iordanov, and S. Hammes-Schiffer. Hydride Transfer in Liver Alcohol Dehydrogenase: Quantum Dynamics, Kinetic Isotope Effects, and Role of Enzyme Motion. *J. Am. Chem. Soc.*, 123:11262, 2001.

[103] R. Bianco and J. T. Hynes. VB resonance theory in solution. I. Multistate formulation. *J. Chem. Phys.*, 102:7864, 1995.

[104] D. M. Ceperley and B. J. Alder. Ground State of the Electron Gas by a Stochastic Method. *Phys. Rev. Lett.*, 45:566, 1980.

[105] R. Car and M. Parrinello. Unified Approach for Molecular Dynamics and Density-Functional Theory. *Phys. Rev. Lett.*, 55(22):2471–2474, 1985.

[106] M. P. Allen and D. J. Tildesley. *Computer Simulation of Liquids.* Oxford University Press, 1989.

[107] D. M. Ceperley. Path integrals in the theory of condensed helium. *Rev. Mod. Phys.*, 67:279, 1995.

[108] P. Sindzingre, M. L. Klein, and D. M. Ceperley. Path-integral Monte Carlo study of low-temperature He-4 clusters. *Phys. Rev. Lett.*, 63:1601, 1989.

[109] M. Sprik, R. W. Impey, and M. L. Klein. Study of electron solvation in liquid ammonia using quantum path integral Monte Carlo calculations. *J. Chem. Phys.*, 83:5802, 1985.

[110] M. Sprik, M. L. Klein, and D. Chandler. Staging: A sampling technique for the Monte Carlo evaluation of path integrals. *Phys. Rev. B*, 31:4234, 1985.

[111] J. W. Negele and H. Orland. *Quantum many-particle systems.* Addison and Wesley, 1988.

[112] I. R. Craig and D. E. Manolopoulos. Quantum statistics and classical mechanics: Real time correlation functions from ring polymer molecular dynamics. *J. Chem. Phys.*, 121:3368, 2004.

[113] E. J. Heller. Time-dependent approach to semiclassical dynamics. *J. Chem. Phys.*, 62:1544, 1975.